

Ulrich L. Rohde, Federal Armed Forces University,
Munich, Germany ; Ajay K. Poddar, Synergy
Microwave, NJ

Metamaterial Resonators: Theory and Applications

From metallic alloys to plastic composites, scientists and engineers have been developing artificial materials for various applications. Metamaterial, a family of artificial composite structures made from conventional material with unconventional structures, exhibits distinct properties apart from what nature can provide easily, such as negative index characteristics for selective frequency regions.¹⁻⁸ The shape, size, geometry, orientation and arrangement of metamaterial gives it smart properties, capable of manipulating electromagnetic (EM) waves by bending, blocking, absorbing and enhancing to attain benefits that go beyond what is possible with conventional materials.

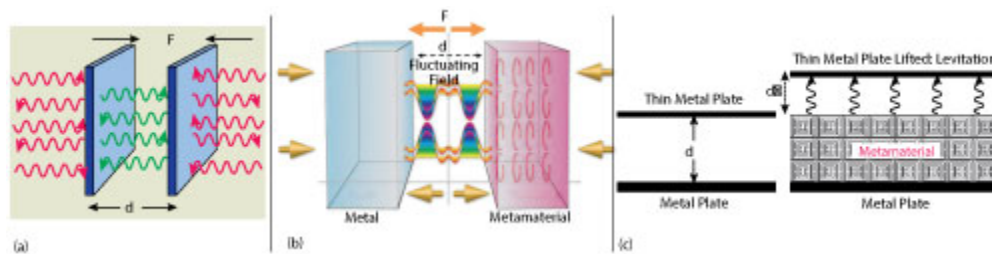


Figure 1 The Casimir force (F) on a parallel plate kept in vacuum (a)⁹ the repulsive Casimir force (F) on parallel plate (b)¹¹ Casimir force levitating a mirror (c).¹²

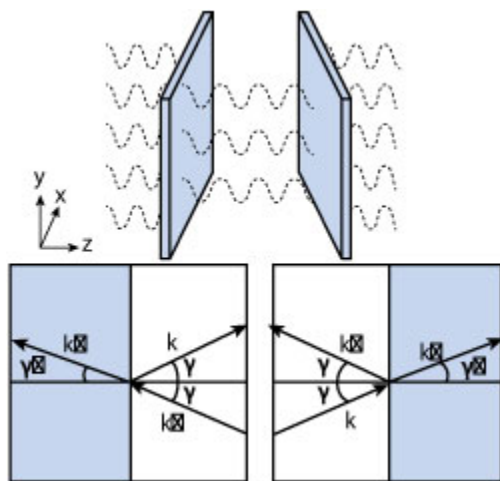


Figure 2 The Gravitational Casimir effect.¹³

Ulrich L. Rohde, Federal Armed Forces University, Munich, Germany ; Ajay K. Poddar, Synergy Microwave, NJ

The Casimir force arises from the interaction of the surfaces with the surrounding electromagnetic spectrum, and includes a complex dependence on the full dielectric function of both surfaces and the region between. The complexity of the Casimir force leads to significant possibilities for manipulation through materials, geometries and other phenomena. It potentially provides the opportunity for neutralizing or partially cancelling Van Der Waals forces. On the more theoretical side, the MMI structure can produce a powerful Casimir effect (force from nothing), which enables the transport of matter, i.e., the use of this effect to attract or repel physical matter. Some practical applications include auto focusing camera lenses, more efficient servos, silicon array propulsion systems and high speed rail systems. The implications of a repulsive Casimir force for the micro-electromechanical systems (MEMS) industry could be significant with potential applications including stiction prevention in sensors, contactless bearings and contactless power transmission.¹⁰ MEMS based electronics offer inexpensive high performance solutions; but reliability issues arising from stiction in MEMS switching devices limits their use in high frequency applications.

The pioneering contributions relate to techniques for a stiction-free MEMS lateral switch and its application in switching networks and phase shifters in electronically scanned phase array antennas for Internet of Things (IoT) applications. In a vacuum, the force of attraction between two surfaces separated by nanometers is explained by the Casimir effect, but effective repulsive forces can be noticed when the two surfaces with materials of different permittivity are taken into consideration.¹¹⁻¹² This phenomenon can also be observed if one of the surfaces possesses negative permittivity. This approach can resolve the stiction problem, leading to new material and fabrication methods in next generation MEMS.

One of the exciting properties of MMI structures is that they can bend light in a way that is mathematically equivalent to the way space-time bends light, allowing topological exploration for the realization of low cost gravitational wave detectors. **Figure 2** shows the Gravitational Casimir effect, with a two plate setup. The change in the refractive index of the plates causes the gravitational wave to refract, where k represents the wave vector of the incident, transmitted, and reflected gravitational waves, and γ is the corresponding angle with respect to the surface normal.¹³

Details of the Casimir effect and applications and use of the MMI structure for futuristic applications will be discussed in part 2 (June 2016 issue) and part 3 (July 2016 issue). This article briefly describes applications of the MMI structure for the IoT, CubeSat, and examples of the Möbius transformation and metamaterial symmetry for medical telemetry, imaging and sensor applications.

Ulrich L. Rohde, Federal Armed Forces University, Munich, Germany ; Ajay K. Poddar, Synergy Microwave, NJ

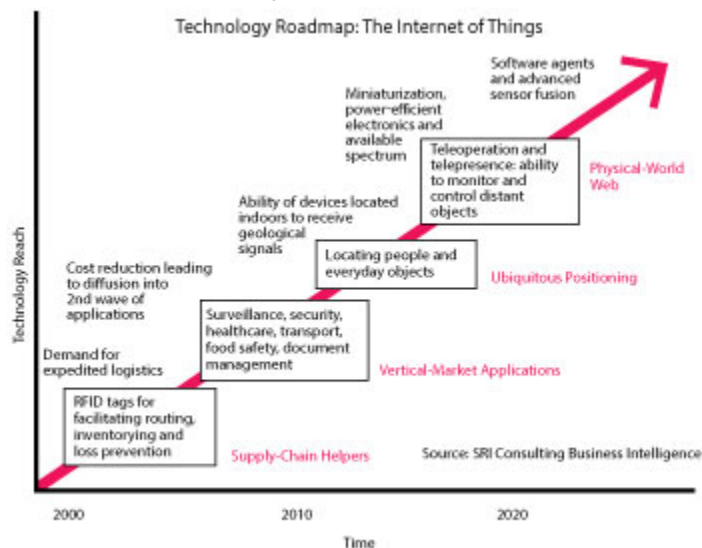


Figure 4 IoT Technology Roadmap.¹⁴

INTERNET OF THINGS (IoT)

The Internet of Things (IoT) is the network of physical objects: devices, vehicles, buildings and other items embedded with electronics, software, sensors and network connectivity that enable these objects to collect and exchange data (see **Figure 3**).¹⁴ The IoT allows objects to be sensed and controlled remotely across the existing network infrastructure, creating opportunities for more direct integration of the physical world into computer-based systems, resulting in improved efficiency, accuracy and economic benefit; when the Internet is augmented with sensors and actuators, it becomes an instance of the more general class of cyber-physical systems, which encompasses technologies such as smart grids, smart homes, intelligent transportation and smart cities. Each thing is uniquely identifiable through its embedded computing system but is also able to interoperate within the existing Internet infrastructure.

Figure 4 illustrates the IoT Technology Roadmap.¹⁴ Current technology cannot yet meet the needs for faster, more reliable and more ubiquitous radio systems required by the IoT. The trend over past decades has been to place an ever increasing emphasis on digital signal processing (DSP), where spectral efficiency has been maximized via sophisticated modulation, multiplexing or MIMO schemes. However, these approaches have now reached their limits and migration to millimeter wave and terahertz frequencies has become indispensable to access broader spectral resources. Unfortunately, DSP is not applicable at such frequencies, where signals are varying too fast to be digitized. The unprecedented control of electromagnetic properties afforded by the MMI structure opens the door to provide fast processing and low power miniaturized electronics to overcome technological challenges.

Ulrich L. Rohde, Federal Armed Forces University, Munich, Germany ; Ajay K. Poddar, Synergy Microwave, NJ

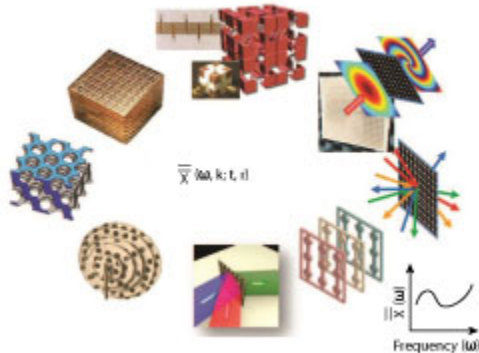


Figure 5 Sketch of metamaterial engineering.⁸

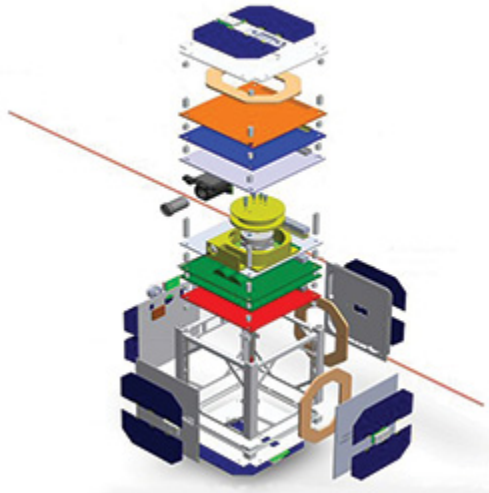


Figure 6 Typical CubeSat layout (courtesy ESTCube-1).¹⁸

Recent publications describe the real-time analog signal processing (R-ASP) of electromagnetic waves at very high frequencies using metamaterial inspired technology in conjunction with concepts of ultrafast optics.¹⁵⁻¹⁷ There is need for a special branch of metamaterial engineering concerning the manipulation of EM waves in space, time and space-time for the realization of an unlimited number of distinct types of artificial smart materials (electromagnetic band gap metamaterial, single negative metamaterial, double negative metamaterial, biisotropic and bianisotropic metamaterial and chiral metamaterial). This technology is suited for telecommunications, medical instrumentation (bio-medical, oral and oncology, ultrasound imaging and magnetic resonance imaging), optics, sensing (bio, thin film, wireless strain, aerospace and defense), energy harvesting, transportation of matter, and levitation/anti-gravity (attractive and repulsive Casimir effect).

Ulrich L. Rohde, Federal Armed Forces University,
Munich, Germany ; Ajay K. Poddar, Synergy
Microwave, NJ

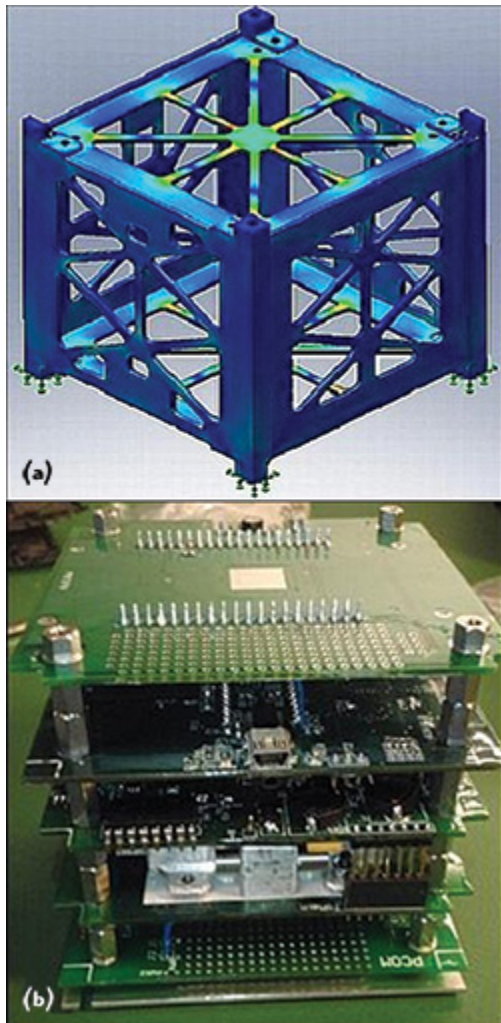


Figure 7 CubeSat bus structure (a) and photo of the interior bus configuration (b) (courtesy Colorado Space Grant Consortium).¹⁹

Ulrich L. Rohde, Federal Armed Forces University, Munich, Germany ; Ajay K. Poddar, Synergy Microwave, NJ



Figure 8 CubeSat hardware (a) and CubeSat in low-Earth orbit (b) (courtesy NASA).²⁰

These applications are supported on the IoT technology roadmap.¹⁴ Figure 5 depicts the typical sketch of metamaterial engineering, illustrating the solutions for next generation electronic circuits and systems.⁸ As shown in Figure 5, $(\bar{\chi})_{\omega, \mathbf{k}; \mathbf{t}, \mathbf{r}}$ is the generic notation of tensors that represents the metamaterial permittivity ($(\bar{\epsilon})$), permeability ($(\bar{\mu})$), magnetic-to-electric coupling ($(\bar{\kappa})$) and electric-to-magnetic coupling ($(\bar{\zeta})$) tensors, while ω is the angular frequency (reciprocal time), k is the spatial frequency (reciprocal space), t is time (direct time) and r is space (direct space). Combining different dependencies ($\omega, k; t, r$) and bianisotropies ($(\bar{\epsilon}, \bar{\mu}, \bar{\kappa}, \bar{\zeta})$) leads to a virtually unlimited number of distinct types of metamaterials.⁸



Figure 9 Network of CubeSats (courtesy NASA).²⁰

CUBESAT

Satellites play a decisive role for establishing communication networks; these satellites are expensive, large in size and take a number of years to build up. To keep costs low, small satellites

Ulrich L. Rohde, Federal Armed Forces University, Munich, Germany ; Ajay K. Poddar, Synergy Microwave, NJ

such as the CubeSat, have yielded big rewards versus their larger counterparts. Small satellites are located in low-Earth orbit (LEO) in the range of 200 to 2,000 km altitude. The speed of small satellites in LEO (relative to Earth's surface) is around 7.5 km/s, which is an orbital period of approximately 90 minutes. The definition of CubeSat comes from its shape and weight. It belongs to the family of small satellites: Picosatellite <1 kg, nanosatellite 1 to 10 kg, and microsatellite 10 to 100 kg). **Figure 6** shows a typical CAD model of a CubeSat (10 cm × 10 cm × 10 cm),¹⁸ **Figure 7** shows a typical bus structure and **Figure 8** shows the actual CubeSat in hand as well as its position in low-Earth orbit.²⁰ The basic subsystems of a CubeSat are telemetry, tracking and control (TTC), power generation and distribution (PGD), data command and handling (DCH), altitude determination and control (ADC) and the payload.

Small satellites cost much less per unit; many CubeSats can be fabricated for the price of one conventional satellite. Although a CubeSat is lower in cost, it obviously does not have the individual payload capacity of a large satellite. A possible cost-effective alternative is to launch many CubeSats as depicted in **Figure 9**, and construct a network of small satellites that can accomplish the same tasks as one large satellite. The advantage is that if one CubeSat fails, the network can be reconfigured to pick up the slack, whereas one satellite is a single point of mission failure. **Figure 10** illustrates the CubeSat launch operations concept,¹⁹⁻²² while **Figure 11** shows the communication link.²³

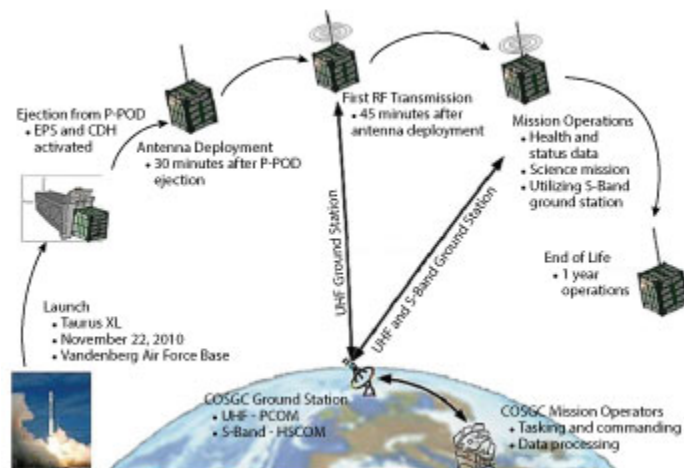


Figure 10 CubeSat launch operations concept (courtesy Colorado Space Grant Consortium).²¹

Antenna size for the communication link is a limitation in small satellites. The maximum gain of conventional aperture antennas (e.g., dish reflectors, horns, arrays) is determined by aperture size. The relatively large size needed for adequate performance, however, makes them unfriendly for space application. Modifications enabled by smart material can either enhance performance or reduce mass, thus lowering the cost of putting the antenna in space. Lighter antennas reduce weight directly, while more energy efficient antennas reduce the size and weight of required storage batteries and solar cells. The metamaterial lined horn antenna with low-index electromagnetic properties shown in **Figure 12**, for example, is relatively small in size, but not yet suitable for small satellite (CubeSat) applications.²⁴

Ulrich L. Rohde, Federal Armed Forces University, Munich, Germany ; Ajay K. Poddar, Synergy Microwave, NJ

Ongoing research towards developing miniaturized low-index metamaterial lens antennas for small satellites faces challenges such as bandwidth and efficiency. Metamaterial lenses exhibit material properties that approximate the behavior of a material with low ($0 < n < 1$) effective index of refraction, and by using dispersion techniques a relatively wideband low-index region can be obtained. A low-index metamaterial lens can create highly collimated beams in the far field from a low directivity antenna feed by, for example, using dual-split ring resonators (DSRR) in the x-y plane for a low permeability response, and end-loaded dipole (ELD) elements in the x-z and y-z planes for a low permittivity response.

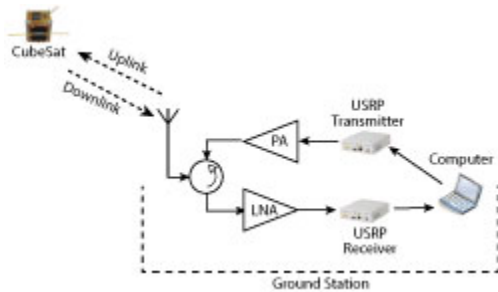


Figure 11 Schematic of general CubeSat communication setup.²³

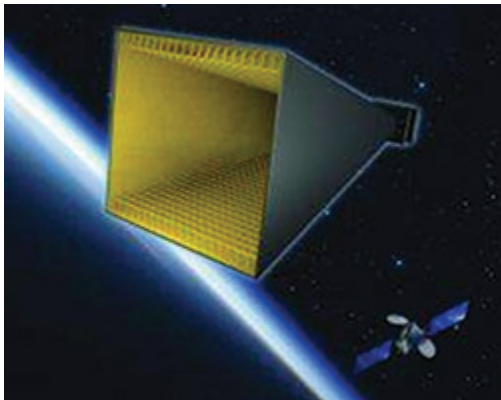


Figure 12 typical metamaterial lined feed horn antenna for satellite communications.²⁴

As ϵ or μ approaches zero, the passband narrows, improving collimation and directivity of the antenna, so that it can be integrated with software defined radio (SDR), facilitating a transformative communication system with remarkable frequency and polarization agility; this is well suited for CubeSat application where multifunctional miniature antennas is the desired goal.

Ulrich L. Rohde, Federal Armed Forces University,
Munich, Germany ; Ajay K. Poddar, Synergy
Microwave, NJ

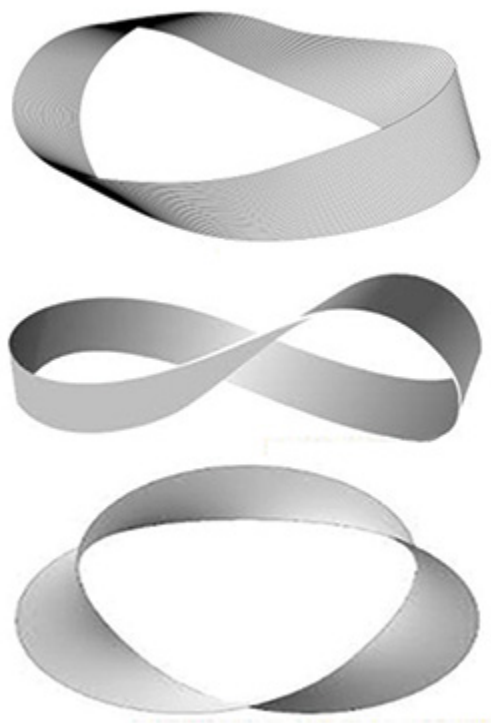


Figure 13 Möbius strips with single twist (top) with single twist and pinched (center) and with three twists (bottom).

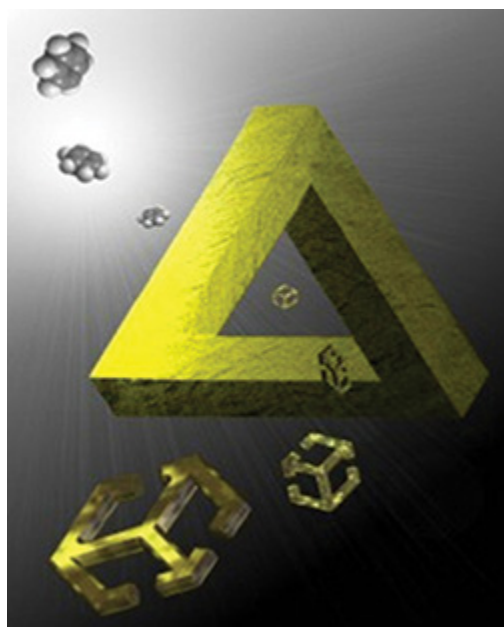


Figure 14 Möbius strip symmetry in metamolecular trimmers.²⁷

Ulrich L. Rohde, Federal Armed Forces University, Munich, Germany ; Ajay K. Poddar, Synergy Microwave, NJ

Smart MMI structures support the development of miniaturized multifunctional antennas, high efficiency solar panels for power generation and the performance of real-time analog signal processing of electromagnetic waves at very high frequencies. Tunable metamaterials using Möbius topology enable broadband tuning in a compact size with narrow instantaneous bandwidths across an entire communications band depending on the channel in use. Tuning the metamaterial and the antenna in tandem provides a dynamic operating channel with a tunable, nearly arbitrary polarization response as an added benefit. The major challenge is figuring out a way to scale these metamaterial and associated antenna structures to operate at lower frequencies while maintaining a practical physical size and weight. MMI technology enables a planar antenna with reduced size at lower frequency without degrading performance.

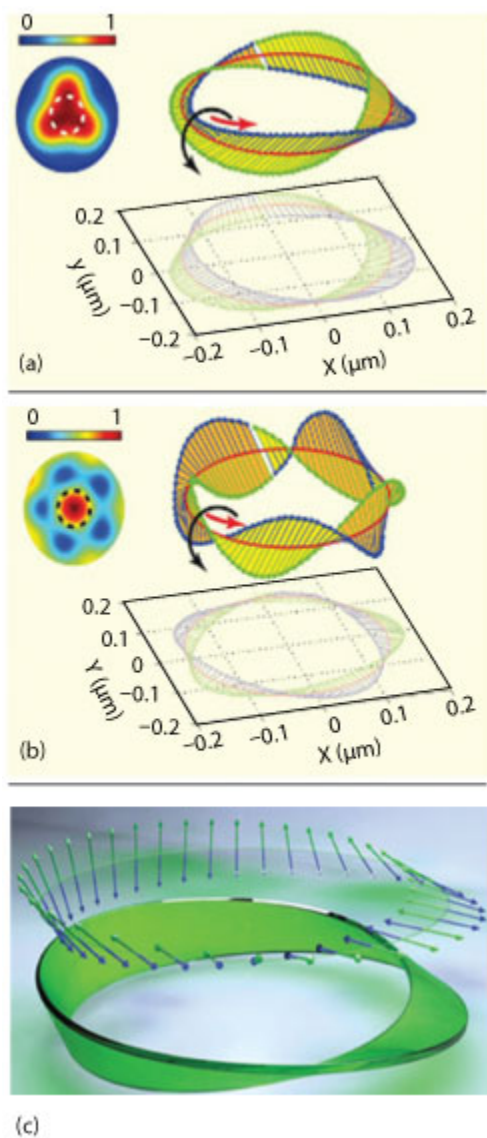


Figure 15 Numerically calculated and experimentally observed optical polarization twist around the Möbius strip: single knot (a) multi-knot (b) and polarization twist (c).²⁸

Ulrich L. Rohde, Federal Armed Forces University, Munich, Germany ; Ajay K. Poddar, Synergy Microwave, NJ

MÖBIUS TRANSFORMATION: METAMATERIAL SYMMETRY

The concept of the Möbius strip is based on the fact that one can travel without encountering obstruction around the loop. The loop behaves like a never ending point, giving rise to the concept of an infinite path in the space-time domain. The concept of infinity is not emptiness or space; rather, it is the concept of having no beginning and no end (see **Figure 13**). As shown, the Möbius strip with one twist and pinched in the middle appears like the mathematical symbol for infinity. Since space-time is curved, it could conceivably run back on itself like the Möbius strip, and have no boundary. Our universe can be considered to be a replica of the Möbius strip with a multiple number of twists of vibrating strings in space, whirling in a warped loop as it experiences its own starting point, and recurs perpetually in space-time dynamics. These “strings” vibrate in multiple dimensions, and depending upon how they vibrate, they might be seen in 3-dimensional space as matter, light or gravity. The figure also shows a 3-twist Möbius strip (twists can be defined as knots).

For engineers, the multi-knot Möbius strip surface is a launch pad to complex geometries and topological exploration of next generation electronic circuits and systems for industrial, medical and space applications. Topology is a field of science that studies invariance of certain properties under continuous deformation, such as stretching, bending or twisting of the underlying geometry. Topological symmetry is defined as a property, conserved when the system undergoes an alteration (deformation, twisting and stretching of objects). Möbius strips deform in a way that its metrical properties barely change, and they violate the Hückel rules.²⁵ Some nanostructures, for example, possess identical elastic properties even after deformation.

It is interesting to note that the Möbius transformations allow complex geometries for realizing a number of distinct types of metamaterials. Metamaterials can be realized with either an array of wire/split ring structures or composite right/left-handed (CRLH) transmission line resonators. The major difference between the two is the coupling dynamics; the wire/split ring structure is loosely coupled, whereas the CRLH transmission line resonator structure is tightly coupled. Since the wire/split rings are practically uncoupled, operating bandwidth is determined by the quality factors and losses associated with individual wire/split-ring structures. The challenge is to reduce the losses and improve the quality factors. In the case of CRLH transmission line resonator-based structures, the resonators are tightly coupled, effectively increasing the operating bandwidth as compared to wire/split ring-based structures.⁷

Topological Möbius metamaterial symmetry due to Möbius transformation $f(z)$, is given by²⁶

$$f(z) = \frac{az + b}{cz + d};$$
$$(a, b, c, d \in \mathbb{C} \text{ and } ad - bc \neq 0) \quad (1)$$

$$z \in \mathbb{C} \rightarrow z = r [\cos(\theta) + i\sin(\theta)] \quad (2)$$

where a, b, c and d are complex numbers, and the numerator of Equation 1 is not a multiple of the denominator (i.e., $ad - bc \neq 0$).

Ulrich L. Rohde, Federal Armed Forces University,
Munich, Germany ; Ajay K. Poddar, Synergy
Microwave, NJ

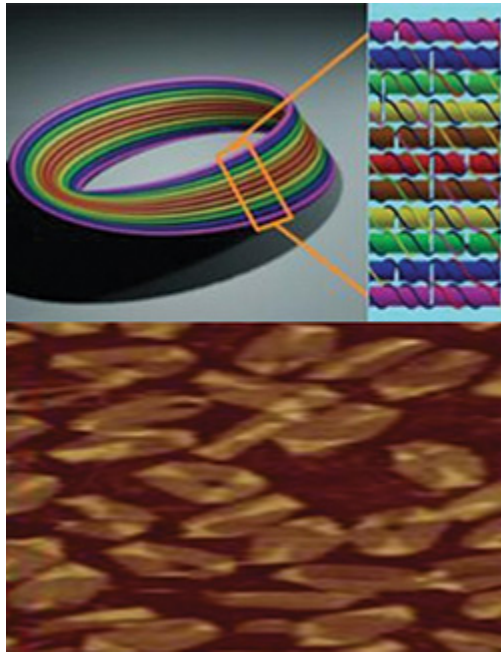


Figure 16 Typical nano architectures of a Möbius DNA strip: colored Möbius strip (top left) strip section (top right) and DNA image (bottom).²⁹

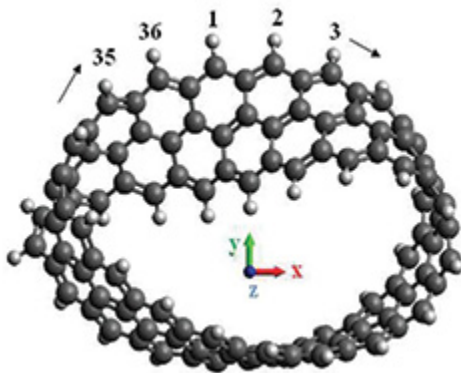
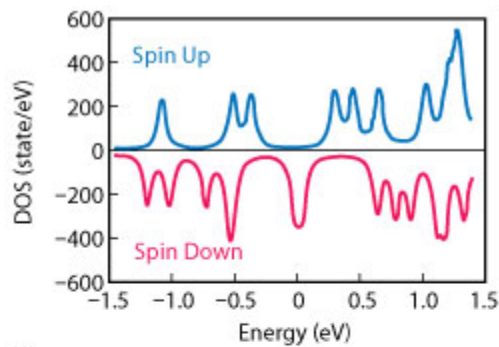


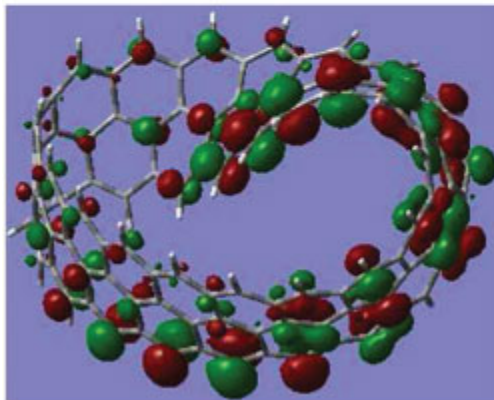
Figure 17 Graphene Möbius structure with length $L = 18$ and width $N = 3$. Möbius axis and edge C atom index are shown.³¹

From Equation 2, the properties of the Möbius transformation $f(z)$ are

Ulrich L. Rohde, Federal Armed Forces University,
Munich, Germany ; Ajay K. Poddar, Synergy
Microwave, NJ



(a)



(b)

Figure 18 Spin-dependent density of states of graphene Möbius strip as a function of electron energy (a) and molecular orbital at $E=0$ eV (b).³¹

(i) $f(z)$ can be expressed as a composition of affine transformations (scaling: $z \rightarrow tz$, translation: $z \rightarrow z+p$, rotation: $z \rightarrow e^{i\theta} z$, complex conjugation: $z \rightarrow \bar{z}$, inversion: $z \rightarrow \frac{1}{z}$), where $t, p \in \mathbb{C}$

(ii) $f(z)$ maps \mathbb{C} one-to-one onto itself, and is continuous

(iii) $f(z)$ maps circles and lines to circles and lines

(iv) $f(z)$ is conformal

From (i)-(iv), the family of functions is the composition of functions; the identity element is the identity map, and the inverse is given by inverse function. The Möbius group consists of those fractional linear transformations that map the open unit disk $D=\{z \in \mathbb{C}: |z| < 1\}$ to itself in a one-to-one way. These transformations and their inverses are analytic on D and map its boundary, the unit circle $S^1=\{z \in \mathbb{C}: |z| = 1\}$ to itself. The automorphism of the disk is in the form:

Ulrich L. Rohde, Federal Armed Forces University, Munich, Germany ; Ajay K. Poddar, Synergy Microwave, NJ

$$f(z) = e^{j\varphi} \frac{\alpha - z}{1 - \bar{\alpha}z} \quad (3)$$

$$z = M(w) = \frac{e^{j\psi} w + \alpha}{1 - \bar{\alpha}e^{j\psi} w} \quad (4)$$

$$w = M^{-1}(z) = e^{-j\psi} \frac{z - \alpha}{1 - \bar{\alpha}z} + \alpha \quad (5)$$

where $\varphi \in \mathbb{R}$, $\psi \in \mathbb{R}$, and $\alpha \in \mathbb{D}$.

From Equations 1 through 5, the Möbius transformation can be used to achieve Möbius metamaterial symmetry, which has received widespread interest in the field of metamolecules, optical polarization, DNA sensing and high frequency components for energy saving electronics and instrumentation.²⁶⁻³⁵

EXAMPLES: MÖBIUS METAMATERIAL SYMMETRY

Benzene Metamolecules

The EM symmetry discovered in metamaterial is equivalent to the structural symmetry of a Möbius strip, with the number of twists controlled by the sign change of the electromagnetic coupling between the meta-atoms. **Figure 14** illustrates metamaterial Möbius symmetry in metals and dielectrics.²⁷ As shown in Figure 14, the hyperspace Möbius mechanism transforms ordinary benzene molecules into metamolecules with Möbius symmetry; “the topological phenomenon that yields a half-twisted strip with two surfaces but only one side.” The prototype of the metamolecular trimmer shown in Figure 14 is a 3-body system like a trimmer; metallic resonant meta-atoms configured as coupled split ring resonators (symbolized as metamolecules) exhibiting topological Möbius cyclic symmetry (C_3 -symmetry) through three rotations of 120 degrees. Möbius twists result from a change in the signs of the electromagnetic coupling constants between the constituent meta-atoms.²⁷ The interesting phenomena is that “different coupling signs exhibit resonance frequencies that depend only on the number of turns but not the locations of the twists,” thus confirming its Möbius symmetry.

Ulrich L. Rohde, Federal Armed Forces University,
Munich, Germany ; Ajay K. Poddar, Synergy
Microwave, NJ

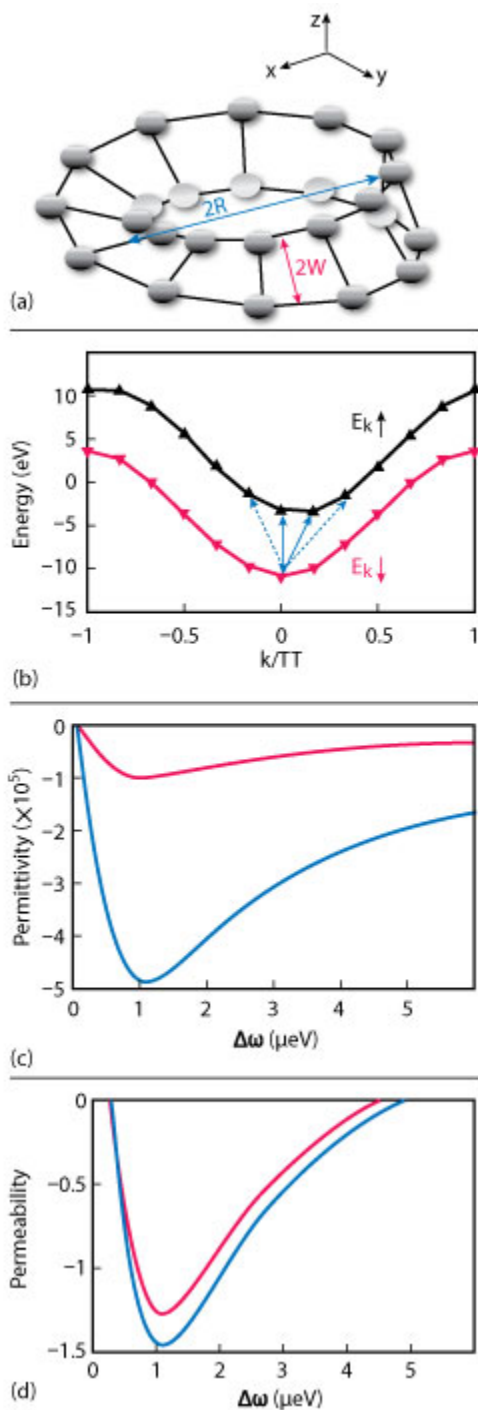


Figure 19 Möbius molecular rings made of carbon atoms (a) energy spectra $E_{k\sigma}$ of the molecular ring (b) relative permittivity as a function of $\Delta\omega$ (c) and relative permeability as a function of $\Delta\omega$ (d).³²

Polarized Light

Ulrich L. Rohde, Federal Armed Forces University, Munich, Germany ; Ajay K. Poddar, Synergy Microwave, NJ

Figure 15 illustrates the artificial Möbius strip formed by EM waves, which demonstrates that “a light-beam can be controlled so that its polarization twists follow a contour of Möbius strips.”²⁸ The creation of EM waves around a Möbius contour is interesting for improving the fundamental understanding of optical polarization and the complex light beam engineering needed for developing optical micro- and nano-fabrication structures for sub-wavelength imaging. As shown in Figure 15, the typical Möbius strip surface consists of polarized states of a light beam, with a non-vanishing curvature, and exhibiting spatial symmetry.

DNA Strip Sensor

Figure 16 shows the nano-architectures of a Möbius DNA strip in which each colored band represents a different DNA double helix. Such nano-architectures can be used in high sensitivity biological and chemical sensing devices.²⁹

MMI Graphene

Graphene has received extensive attention recently due to its remarkable structural and superior electronic and optical properties.³⁰ A single layer of graphite exhibits mechanical properties like thin paper or plastic with large bulk modulus along the graphene plane and is easily bent or curved. This unique characteristic allows graphene to wrap into carbon nanotubes without deformation and qualifies its use as a material for the construction of Möbius strips for microwave and optical components. The bandgap and cohesive energy of Möbius graphene as depicted in **Figure 17** depends on the width of the strip, and is augmented by increasing the width, as described by³¹

$$E_{CO}^{r(M)} = \frac{E_{SCF}^{r(M)} - N_C \times E_{SCF}^C - N_H \times E_{SCF}^H}{\Sigma(N_C + N_H)} \quad (6)$$

where the superscript $r(M)$ corresponds to the graphene ribbon (Möbius strip), N_C is the number of carbon atoms, N_H is the number of hydrogen atoms, $E_{CO}^{r(M)}$ is the self-consistent field energy of the graphene ribbon, and E_{SCF}^C and E_{SCF}^H are the self-consistent field energy of the carbon and hydrogen atoms, respectively.

The magnetic moment and spin-properties of Möbius graphene are interesting. A graphene Möbius strip maintains its metallic surface states in the presence of an external electric field. For sufficiently higher applied electric field, spin flipping can take place in the Möbius strip. In contrast with graphene nanoribbons, graphene Möbius strips show half-semiconducting properties when an external electric field is applied. **Figure 18** shows the typical orbital of a graphene Möbius strip and spin dependent density of states (DOS). The ferromagnetism and spin-flipping properties of Möbius graphene are attractive for spintronic devices and quantum oscillator applications.³¹

Figure 19 shows the characteristics of Möbius molecular rings that support metamaterial applications (negative permittivity ϵ and negative permeability).³² Two energy bands are denoted by their different pseudo spin labels $\sigma = \uparrow$ and \downarrow . Detuning $\Delta\omega = \omega - \Delta_0$.³² The difference between the Möbius molecular ring and the common annulenes lies in the boundary condition. The negative

Ulrich L. Rohde, Federal Armed Forces University, Munich, Germany ; Ajay K. Poddar, Synergy Microwave, NJ

index properties offer remarkable properties such as image cloaking, sub-wavelength imaging and enhancement of evanescent fields resulting in improved Q-factor.

Figure 20 depicts the application of graphene Möbius strips for the realization of microelectronic components.³⁰⁻³⁵ It illustrates the next generation microwave components realized by Möbius metamaterial strips through the electromagnetic coupling dynamics governed by the Möbius transformation.

As shown in Figure 20, cylindrical closed ring structures formed by graphene nanoribbons possessing two edges exhibit anti-ferromagnetic (zero-magnetic moment), whereas Möbius closed-ring strips formed by graphene nanoribbons possessing a single-edge exhibit ferromagnetism (nonzero magnetic moment). Graphene nanoribbons with a 'zigzag' edge structure exhibit magnetism at their edges. The most stable configuration of these ribbons is anti-ferromagnetic, so that magnetic moments at opposite edges point in opposite directions, reducing the total magnetic moment of the ribbons to zero. However, a graphene Möbius strip has only one continuous edge, hence no magnetic cancellation between the opposite edges, resulting in a nonzero magnetic moment.

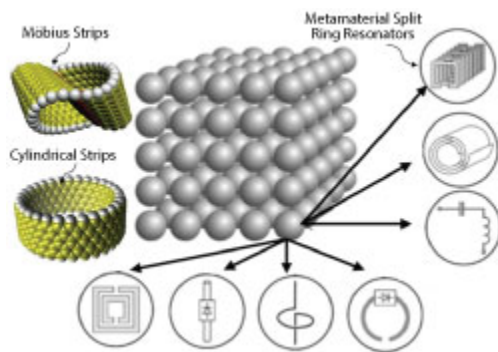


Figure 20 Structures of Möbius metamaterial strips formed by graphene for the realization of microelectronic components.³⁰

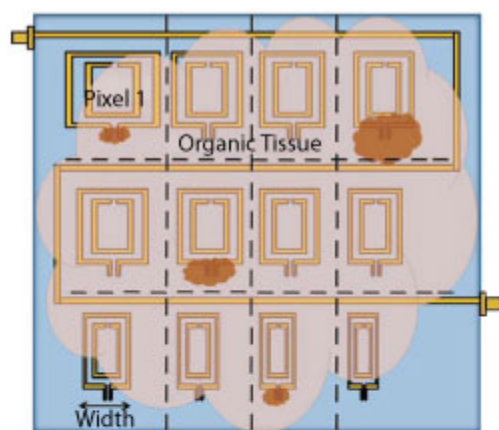
Medical Telemetry

Medical telemetry systems have considerably increased due to the inevitability for early diagnoses of diseases and continuous monitoring of physiological parameters. Microwave antennas and sensors are key components of these telemetry systems since they provide the communication between the patient and base station. The Industrial, Scientific and Medical (ISM) radio bands are portions of the radio spectrum reserved internationally for the use of RF energy for industrial, scientific and medical purposes other than communications. Through the use of metamaterial like EBG structures in slotted microstrip antennas, increased efficiency and better return loss characteristics can be achieved.³⁶

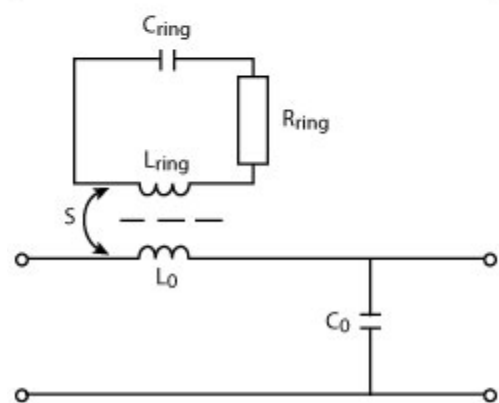
Cancer is the uncontrolled growth of abnormal (malignant) cells. Integrating microwave designs with metamaterial-inspired structures can lead to cost-effective devices that can localize abnormalities within the human body with high precision. The basic principle behind cancer detection is that small changes in the water content of biological tissues produces changes in their permittivities (ϵ) and conductivities (σ).³⁷ Malignant cells have significantly higher water content than normal tissues.

Ulrich L. Rohde, Federal Armed Forces University, Munich, Germany ; Ajay K. Poddar, Synergy Microwave, NJ

Hence the permittivity and conductivity of a tumor are higher than those ones of normal tissues at microwave frequencies. A proposed biosensor consists of an array of complementary metallic metamaterial resonators. The reason for choosing split ring resonators (SRR) is their strong response to an electromagnetic field.³⁷ An electromagnetic source generates an electromagnetic wave impinging on a metamaterial array and a detector is placed so as to detect the signal after the array. The biosensor without any material under test has a specific resonant frequency.³⁷ The variation in permittivity of the material under test, acts on the capacitance of the resonators, shifting with high sensitivity the sensor resonant frequency. Thus the shift in resonant frequency and the shape of the response is extremely useful for tumor detection. **Figure 21a** shows a typical metamaterial-inspired coupled SRR based sensor comprising 12 SRRs. **Figure 21b** represents a pixel within the sensor.



(a)



(b)

Figure 21 Metamaterial inspired microstrip coupled SRR sensor array (a) and equivalent circuit of a SRR loaded microstrip element (b).²⁷⁻²⁸

If, for example, an organic tissue, interacts with the outer split of a SRR it changes its capacitance value due to a change of effective permittivity. In this way, differences in tissues, such as abnormalities, can be detected.³⁸ The equivalent circuit of a microstrip line loaded with a single SRR for the quasi-static case is shown in Figure 21b.³⁹ The SRR is magnetically coupled to the

Ulrich L. Rohde, Federal Armed Forces University, Munich, Germany ; Ajay K. Poddar, Synergy Microwave, NJ

transmission line with the coupling factor S , where L_o and C_o correspond to the total SRR inductance and capacitance, respectively. The equivalent circuit yields the effective permeability with Lorentz dispersion⁴⁰

$$\mu_{\text{eff}} = -j \frac{Z_1}{\omega p} = \frac{L_o}{p} \left(1 + \frac{\omega^2 S^2}{\omega_{Om}^2 - \omega^2 + j\omega\delta} \right) \quad (7)$$

with p being the net cell length.

Acoustic Imaging

Acoustic imaging tools are used in both medical diagnostics and in testing the structural integrity of everything from airplanes to bridges. Medical personnel and structural engineers often need to focus sound for imaging or therapeutic purposes. Metamaterial gives researchers more control over the angle at which acoustic waves can pass through it. **Figure 22** shows a typical metamaterial inspired acoustic hyperbolic structure made of paper and aluminum for acoustic imaging application. The acoustic hyperbolic metamaterial (AHM) structure allows manipulation of acoustic waves to more than double the resolution of acoustic imaging by focusing acoustic waves and controlling the angles at which sound passes through the metamaterial.⁴¹ It interacts with acoustic waves in two different ways. From one direction, it exhibits a positive density and interacts with acoustic waves normally, just like air. But from a perpendicular direction, the metamaterial exhibits a negative density. This effectively makes acoustic waves bend at angles that are the exact opposite of what basic physics predicts. This has some very useful applications. For one, it can be used to improve acoustic imaging. Traditionally, acoustic imaging cannot achieve image resolution smaller than half of a sound's wavelength. For example, an acoustic wave of 100 kHz, traveling through air has a wavelength of 3.4 mm, limiting image resolution to 1.7 mm.

CONCLUSION

The unique features of MMI structures open the gateway to new inventions, recurring in an endless fashion; one could say that the future has the form of an MMI surface. In this article, the Casimir effect is discussed briefly. Details of the Casimir effect and applications using MMI structures for futuristic applications will be discussed in parts 2 and 3.

References

Ulrich L. Rohde, Federal Armed Forces University,
Munich, Germany ; Ajay K. Poddar, Synergy
Microwave, NJ

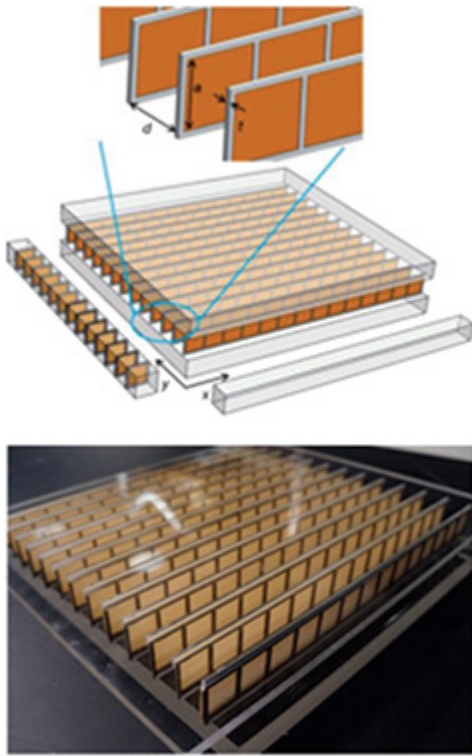


Figure 22 Physical structure of acoustic hyperbolic metamaterial.

1. U. L. Rohde and A. K. Poddar, "Möbius Strips and Metamaterial Symmetry: Theory and Applications," *Microwave Journal*, Vol. 11, No. 57, November 2014, pp. 76–88.
2. U. L. Rohde and A. K. Poddar, "Metamaterial Resonators: Theory and Applications," *Microwave Journal*, Vol. 57, No. 2, December 2014, p. 74.
3. U. L. Rohde and A. K. Poddar, "Metamaterial Möbius Strip Resonators for Tunable Oscillators, Part 3," *Microwave Journal*, Vol. 58, No. 1, January 2015, p. 64.
4. A. Poddar, "Slow Wave Resonator Based Tunable Multi-Band Multi-Mode Injection-Locked Oscillator," Habil Thesis, BTU Cottbus, Germany, 2014.
5. U. L. Rohde, A. K. Poddar and D. Sundarajan, "Real Time Signal Retention Device Using Co-Planar Waveguide (CPW) as Möbius Strip," *IEEE MTT-S Digest*, June 2013, pp. 1–3.
6. U. L. Rohde, A. K. Poddar and D. Sundarajan, "A Novel Möbius-Coupled Printed Resonator Based Signal Sources," *IEEE MTT-S Digest*, June 2013, pp. 1–3.
7. C. Caloz, "Perspectives on EM Metamaterials," *Materials Today*, Vol. 12, No. 3, March 2009, pp. 12–20.
8. C. Caloz, "Tomorrow's Metamaterials: Manipulation of Electromagnetic Waves in Space, Time and Space-time," February 2016, <http://arxiv.org/pdf/1602.04340.pdf>.
9. A. Lambrecht, "The Casimir Effect: A Force From Nothing," *Physics World*, September 2002, <https://www.physics.ohio-state.edu/~jay/631/Casimir%20effect.pdf>.
10. R. Zeng, Y. Chen and Y. Yang, "Stable Multilayer Structure Based on Restoring Casimir Forces," *European Physical Journal B*, Vol. 86, No. 398, September 2013, pp. 1–6.

Ulrich L. Rohde, Federal Armed Forces University, Munich, Germany ; Ajay K. Poddar, Synergy Microwave, NJ

11. F. Intravaia and C. Henkel, "Can Surface Plasmons Tune the Casimir Forces Between Metamaterials?," *New Frontiers in Casimir Force Control*, Poster, September 2009, <http://cnls.lanl.gov/casimir/PostersSF/Intravaia-SantaFe-poster.pdf>.
12. U. Leonhardt and T. G. Philbin, "Quantum Levitation by Left-Handed Metamaterials," *New Journal of Physics*, Vol. 9, August 2007.
13. J. Q. Quach, "Gravitational Casimir Effect," *Physical Review Letters*, Vol. 114, February 2015.
14. "Internet of Things," Wikipedia, https://en.wikipedia.org/wiki/Internet_of_Things.
15. C. Caloz, "Metamaterial Dispersion Engineering Concepts and Applications," *Proceedings of the IEEE*, Vol. 99, No. 10, October 2011, pp. 1711–1719.
16. B. E. A. Saleh and M. C. Teich, *Fundamentals of Photonics*, 2nd ed., Wiley, 1964, Chap. 22.
17. C. Caloz, S. Gupta, Q. Zhang and B. Nikfal, "Analog Signal Processing," *IEEE Microwave Magazine*, Vol. 14, No. 6, September 2013, pp. 87–103.
18. "ESTCube-1," Wikipedia, <https://en.wikipedia.org/wiki/ESTCube-1>.
19. "Hermes CubeSat Mission," Earth Observation Portal, <https://directory.eoportal.org/web/eoportal/satellite-missions/h/hermes>.
20. "CubeSats," NASA, www.nasa.gov/mission_pages/cubesats/index.html.
21. "NASA CubeSat launch," Southgate Amateur Radio News, http://southgatearc.org/news/january2010/nasa_cubesat_launch.htm.
22. G. L. Skrobot, "Project ElaNa and NASA's CubeSat Initiative," *Proceedings of the Cal Poly 2010 CubeSat Developer's Workshop*, April 2010.
23. O. Ceylan, A. Caglar, H. B. Tugrel, H. O. Cakar, A. O. Kislal, K. Kula and H. B. Yagci, "Small Satellites Rock," *IEEE Microwave Magazine*, Vol. 17, No. 3, March 2016, pp. 26–33.
24. "Metamaterials Approach Makes Better Satellite Antennas," phys.org, January 2011, <http://phys.org/news/2011-01-metamaterials-approach-satellite-antennas.html>.
25. E. Hückel, "Grundzüge der Theorie Ungesättigter und Aromatischer Verbindungen," *Zeitschrift für Elektrochemie und Angewandte Physikalische Chemie*, Vol. 43, No. 9, September 1937, pp. 77–85.
26. S. A. Marvel, R. E. Mirolo and S. H. Strogatz, "Identical Phase Oscillators with Global Sinusoidal Coupling Evolve by Möbius Group Action," *American Institute of Physics*, Vol. 19, No. 4, October 2009, pp. 043104-1-11.
27. C.W. Chang, M. Liu, S. Nam, S. Zhang, Y. Liu, G. Bartal, and X. Zhang, "Optical Möbius Symmetry in Metamaterials," *Physical Review Letters*, Vol. 105, December 2010, pp. 23550-1–4.
28. T. Bauer¹, P. Banzer, E. Karimi, S. Orlov, A. Rubano, L. Marrucci, E. Santamato, R. W. Boyd and G. Leuchs, "Observation of Optical Polarization Möbius Strips," *Science*, Vol. 347, No. 6225, February 2015, pp. 964–966.
29. D. Han, S. Pal, Y. Liu and H. Yan, "Folding and Cutting DNA into Reconfigurable Topological Nanostructures," *Nature Nanotechnology*, Vol. 5, October 2010, pp. 712–717.
30. X. Wang, X. Zheng, M. Ni, L. Zou and Z. Zeng, "Theoretical Investigation of Möbius Strips Formed from Graphene," *Applied Physics Letters*, Vol. 97, September 2010.
31. H. Mazidabadi, H. Simchi and M. Esmaeilzadeh, "Electronic and Magnetic Properties of Graphene Möbius Strips: Density Functional Theory Approach," *Journal of Nanoscience and Nanotechnology*, Vol. 3, No. 5, September 2014, pp. 268–273.
32. Y. N. Fang, Y. Shen, Q. Ai and C. P. Sun, "Negative Refraction Induced by Möbius Topology," *Cornell University Library*, January 2015.

Ulrich L. Rohde, Federal Armed Forces University, Munich, Germany ; Ajay K. Poddar, Synergy Microwave, NJ

33. A. Poddar, "Slow Wave Resonator Based Tunable Multi-Band Multi-Mode Injection-Locked Oscillator," *Habil Thesis, BTU Cottbus, Germany*, 2014.
34. G. Li and E. Afshari, "A Low Phase Noise Multi-Phase Oscillator Based on Left-Handed LC-Ring," *IEEE Journal of Solid State Circuits*, JSSC. Vol. 45, No. 9, September 2010, pp. 1822–1833.
35. A. Rofougaran, J. Rael, M. Rofougaran and A. Abidi, "A 900 MHz CMOS LC Oscillator with Quadrature Outputs," *IEEE International Solid State Circuits Conference*, February 1996, pp. 392–393.
36. H. Kumar, R. K. Kanth, P. Liljeberg and H. Tenhunen, "Metamaterial Based Slotted Patch Antenna," *IEEE 10th International Conference on Telecommunication in Modern Satellite Cable and Broadcasting Services*, Vol. 1, October 2011, pp. 43–46.
37. L. La Spada, F. Bilotti and L. Vegni, "Metamaterial Biosensor for Cancer Detection," *IEEE Sensors*, October 2011, pp. 627–630.
38. M. Puentes, M. Maasch, M. Schubler and R. Jakoby, "Frequency Multiplexed 2-Dimensional Sensor Array Based on Split-Ring Resonators for Organic Tissue Analysis," *IEEE Transactions on Microwave Theory and Techniques*, Vol. 60, No. 6, June 2012, pp. 1720–1727.
39. J. Baena, J. Bonache, F. Martin, R. Sillero, F. Falcone, T. Lopetegi, M. Laso, J. Garcia-Garcia, I. Gil, M. Portillo and M. Sorolla, "Equivalent Circuit Models for Split-Ring Resonators and Complementary Split-Ring Resonators Coupled to Planar Transmission Lines," *IEEE Transactions on Microwave Theory and Techniques*, Vol. 53, No. 4, April 2005, pp. 1451–1461.
40. A. Trehan and N. Nikolova, "Summary of Materials and Recipes Available in the Literature to Fabricate Biological Phantoms for RF and Microwave Experiments," Ph.D. dissertation, McMaster University, ON, Canada, 2009.
41. C. Shen, Y. Xie, N. Sui, W. Wang, S. A. Cummer and Y. Jing, "Broadband Acoustic Hyperbolic Metamaterial," *Physical Review Letters*, Vol. 115, December 2015.

Möbius Metamaterial Inspired Signal Sources and Sensors

Metamaterial Möbius strips (MMS) have captured the interest of research scientists because of their distinctive properties, such as topological symmetry, which is conserved when the system undergoes an alteration such as deformation, twisting and stretching; and a negative index of refraction (i.e., $n = -\sqrt{\epsilon\mu}$; $\epsilon < 0$, $\mu < 0$). **Figure 1** shows typical negative index ($\epsilon < 0$, $\mu < 0$) Möbius strips formed by graphene nano-ribbons that are used to create topologically-induced high Q-factor components with desirable electromagnetic properties. Unlike conventional materials, which interact with electromagnetic waves based on their chemical compositions, the properties of negative index

Ulrich L. Rohde, Federal Armed Forces University, Munich, Germany ; Ajay K. Poddar, Synergy Microwave, NJ

materials (NIM), otherwise known as metamaterials, come from their geometric topological structures.

NIMs, as shown in Figure 1, are artificial engineered topological structures intended to modify the bulk permeability and permittivity of the medium. This is realized by constraining the size of periodically unit cell NIMs structures size to typically less than the wavelength of incident EM waves. It is interesting to note that by changing the position, orientation and excitation of the NIMs structures, important parameters such as permittivity, permeability, refractive index, transmission, reflection, impedance and coupling can be tuned and optimized for desired applications. There are many ways to vary the properties of NIMs, such as using ferrites, liquid crystals, frequency-selective surfaces and hybrid-NIMs, or by manipulating their lattice structures.

Figure 2 shows the typical characteristics of a medium that explains the properties of natural and artificially engineered composite material.¹ The third quadrant describes the properties of a left-handed medium that posses NIM characteristics. The evanescent-mode energy storage and resonance characteristics of the third-quadrant material enables potential applications in electronics, medical, space and optics. Hence, it is important to understand its fundamental EM dynamics for the design of NIMS resonator based electronic signal sources. It is important to note that exact characterization of ϵ and μ of a NIM structure is a challenging task for wideband frequency operation.

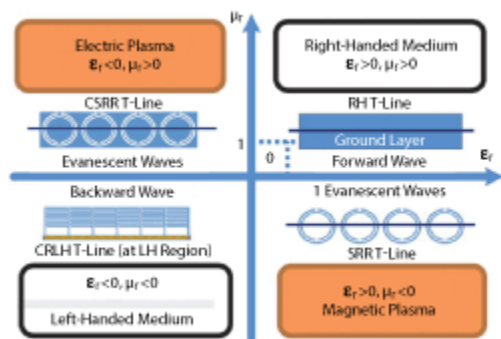


Figure 2 Typical representation of a medium; the third quadrant explains NIM properties.

In addition to this, the justification for using effective constitutive parameters ($\epsilon < 0$, $\mu < 0$) provides a convenient means to understand the behavior of the artificially engineered NIM structures without considering, in detail, the local EM-field distribution. To establish faithful values for these parameters, numerous methods have been reported, but none of them provide exact solutions because of hypotheses concerning the NIM's tiny size, and they neglect coupling. The general isotropic medium model assumes that the induced electric and magnetic dipoles are mutually independent, but in reality this is not always the case. NIMs are intrinsically anisotropic and sometimes bi-anisotropic because of the geometry and orientations of their structures.

For example, split rings (SR) as shown in **Figure 3**, typically used in NIMs, exhibit simultaneous electric and magnetic responses; i.e., their corresponding dipoles are coupled.⁵ This leads to cross coupling between the electric and magnetic field in SR inspired NIM structures. Therefore, it is not recommended to discount the magneto-electric coupling that depends on the shape of inclusions,

Ulrich L. Rohde, Federal Armed Forces University, Munich, Germany ; Ajay K. Poddar, Synergy Microwave, NJ

wave polarizations, excitation and orientation of NIM structures. To account for both asymmetric reflection and magneto-electrical coupling, the bi-anisotropic medium model can be used.

Figure 3 shows typical NIM circular and square split ring structures. Their sizes and the distances between them are kept smaller than a wavelength (λ). Under these conditions, an SR-NIM structure may present bulk properties that can be characterized by a macroscopic model, with parameters ϵ and μ . The expression n is given by

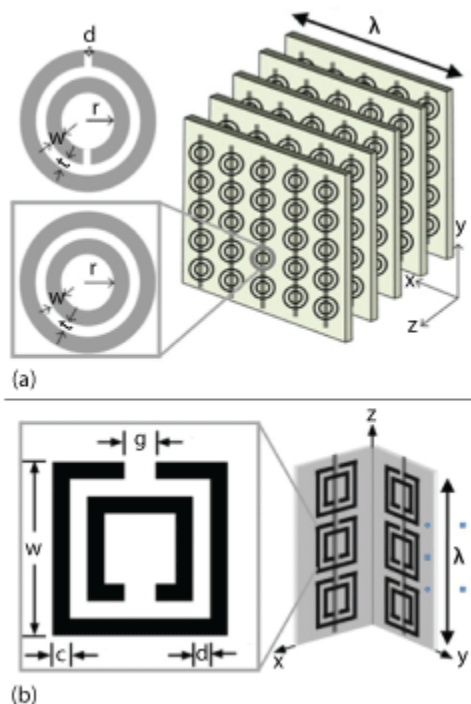


Figure 3 Typical SRRs and NIM construction with closed SRR wire structure: circular split ring (a) and rectangular split ring (b).

$$n = \pm\sqrt{(\pm\epsilon)(\pm\mu)} = \pm\sqrt{\mu\epsilon} \quad (1)$$

From (1), a positive sign is used for n when $\epsilon, \mu > 0$, whereas a negative sign is used when $\epsilon, \mu < 0$. The assumption of positive index ($n > 0$) implies that the index n is a scalar, and does not depend on frequency. But in reality, this is not always true. The energy of the field (W), where $W = \epsilon E^2 + \mu H^2$, would be a negative value when ϵ and μ are negative, and this is not possible; hence ϵ and μ are bound to depend on frequency and fall into complex domain.² The unified expression of energy W can be described by

$$W = \frac{\partial(\omega\epsilon)}{\partial\omega} E^2 + \frac{\partial(\omega\mu)}{\partial\omega} H^2 \quad (2)$$

where $\epsilon(\omega) = \epsilon'(\omega) + j\epsilon''(\omega)$ and

$$\mu(\omega) = \mu'(\omega) + j\mu''(\omega)$$

Ulrich L. Rohde, Federal Armed Forces University, Munich, Germany ; Ajay K. Poddar, Synergy Microwave, NJ

From (2), the electrodynamics of negative index materials ($n < 0$; $\epsilon < 0$ and $\mu < 0$) provide a positive W value for a very broad class of dispersive materials characterized by $\epsilon(\omega)$ and $\mu(\omega)$, exhibit dependency on frequency.

Any material supporting a single propagating mode at a known frequency usually exhibits well-defined n , whether the material is homogeneous/continuous or not. But it is not easy to assign z to a non-homogeneous material, because z strongly depends on the surface termination and overall size of the material.¹ The classical homogenization theories are typically valid when the unit-cell size is insignificant with respect to wavelength (the zero frequency limits) and thus might be expected to result in a poor description of negative index materials. The key supposition is, if the wavelength of the incident wave is much larger than the size and spacing between the NIM's unit cell elements then it is possible to perform homogenization, and to obtain a value of z within an acceptable range of error.^{2,3}

Assuming the size of a NIM structure is much smaller than $\lambda/10$, the homogenization theory can be applied to topology inspired Möbius strips. The averaging of Maxwell's equations over small volumes (with respect to a wavelength) can be performed to obtain an analogous uniform continuous harmonized medium described by effective constitutive parameters (ϵ and μ). It is possible to retrieve values for the complex n and z of inhomogeneous periodic negative index Möbius strips (NIMS) structures with prior information about the termination of the NIM unit cell, and the phases and amplitudes of the waves transmitted/reflected from the NIMS sample. The challenge is that if the NIMS structures are not symmetric along the wave propagation direction, two different values of z are retrieved corresponding to two incident directions of propagation. This ambiguity in the computation of z leads to a fundamental ambiguity in the definitions of ϵ and μ , which increases as the ratio of unit cell dimension to wavelength increases.

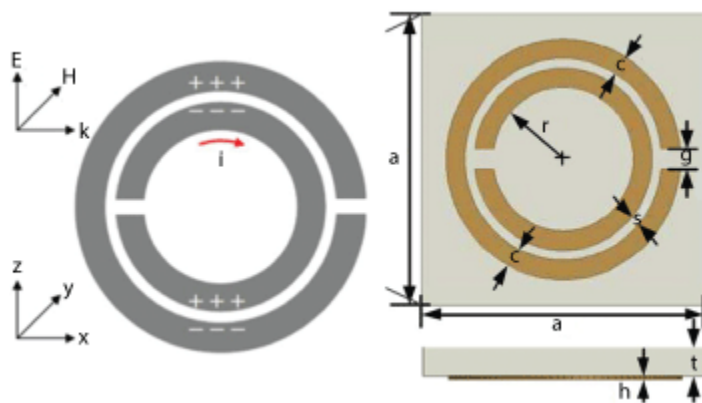


Figure 4 Typical SRR unit cell showing the inner and outer asymmetric rings.

The simplest theoretical formulation of a SR inspired NIM can be deduced from an equivalent circuit model that gives insight into the relationship between the physical properties and geometric parameters of SRRs as shown in **Figures 3 and 4**. Analytical values of the constitutive parameters (ϵ_{zz} , μ_{yy} , ξ_0) are given by^{5, 13, 17}

Ulrich L. Rohde, Federal Armed Forces University, Munich, Germany ; Ajay K. Poddar, Synergy Microwave, NJ

$$\varepsilon_z = 1 + \frac{1}{\varepsilon_0 a^3} \quad (3)$$

$$\left\{ \varepsilon_0 \frac{16}{3} r_{ext}^3 + 4d_{eff}^2 r_0^2 C_{pull}^2 L \left(\frac{\omega^2}{\omega_0^2 - \omega^2 - i\omega\gamma} \right) \right\}$$

$$\mu_y = 1 + \frac{\mu_0}{a^3} \left\{ \frac{\pi^2 r_0}{L} \left(\frac{\omega^2}{\omega_0^2 - \omega^2 - i\omega\gamma} \right) \right\} \quad (4)$$

$$\xi_0 = -i \sqrt{\frac{\mu_0}{\varepsilon_0 a^3}} \quad (5)$$

$$\left\{ -2ir_0^3 d_{eff} C_{pull} \frac{\omega_0^2}{\omega} \left(\frac{\omega^2}{\omega_0^2 - \omega^2 - i\omega\gamma} \right) \right\}$$

where $d_{eff} = c + s$, $\gamma = \frac{R}{L}$, $r_0 = r + c + s/2$ and $r_{ext} = r + 2c + s$; L and C_{pull} are the total inductance of the SRR and the capacitance between the rings respectively.

From the equivalent circuit model, RR behaves as a resonant LC circuit, and that the frequency of the resonance is given by

$$\omega_0^2 = \frac{1}{\left(\frac{1}{2} \pi r_0 C_{pull} + C_{gap} \right) L} \quad (6)$$

L and C_{pull} can be calculated from the analytical equations reported by Marques et al.¹⁷ C_{gap} is the capacitance of the gap, if the gap is narrow, its capacitance can be analytically written as¹⁸

$$C_{gap} = \frac{\varepsilon_0 c h}{g} + C_0 \quad \text{with} \quad (7)$$

$$C_0 = \varepsilon_0 (h + c + g)$$

From Marques et al.,¹⁷ $L = 3.9287 \times 10^{-9}$ H, $C_{pull} = 1.6806 \times 10^{-11}$ F, $C_{gap} = 4.1557 \times 10^{-15}$ F and $R = 0.4901 \Omega$ at the frequency of resonance. The poor accuracy of the analytical method for constitutive parameter calculation given in (3) through (7) and the deficiency in complex modeling of thicker structures limits its validation. The alternative approach is a retrieval technique based on the extraction of S-parameters. The advantage of the retrieval method is that it can be used for simulated and measured S-parameter data; thin samples (in the propagation direction) are preferred to minimize the errors.

In general there are three methods used for the determination of effective constitutive parameters based on applications and acceptable errors.³ The first method is to numerically calculate the ratios of the EM field inside NIM structure. This approach is good for numerical simulations, but not appropriate for experimental measurement.⁴ The second method calculates the effective constitutive parameters by using analytical models of NIM structures including the numerical averaging of fields; but, this technique is not suitable for complex NIM structures.⁵ The third method is a retrieval technique based on the inversion of scattering data (S-parameters) of a finite slab, called the Nicolson–Ross–Weir (NRW) procedure.^{6,7}

The NRW method was developed for the measurement of complex permittivity and permeability of natural materials and recently applied to NIMs.¹⁻²⁰ The problem with NRW method arises in cases

Ulrich L. Rohde, Federal Armed Forces University, Munich, Germany ; Ajay K. Poddar, Synergy Microwave, NJ

where topology-driven NIM structures undergo asymmetric reflections. Smith et al.,² reported a modified approach to resolve this issue of asymmetric reflections by using averaged values of reflection coefficients. The isotropic medium model cannot duplicate this property, as it is intrinsically symmetric, hence it is important to understand the EM dynamics of SR inspired NIM media that inherently possess reflection asymmetric structures ($S_{11} \neq S_{22}$).²¹

EM Dynamics of Media

The fundamental equations describing EM waves in a biaxial anisotropic medium (or simply called biaxial) are more complex than the isotropic equations. Isotropic materials have a single permittivity ϵ . In an isotropic media, the constitutive relations that relate the electric flux density $\bar{\mathbf{D}}$ to the electric field intensity $\bar{\mathbf{E}}$ and the magnetic flux density $\bar{\mathbf{B}}$ to the magnetic field intensity $\bar{\mathbf{H}}$ are given by

$$\bar{\mathbf{D}} = \epsilon \bar{\mathbf{E}} = \epsilon_0 \epsilon_r \bar{\mathbf{E}} ; \bar{\mathbf{B}} = \mu \bar{\mathbf{H}} = \mu_0 \mu_r \bar{\mathbf{H}} \quad (8)$$

From (8), ϵ describes the medium's electrical properties and μ describes its magnetic properties. The time-harmonic forms of Maxwell's equations for isotropic media are given by

$$\nabla \times \bar{\mathbf{E}} = -i\omega\mu\bar{\mathbf{H}} \quad (9)$$

$$\nabla \times \bar{\mathbf{H}} = i\omega\epsilon\bar{\mathbf{E}} + \bar{\mathbf{J}} \quad (10)$$

$$\nabla \cdot \bar{\mathbf{D}} = \rho_v \quad (11)$$

$$\nabla \cdot \bar{\mathbf{B}} = 0 \quad (12)$$

A medium is called electrically anisotropic if $\bar{\mathbf{D}} = \bar{\boldsymbol{\epsilon}} \cdot \bar{\mathbf{E}}$, where $\bar{\boldsymbol{\epsilon}}$ is the permittivity tensor. A medium is magnetically anisotropic if $\bar{\mathbf{B}} = \bar{\boldsymbol{\mu}} \cdot \bar{\mathbf{H}}$, where $\bar{\boldsymbol{\mu}}$ is the permeability tensor, note that $\bar{\mathbf{B}}$ and $\bar{\mathbf{H}}$ are no longer parallel. A medium can be both electrically and magnetically anisotropic. In the electrically anisotropic case, $\bar{\mathbf{D}}$ and $\bar{\mathbf{E}}$ are no longer parallel, and $\bar{\boldsymbol{\epsilon}}$ is given by

$$\bar{\boldsymbol{\epsilon}} = \begin{pmatrix} \epsilon_{xx} & \epsilon_{xy} & \epsilon_{xz} \\ \epsilon_{yx} & \epsilon_{yy} & \epsilon_{yz} \\ \epsilon_{zx} & \epsilon_{zy} & \epsilon_{zz} \end{pmatrix} \quad (13)$$

For example, crystals, in general, are described by a symmetric permittivity tensor; there always exists a coordinate transformation that transforms the symmetric matrix $\bar{\boldsymbol{\epsilon}}$ to a diagonal matrix as given by

$$\bar{\boldsymbol{\epsilon}} = \begin{pmatrix} \epsilon_{xx} & 0 & 0 \\ 0 & \epsilon_{yy} & 0 \\ 0 & 0 & \epsilon_{zz} \end{pmatrix} \quad (14)$$

From (14), the new coordinate system is called the principal system, and the three coordinate axes are called the principal axes. For a cubic crystal where $\epsilon_{xx} = \epsilon_{yy} = \epsilon_{zz} = \epsilon$, the crystal is isotropic.

Ulrich L. Rohde, Federal Armed Forces University, Munich, Germany ; Ajay K. Poddar, Synergy Microwave, NJ

$$\bar{\epsilon} = \begin{pmatrix} \epsilon & 0 & 0 \\ 0 & \epsilon & 0 \\ 0 & 0 & \epsilon \end{pmatrix} \quad (15)$$

For tetragonal, hexagonal and rhombohedra crystals two of the three ϵ are equal; such a crystal is called uniaxial. Uniaxial anisotropic materials have two different permittivity values. They have the same permittivity along two dimensions and a different permittivity along the third dimension. An unrotated uniaxial permittivity tensor can be written as

$$\bar{\epsilon} = \begin{pmatrix} \epsilon & 0 & 0 \\ 0 & \epsilon & 0 \\ 0 & 0 & \epsilon_{zz} \end{pmatrix} \quad (16)$$

From (16), the principal axis that is different (exhibits anisotropy) is called the optical axis (z-axis is the optical axis), and there exists a two dimensional degeneracy. If $\epsilon_{zz} > \epsilon$, the medium exhibits positive uniaxial behavior, and if $\epsilon_{zz} < \epsilon$, the medium shows negative uniaxial characteristics.

If $\epsilon_{xx} \neq \epsilon_{yy} \neq \epsilon_{zz}$, the crystal is biaxial. Examples of biaxial crystals are orthorhombic, monoclinic, and triclinic. The defining property of electrically biaxial media is the permittivity tensor $\bar{\epsilon}$.

If the medium is biaxial anisotropic, the permittivity and permeability of medium take on a tensor form. From (8), the set of matrix equations can be described by

$$\bar{D} = \bar{\epsilon} \cdot \bar{E} = \epsilon_0 \bar{\epsilon}_r \cdot \bar{E}; \bar{B} = \quad (17)$$

$$\bar{\mu} \cdot \bar{H} = \mu_0 \bar{\mu}_r \cdot \bar{H}$$

where $\bar{\epsilon}_r$ and $\bar{\mu}_r$ are relative permittivity and permeability tensors, respectively. From (17), the change in constitutive relations also affect Maxwell's equations (9)-(12) in the medium,

$$\nabla \times \bar{E} = -i\omega \bar{\mu} \bar{H} \quad (18)$$

$$\nabla \times \bar{H} = i\omega \bar{\epsilon} \bar{E} + \bar{J} \quad (19)$$

$$\nabla \cdot \bar{D} = \rho_V \quad (20)$$

$$\nabla \cdot \bar{B} = 0 \quad (21)$$

The NIM exhibits properties of a bi-anisotropic medium, provide coupling between electric and magnetic fields. The constitutive relations for a bi-anisotropic medium are given by

Ulrich L. Rohde, Federal Armed Forces University, Munich, Germany ; Ajay K. Poddar, Synergy Microwave, NJ

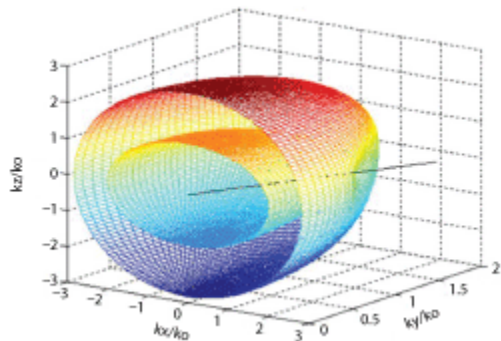


Figure 5 Wave vector surface: unrotated biaxial medium $(\epsilon_x, \epsilon_y, \epsilon_z) = (2, 8, 4)$, plotted over $0 \leq \theta \leq \pi$ and $0 \leq \phi \leq \pi$.

$$\vec{D} = \vec{\epsilon} \cdot \vec{E} + \vec{\xi} \cdot \vec{H} \quad (22)$$

$$\vec{B} = \vec{\mu} \cdot \vec{H} + \vec{\zeta} \cdot \vec{E} \quad (23)$$

A bi-anisotropic medium placed in an electric or magnetic field becomes both polarized and magnetized. Almost any medium in motion becomes bi-anisotropic. The first cases of bi-anisotropic materials were indeed moving dielectrics and magnetic materials in the presence of electric or magnetic fields. The topics of moving NIMs and their constitutive relations are the subject of relativistic electromagnetic theory, and can lead to Casimir effect (anti-gravity).¹⁵ The permittivity described in (16), represents an unrotated uniaxial medium with its optic axis along the z-direction.

Biaxially anisotropic materials have three unique values in the permittivity tensor and they have two optic axes. An unrotated biaxial permittivity tensor is given by

$$\epsilon_{ij} = \begin{pmatrix} \epsilon_x & 0 & 0 \\ 0 & \epsilon_y & 0 \\ 0 & 0 & \epsilon_z \end{pmatrix} \quad (24)$$

where $\epsilon_x \neq \epsilon_y \neq \epsilon_z$. From (8), principal axes of a biaxial medium are aligned with the Cartesian coordinate system.

For a better understanding, **Figure 5** shows the plots of the unrotated biaxial medium; the inner surface is called the “a-wave vector surface” and the outer surface is the “b-wave vector surface”. The intersecting line is one of the optic axes, it can be seen from Figure 5 that the optic axis intersects the wave vector surfaces at some point and the “b-wave wave vector surface” is at a local minimum at the point of intersection.¹⁰ If the biaxial medium is arbitrarily oriented with respect to the coordinate system, the permittivity tensor representation would be complex and not as simple described in (8).

Ulrich L. Rohde, Federal Armed Forces University, Munich, Germany ; Ajay K. Poddar, Synergy Microwave, NJ

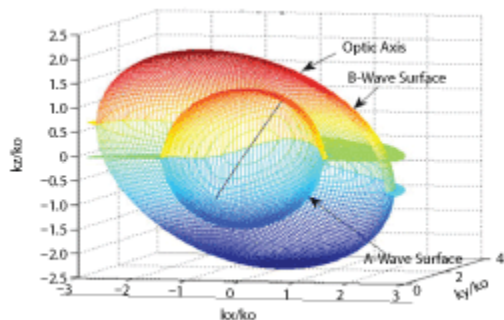


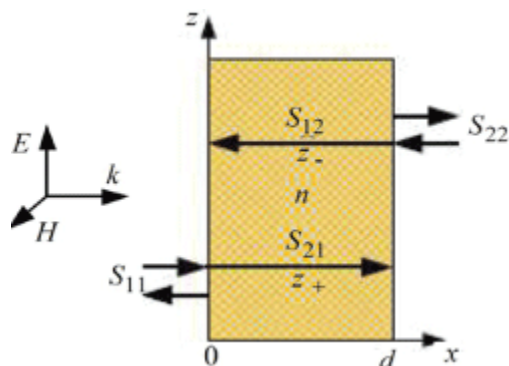
Figure 6 Wave vector surface: rotated biaxial medium $(\epsilon_x, \epsilon_y, \epsilon_z) = (2, 8, 4)$, rotated by $(\psi_1 \ \psi_2) = (30^\circ, 75^\circ)$.

The evaluation of the tensor for an arbitrarily oriented biaxial medium is given by applying rotations to the tensor in (8); the wave vector surfaces are shown in **Figure 6**. Studying the wave vector surfaces of the unbounded region shown in Figures 5 and 6 give insight into how the wave influences the important parameters (ϵ, μ, n, z) in the composite NIM structures, which are intrinsically anisotropic and sometimes bi-anisotropic due to geometry and structural orientations.

Constitutive Effective Parameters

Most of the NIMs presented over the past several years are artificially engineered SR-inspired periodic structures.¹⁻²⁷ It is convenient to extract the parameters from a unit cell of periodic structures through numerical approaches. It has been demonstrated that under the condition of long wavelength, a material with a periodic structure can be viewed as a homogeneous medium and its properties can be described by the effective medium parameters. The properties of a periodic structure can be determined from the transfer-matrix (T) associated with the fields of a unit cell.

NIM structures fall into the category of anisotropic and bi-anisotropic (cross-coupling exists between electric and magnetic fields in bi-anisotropic) due to their orientation and special geometric structures. When computing the effective parameters of NIM structures, magneto-electric coupling is a critical parameter. The simplified approach to retrieve the coupling parameter of a bi-anisotropic material from S-parameters is based on transfer-matrix method. The transfer-matrix method has been used to retrieve the effective EM parameters of homogeneous and non-homogeneous materials.^{1,2}



Ulrich L. Rohde, Federal Armed Forces University, Munich, Germany ; Ajay K. Poddar, Synergy Microwave, NJ

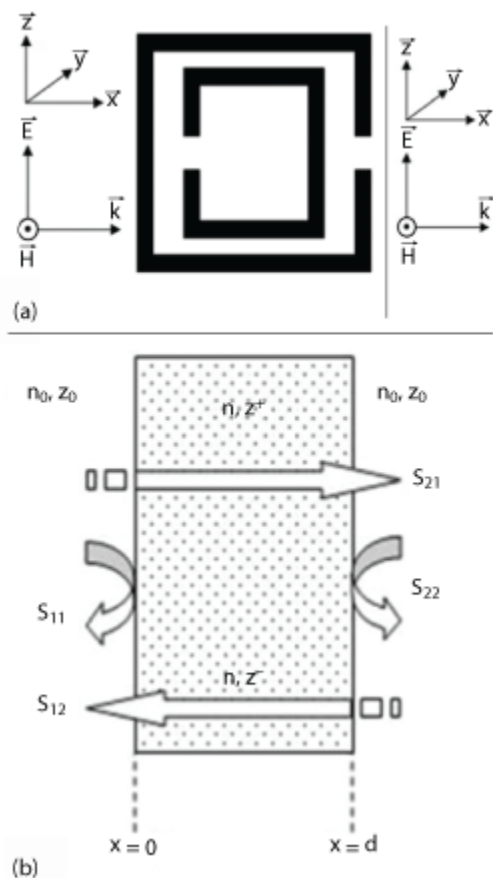
Figure 7 Plane wave incident in the x direction into a bi-anisotropic slab.¹³

Figure 7 shows a typical of bi-anisotropic slab of thickness d placed in air, illustrating the direction of S-parameters. For a material consisting of periodic structures, there is a phase advance per unit cell, which can be defined by the periodicity.¹³

Chen et al.,¹⁶ extracted effective constitutive parameters of bi-anisotropic negative index material from S-parameters for various wave polarizations using a numerical approach for a plane wave polarized in the z direction and incident in the x direction. Figure 8 shows the triplet $[\vec{k}_x, -\vec{H}_y, \vec{E}_z]$ based on a right-handed coordinate system, containing an electric and magnetic field.

As shown in Figure 8, the plane wave polarized in z- axis propagates along the x- direction, the electric fields in the z-direction will induce magnetic dipoles and the magnetic fields in the y- direction will induce electric dipoles due to the asymmetry of the inner and outer rings. It means that electric dipoles cannot only be excited by the E-fields but also by the H-fields. Similarly, magnetic dipoles cannot only be excited by the H-fields but also by the E-fields.

Assuming that medium is reciprocal and that the harmonic time dependence is $e^{-i\omega t}$, the constitutive relationships are given by¹⁹



Ulrich L. Rohde, Federal Armed Forces University, Munich, Germany ; Ajay K. Poddar, Synergy Microwave, NJ

Figure 8 Planar SRR structure (a) and homogeneous bi-anisotropic material slab suspended in air, with S-parameters used to determine forward and backward wave impedances (b).³

$$\vec{D} = \vec{\epsilon} \cdot \vec{E} + \vec{\xi} \cdot \vec{H} \quad (25)$$

$$\vec{B} = \vec{\mu} \cdot \vec{H} + \vec{\xi} \cdot \vec{E} \quad (26)$$

$$\vec{\epsilon} = \epsilon_0 \begin{pmatrix} \epsilon_{xx} & 0 & 0 \\ 0 & \epsilon_{yy} & 0 \\ 0 & 0 & \epsilon_{zz} \end{pmatrix}, \quad (27)$$

$$\vec{\mu} = \mu_0 \begin{pmatrix} \mu_{xx} & 0 & 0 \\ 0 & \mu_{yy} & 0 \\ 0 & 0 & \mu_{zz} \end{pmatrix}$$

$$\vec{\xi} = \frac{1}{c} \begin{pmatrix} 0 & 0 & 0 \\ 0 & 0 & 0 \\ 0 & -i\xi_0 & 0 \end{pmatrix}, \quad \vec{\zeta} = \frac{1}{c} \begin{pmatrix} 0 & 0 & 0 \\ 0 & 0 & i\xi_0 \\ 0 & 0 & 0 \end{pmatrix} \quad (28)$$

where \vec{E} , \vec{H} , and \vec{D} , are electric field, magnetic field intensity, and flux density; ϵ_0 and μ_0 are the permittivity and permeability in a vacuum; c is the speed of light in vacuum; and the other four quantities are dimensionless and are unknowns. When a plane wave polarized in the z -direction is incident in the x -direction, only two components of EM-fields (E_z and H_y) and three EM parameters (ϵ_{zz} , μ_{yy} , ξ_0) are included.

The numerical formulation is done for the determination of the forward and backward wave impedances entailed by parameters ϵ_{zz} , μ_{yy} and ξ_0 , since the unknown four quantities ϵ_{xx} , ϵ_{yy} , μ_{xx} , and μ_{zz} are not related to the bi-anisotropic structure in Figure 8b. From (18)-(19):

$$\frac{\partial^2 E_z}{\partial x^2} + k_x^2 E_z = 0, \quad \frac{\partial^2 H_y}{\partial x^2} + k_x^2 H_y = 0 \quad (29)$$

$$Z^+ = \frac{E^+}{H^+} = Z_0 \frac{\mu_{yy}}{(n+i\xi_0)} \quad (30)$$

$$Z^- = \frac{E^-}{H^-} = Z_0 \frac{\mu_{yy}}{(n-i\xi_0)}, \quad Z_0 = \sqrt{\frac{\mu_0}{\epsilon_0}} \quad (31)$$

$$z^\pm = \frac{Z^\pm}{Z_0}; \quad z^+ = \frac{Z^+}{Z_0}; \quad z^- = \frac{Z^-}{Z_0} \quad (32)$$

$$k_x^2 = k_0^2 (\epsilon_{zz} \mu_{yy} - \xi_0^2), \quad k_x = nk_0 \quad (33)$$

$$n^2 = \epsilon_{zz} \mu_{yy} - \xi_0^2, \quad n = \pm \sqrt{\epsilon_{zz} \mu_{yy} - \xi_0^2} \quad (34)$$

Ulrich L. Rohde, Federal Armed Forces University,
Munich, Germany ; Ajay K. Poddar, Synergy
Microwave, NJ

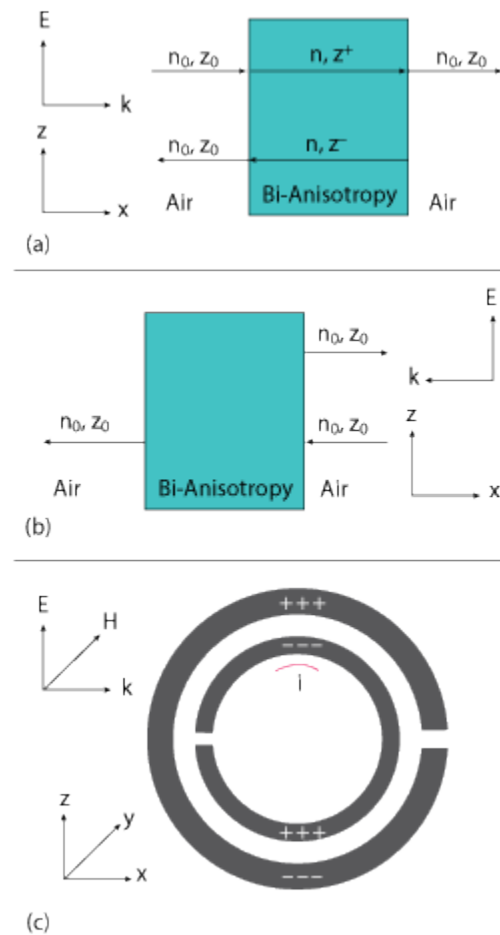


Figure 9 Signal flow of a homogeneous bi-anisotropic slab placed in open space, for the calculation of S-parameters for plane waves incident in the $+x$ (a) and $-x$ (b) directions; NIM unit cell (c).

where E_z and H_y are the z and y components of \vec{E} and \vec{H} ; k_x and k_0 are the wave number of the wave propagating in the x direction and in free-space, Z^+ and Z^- are wave impedances inside the medium for forward ($+\hat{x}$) and backward ($-\hat{x}$) propagations; z^+ and z^- are normalized (or non-dimensionalized) wave impedances in respective directions; Z_0 is the wave impedance (or intrinsic impedance) in air; and n is the refractive index of the negative index structure.

From (30),(31), bi-anisotropic NIM structure samples exhibit different values of wave impedances for forward and backward wave propagation.^{2,20} The non-homogeneous periodic NIM structure does not exhibit distinct impedance values because the ratio of E/\vec{H} varies periodically throughout the structure. This variation is negligible if the NIM structure unit cell sizes are small relative to a wavelength. It is important to note that the lack of a unique definition for z^\pm indicates that the values of ϵ and μ retrieved are not assignable but can be applied if the NIM formed by the periodic structure is always terminated in the same location of the unit cell. The surface termination has an increasing influence on the scattering properties of the structure as the scale of inhomogeneity increases relative to a wavelength.

Ulrich L. Rohde, Federal Armed Forces University, Munich, Germany ; Ajay K. Poddar, Synergy Microwave, NJ

It has been demonstrated that under the long wavelength condition, materials with periodic structures can be viewed as homogeneous and their properties can be described by the effective medium parameters. The properties of a periodic structure can be determined from the transfer-matrix (T) that is associated with the fields of a unit cell. We express the fields in the form of a vector $\mathbf{F} = \bar{\mathbf{F}} = (\bar{\mathbf{E}}, \bar{\mathbf{H}})^T$, where $\bar{\mathbf{E}}$ and $\bar{\mathbf{H}}$ are the complex amplitudes of the electric and magnetic fields located on the left-hand and right-hand faces of a slab. The magnetic field is a reduced field with the normalized form $\bar{\mathbf{H}} = i\omega\mu\bar{\mathbf{H}}$. The relations of fields on two sides of a slab can be expressed as

$$\bar{\mathbf{F}}(x+d) = e^{i\alpha d}\bar{\mathbf{F}}(x) = T\bar{\mathbf{F}}(x) \quad (35)$$

where α is the phase advance per unit cell which relates the fields on its two sides. T is the one dimensional transfer matrix of a NIM slab

$$T = \begin{pmatrix} T_{11} & T_{12} \\ T_{21} & T_{22} \end{pmatrix} = \begin{pmatrix} \cos(nk_0d) & -\frac{z}{k_0}\sin(nk_0d) \\ \frac{z}{k_0}\sin(nk_0d) & \cos(nk_0d) \end{pmatrix} \quad (36)$$

with k_0 being the wave number of light in free space, z being the wave impedance of a slab and n being the refractive index. From (35) and (36), the dispersion relation is given by solving

$$T_{11}T_{22} - e^{i\alpha d}(T_{11} + T_{22}) + e^{i2\alpha d} - T_{12}T_{21} = 0 \quad (37)$$

Ulrich L. Rohde, Federal Armed Forces University,
Munich, Germany ; Ajay K. Poddar, Synergy
Microwave, NJ

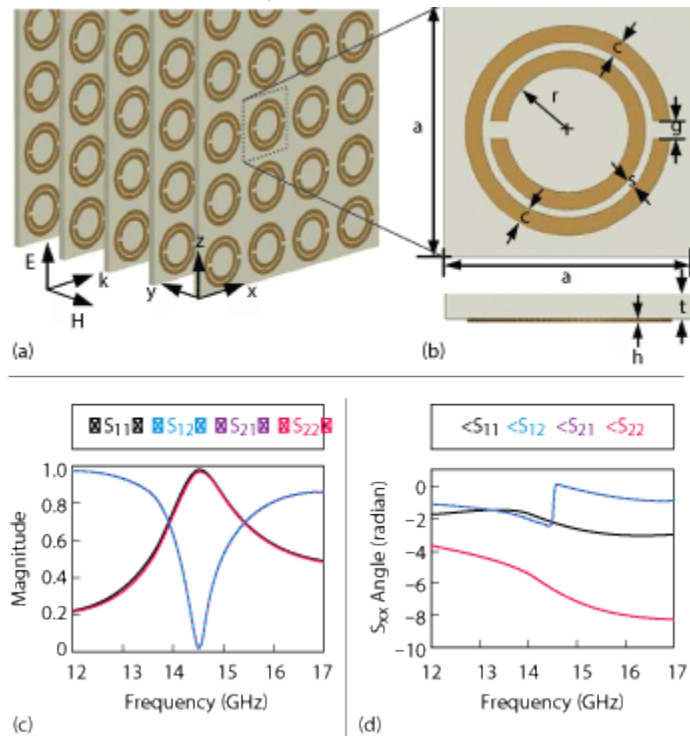


Figure 10 A typical bi-anisotropic structure: array of SRRs printed on substrate with metallization (a) SRR unit cell (b) magnitude (c) and phase (d) of S-parameters.¹³

The elements of the transfer matrix can be expressed in terms of S-parameters.

$$T_{11} = \frac{(1+S_{11})(1-S_{22})+S_{21}S_{12}}{2S_{21}} \quad (38)$$

$$T_{12} = \frac{(1+S_{11})(1+S_{22})-S_{21}S_{12}}{2S_{21}} \quad (39)$$

$$T_{21} = \frac{(1-S_{11})(1-S_{22})-S_{21}S_{12}}{2S_{21}} \quad (40)$$

$$T_{22} = \frac{(1-S_{11})(1+S_{22})+S_{21}S_{12}}{2S_{21}} \quad (41)$$

Figure 9 shows the schematics of a homogeneous bi-anisotropic material slab that is placed in an open space. There are two different situations to be considered, i.e., wave incidence in the +x and -x directions. After applying the boundary continuous conditions, it is easy to obtain the expressions for the S-parameters by using the transfer matrix method.²⁰ When the incidence is in the +x direction as shown in Figures 7 and 9a, the corresponding reflection (S₁₁) and transmission (S₂₁) coefficients are

Ulrich L. Rohde, Federal Armed Forces University,
Munich, Germany ; Ajay K. Poddar, Synergy
Microwave, NJ

$$S_{11} = \quad (42)$$

$$\frac{2i \sin(nk_0 l) [n^2 + (\xi_0 + i\mu_y)^2]}{[(\mu_y + n)^2 + \xi_0^2] e^{-ink_0 l} - [(\mu_y - n)^2 + \xi_0^2] e^{ink_0 l}}$$

$$S_{21} = \quad (43)$$

$$\frac{4\mu_y n}{[(\mu_y + n)^2 + \xi_0^2] e^{-ink_0 l} - [(\mu_y - n)^2 + \xi_0^2] e^{ink_0 l}}$$

where l is the thickness of the homogeneous bi-anisotropic material slab and k_0 is the wave number of light in free space. For the case when the incidence is in the $-x$ direction, as shown in **Figure 9b**, we obtain the corresponding reflection (S_{22}) and transmission (S_{12}) coefficients as

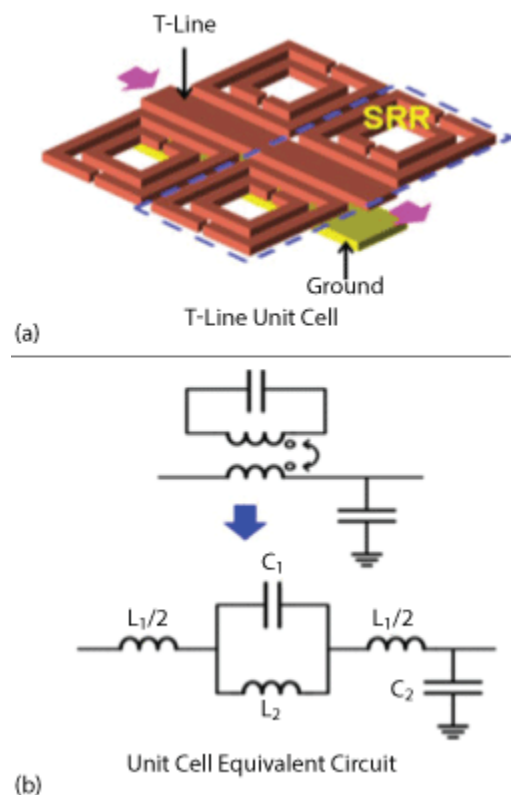


Figure 11 SRR loaded T-line unit cell (a) and equivalent lumped LC model (b)

Ulrich L. Rohde, Federal Armed Forces University,
Munich, Germany ; Ajay K. Poddar, Synergy
Microwave, NJ

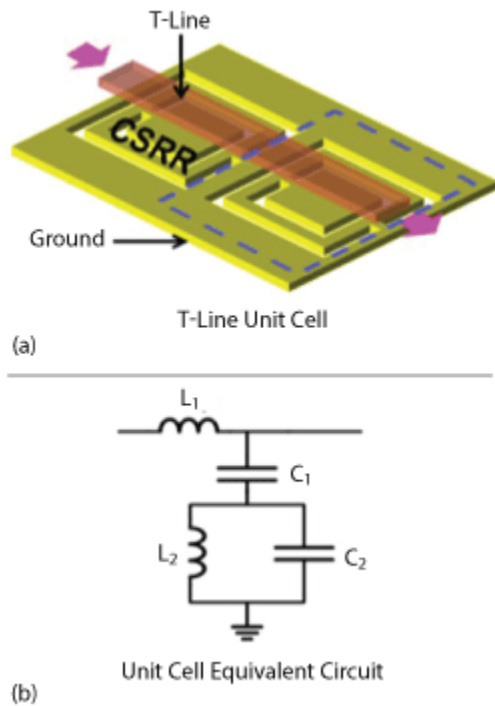


Figure 12 CSRR loaded T-line unit cell (a) and equivalent lumped LC model (b).

$$S_{12} = \frac{4\mu_y n}{[(\mu_y + n)^2 + \xi_0^2] e^{-in k_0 l} - [(\mu_y - n)^2 + \xi_0^2] e^{in k_0 l}} \quad (44)$$

$$S_{22} = \frac{2i \sin(n k_0 l) [n^2 + (\xi_0 - i\mu_y)^2]}{[(\mu_y + n)^2 + \xi_0^2] e^{-in k_0 l} - [(\mu_y - n)^2 + \xi_0^2] e^{in k_0 l}} \quad (45)$$

Ulrich L. Rohde, Federal Armed Forces University,
Munich, Germany ; Ajay K. Poddar, Synergy
Microwave, NJ

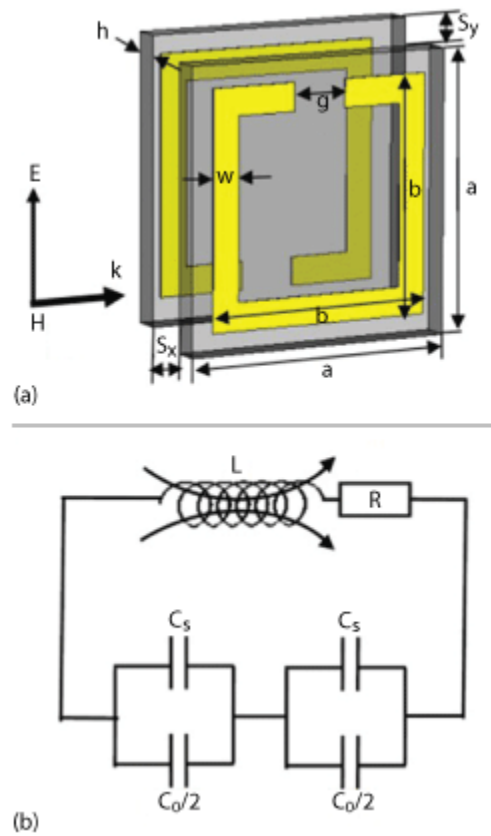


Figure 13 Typical broadside-coupled split ring resonator (a) and equivalent lumped circuit representation (b).²²

Ulrich L. Rohde, Federal Armed Forces University,
Munich, Germany ; Ajay K. Poddar, Synergy
Microwave, NJ

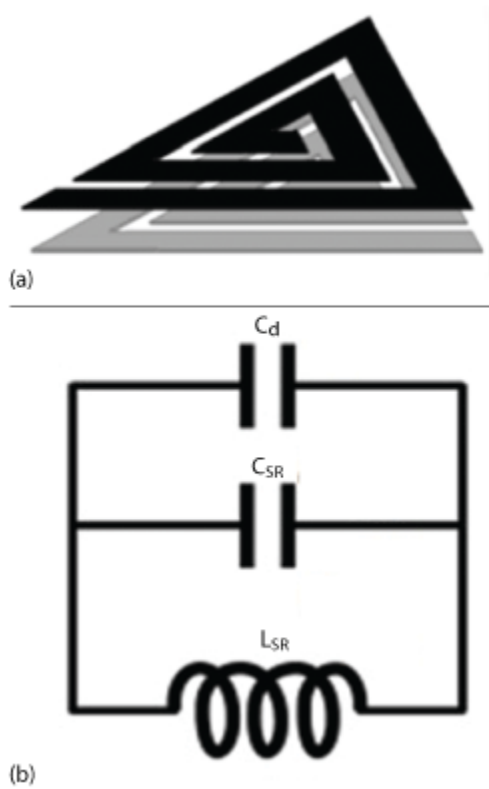


Figure 14 Layout of the BCTSR (a) and equivalent lumped circuit (b).

From (43)-(45), S_{21} is equal to S_{12} , but S_{11} is not equal to S_{22} . There are three independent equations for the three unknowns (n , μ_{eff} and ξ_0). By solving analytically (43)-(45), the expression for refractive index n is given by

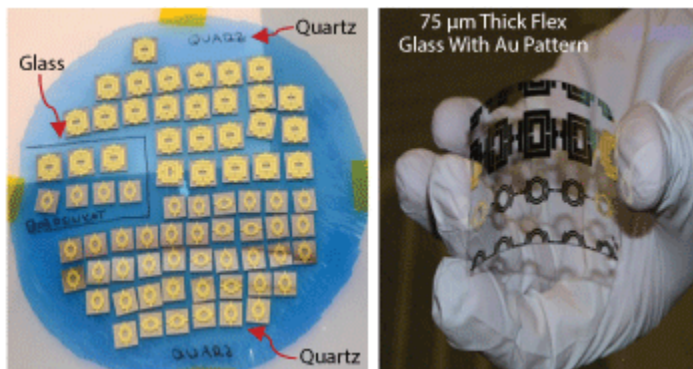


Figure 15 Metamaterial resonators fabricated on glass and quartz.

Ulrich L. Rohde, Federal Armed Forces University, Munich, Germany ; Ajay K. Poddar, Synergy Microwave, NJ

$$\cos(nk_0d) = \cos(ad) = \frac{1-(S_{11}S_{22})+S_{21}^2}{2S_{21}} \quad (46a)$$

From (36), using the condition of determinant (T)=1, and substituting (38)-(41):

$$\cos(nk_0d) = \cos(ad) = \frac{1-(S_{11}S_{22})+S_{21}^2}{2S_{21}} \quad (46b)$$

It is understood that when S_{11} is equal to S_{22} , (46) will degenerate into a standard retrieval form.² The refractive index n can be obtained from the implicit expression (46), which has many solutions for n to the different branches of the inverse cosine. When solving for n from (46), one must determine one branch from many branches of solutions. For a passive medium, the n must obey the condition $n''=\text{Im}(n)\geq 0$. After computing n , the other constitutive parameters are

$$\xi_0 = \left(\frac{n}{-2 \sin(nk_0l)} \right) \left(\frac{S_{11}-S_{22}}{S_{21}} \right) \quad (47)$$

$$\mu_y = \quad (48)$$

$$\left(\frac{in}{\sin(nk_0l)} \right) \left(\frac{2+S_{11}+S_{22}}{2S_{21}} - \cos(nk_0l) \right)$$

$$\epsilon_z = \left(\frac{n^2+\xi_0^2}{\mu_y} \right) \quad (49)$$

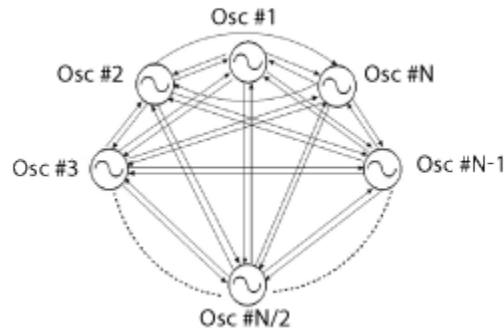


Figure 16 A typical N-coupled N-push oscillator topology.²⁹

Consequently, impedances z_+ and z_- can be obtained from (29)-(30). For a passive medium, the following conditions should be satisfied: $z_+'=\text{Re}(z_+)\geq 0$, $z_-'=\text{Re}(z_-)\geq 0$.

From (47)-(49), retrieved effective constitutive parameters can be assigned to the NIM structure; however, a variety of artifacts exists in the retrieved material parameters that are related to the NIM structure's inherent inhomogeneity. The artifacts in the retrieved material parameters are particularly severe for NIM structures that make use of resonant elements, as large fluctuations in the index and impedance can occur, such that the wavelength within the material can be on the order of or smaller than the unit cell dimension. The retrieval technique based on analyzing the S-parameter of a finite slab can suffer from unphysical anti-resonances with negative imaginary parts for some of the parameters. These anomalies could be due to periodicity of the structure and spatial dispersion.^{11,12}

Ulrich L. Rohde, Federal Armed Forces University, Munich, Germany ; Ajay K. Poddar, Synergy Microwave, NJ

An example of this behavior can be seen in the retrieved imaginary parts of ϵ and μ , which typically differ in sign for a unit cell that has a magnetic or an electric resonance. In homogeneous passive media, the imaginary components of the material parameters are restricted to positive values. This anomalous behavior vanishes as the unit cell size approaches zero.² For a homogeneous or symmetric material, the value of z will be unique, while it will result in two different values for an inhomogeneous or asymmetric material. The impedance $z = \frac{\mathbf{E}}{\mathbf{H}}$ is an intrinsic parameter which relates the electric field to the magnetic field.

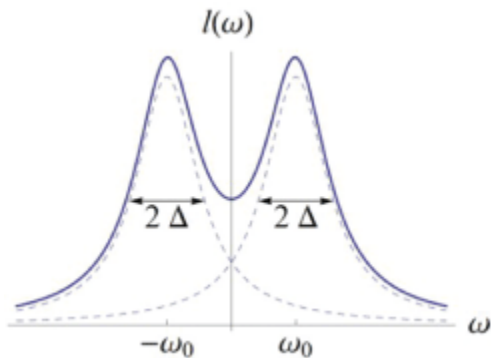


Figure 17 Bimodal distribution consisting of the sum of two Lorentzians.¹⁷

From (35), two equivalent expressions for the impedance of a slab can be obtained by

$$z = \frac{T_{12}}{e^{i\alpha d} - T_{11}} = \frac{e^{i\alpha d} - T_{22}}{T_{21}} \quad (50)$$

from (37) and (50)

$$Z^{\pm} = \pm \frac{(T_{11} - T_{22}) \pm \sqrt{(T_{22} - T_{11})^2 + 4T_{12}T_{21}}}{2T_{21}} \quad (51)$$

The two roots of (51) correspond to the two propagation directions of a plane wave. Substitution of (38)-(41) into (50) leads to

$$Z^{\pm} = \pm \frac{(S_{11} - S_{22}) \pm \sqrt{(1 - S_{11}S_{22} + S_{12}S_{21})^2 - 4S_{12}S_{21}}}{(1 - S_{11})(1 - S_{22}) - S_{12}S_{21}} \quad (52)$$

Ulrich L. Rohde, Federal Armed Forces University,
Munich, Germany ; Ajay K. Poddar, Synergy
Microwave, NJ

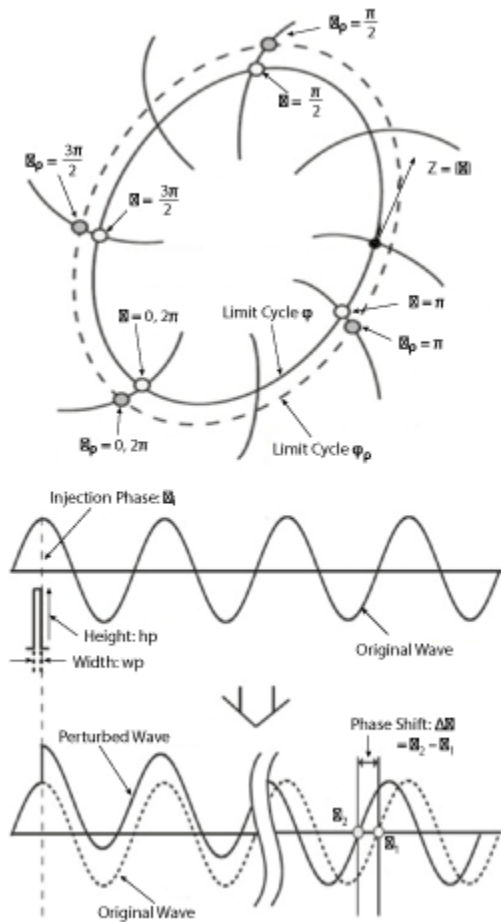


Figure 18 Typical phase injection mechanism in a Möbius strip resonator due to perturbation at the i^{th} node.

From (51) and (52), the characteristic impedance in terms of S-parameters associated with a metamaterial having bi-anisotropic structures is obtained. For a passive medium the impedance needs to satisfy the conditions $(z^+) \geq 0$ and $(-z^-) \geq 0$, where $(\cdot)'$ denotes the real part operator.

For an example, a typical array of SRRs printed on substrate and unit cell is shown in **Figure 10**. As illustrated in **Figure 10a**, a plane wave is incident in the x direction and polarized in the z direction. The dimensions are $\alpha = 3$ mm, $r = 0.74$ mm, $c = 0.2$ mm, $s = 0.1$ mm, $g = 0.2$ mm, $t = 0.3$ mm, $h = 35$ mm; and the substrate permittivity is ϵ_0 , for simplification.¹³

It can be seen from **Figures 10b** and **10c** that S_{12} is equal to S_{21} and the magnitudes of S_{11} and S_{22} are almost the same, while the phase of S_{11} is different with that of S_{22} . In this case, the application of the standard retrieval method¹ will lead to an inaccurate result. The discrepancy in phase of S-parameter measurements is because of the fact that the NIM's cells are not infinitely small compared to the incoming wavelength, causing spacial dispersion.

Assuming that there is a plane wave propagating in the direction of +x, polarized in the +z direction. The constitutive relationship between electric field and magnetic field can be described as

Ulrich L. Rohde, Federal Armed Forces University, Munich, Germany ; Ajay K. Poddar, Synergy Microwave, NJ

$$\overline{D}_z = \epsilon_0 \epsilon_z \overline{E}_z - ic^{-1} \xi_0 \overline{H}_y \quad (53)$$

$$\overline{B}_y = \mu_0 \mu_y \overline{H}_y + ic^{-1} \xi_0 \overline{E}_z \quad (54)$$

With the substitution of (53)-(54) into Maxwell's equations (18)-(19):

$$\nabla^2 \overline{E}_z + \omega^2 \epsilon_0 \mu_0 (\epsilon_z \mu_y - \xi_0^2) \overline{E}_z = 0 \quad (55)$$

From (13), the index (n) can be given by

$$n^2 = \epsilon_z \mu_y - \xi_0^2 \quad (56)$$

For a passive material, the roots have to be chosen properly to guarantee the condition $\text{Im}(n) \geq 0$. Otherwise, the exponentially growing solutions will occur, which violates energy conservation. The impedances of a bi-anisotropic material for wave propagation in the right-hand or left-hand directions are Z_{\pm} , the values of which are given by the equations

$$Z^+ = \frac{E^+}{H^+} \text{ and } Z^- = \frac{E^-}{H^-}$$

From Maxwell's equations (18)-(21), the formulas of the impedance and effective parameters can be obtained,

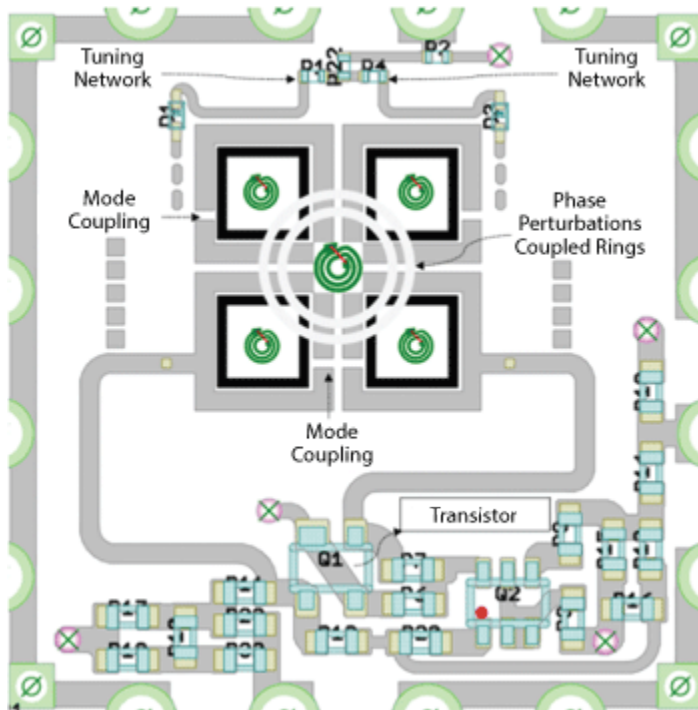


Figure 19 Typical layout of 25 GHz oscillator using Möbius coupled resonator.

Ulrich L. Rohde, Federal Armed Forces University, Munich, Germany ; Ajay K. Poddar, Synergy Microwave, NJ

$$Z^{\pm} = \frac{Z^{\pm}}{Z_0} = \frac{\mu_y}{\pm n - i\xi_0}, Z_0 = \sqrt{\frac{\mu_0}{\epsilon_0}} \quad (57)$$

$$\epsilon_z = \frac{n + i\xi_0}{Z^+} \quad (58)$$

$$\mu_y = (n - i\xi_0)Z^+ \quad (59)$$

$$\xi_0 = in \frac{Z^- + Z^+}{Z^- - Z^+} \quad (60)$$

The refractive index and impedances for a bi-anisotropic medium can be obtained from (46) and (52). The expressions for the effective electromagnetic parameters (ϵ_z , μ_y and ξ_0) and impedance associated with the bi-anisotropic structure are obtained from (58)-(60), and can be used for designing NIMS resonators for next generation energy efficient signal sources.

NIMs Inspired Resonator For Oscillators

A NIMs resonator can be classified into two types: resonant type and non-resonant type: examples are the split ring resonator (SRR), and left handed (LH) transmission line (T-line). Resonant type metamaterial exhibits larger dynamic range for material parameters ($\epsilon_r < 0$, $\mu_r < 0$), while non-resonant type metamaterial offers wide bandwidth and lower loss. Traditional metamaterial T-lines can be categorized into resonant type and non-resonant type, represented by the SRR/(complementary SRR) CSRR loaded T-line, and composite right/left handed (CRLH) T-line, with corresponding layouts shown in **Figures 11** and **12**, where C and L are per-unit length capacitance and inductance that determine the T-line metamaterial properties. For a T-line loaded with an SRR (see Figure 1), L_1 and C_2 are linked with T-line, whereas C_1 and L_2 are linked to magnetic coupling. Figure 11 shows the typical split ring resonator and NIM construction.

The physical properties in Figure 11 are given by:

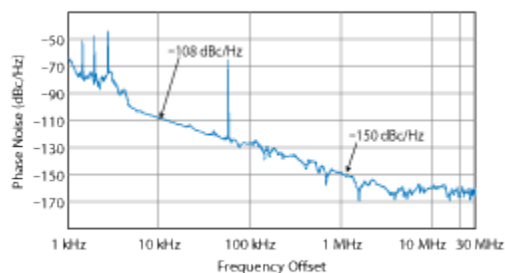


Figure 20 Measured phase noise of the 25 GHz oscillator shown in Fig. 19.

Ulrich L. Rohde, Federal Armed Forces University, Munich, Germany ; Ajay K. Poddar, Synergy Microwave, NJ

$$\varepsilon = \frac{Y}{j\omega} = C_2 \text{ is + ve} \rightarrow \varepsilon > 0 \text{ (+ve)} \quad (61)$$

$$\mu = \frac{Z}{j\omega} = \frac{L_1 + L_2 - \omega^2 L_1 L_2 C_1}{1 - \omega^2 L_2 C_1} \quad (62)$$

$$\mu < 0 \text{ (-ve) for } \left(\frac{1}{L_2 C_1} \right)^{1/2} \quad (63)$$

$$< \omega < \left(\frac{L_1 + L_2}{L_1 L_2 C_1} \right)^{1/2}$$

From (61) and (63), $\text{Re}(\mu)$ is negative and $\text{Re}(\varepsilon)$ is positive. For $(\varepsilon > 0, \mu < 0)$, propagating waves become evanescent waves, therefore energy cannot propagate through the resonator and is reflected back to establish a standing-wave.

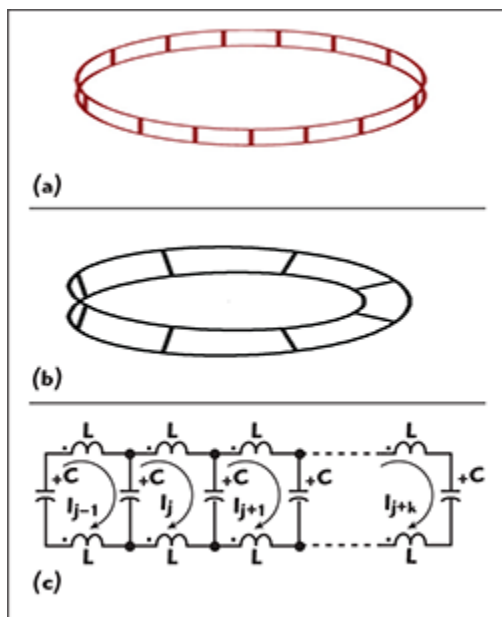


Figure 21 Ring resonator (a) Möbius strip (b) and equivalent LC representation consisting of L and C along the transmission line (c).

As a result, the SRR loaded T-line structure stores the energy and forms a high-Q resonator tank circuit for a low phase noise oscillator application. Similarly, for a T-line loaded with a CSRR (see Figure 12), L_1 is associated with the T-line, while C_1 , C_2 , and L_2 account from electric coupling of the CSRR to ground.

The physical properties in Figure 12 are given by

Ulrich L. Rohde, Federal Armed Forces University, Munich, Germany ; Ajay K. Poddar, Synergy Microwave, NJ

$$\mu = \frac{Y}{j\omega} = L_1 i s + v e \rightarrow \mu > 0 (+ve) \quad (64)$$

$$\epsilon = \frac{Y}{j\omega} = \frac{C_1(1-\omega^2 L_2 C_2)}{1-\omega^2(C_1+C_2)L_2} \quad (65)$$

$$\epsilon < 0 (-ve) \text{ for } \left(\frac{1}{(C_1 + C_2)L_2} \right)^{1/2}$$

$$< \omega < \left(\frac{1}{L_2 C_2} \right)^{1/2} \quad (66)$$

From (64) and (66), $\text{Re}(\mu)$ is positive and $\text{Re}(\epsilon)$ is negative. In this case ($\epsilon < 0, \mu > 0$), and electric plasma is formed, where propagating waves become evanescent waves, hence, energy cannot propagate through the resonator either and is reflected back to establish a standing-wave. As a result, the CSRR loaded T-line can also be used to form a high-Q resonator.

Figure 13a shows the structure of the broadside-coupled split ring resonator, there are two relative slips S_x and S_y between the two broadside coupled rings. **Figure 13b** shows the corresponding equivalent circuit, where L and R are the equivalent inductance and resistance, respectively, C_0 is mutual capacitance between the two rings and C_s is the capacitance of the split. As shown in Figure 13a, the tuning can be realized with minor slips along and perpendicular to the gap direction of two broadsides coupled rings.²² **Figure 14a** shows the layout of the broad coupled split ring (dark region denotes etching on the signal plane, and light region denotes broadside coupled triangular SR etched on ground plane), and **Figure 14b** shows the equivalent lumped circuit.

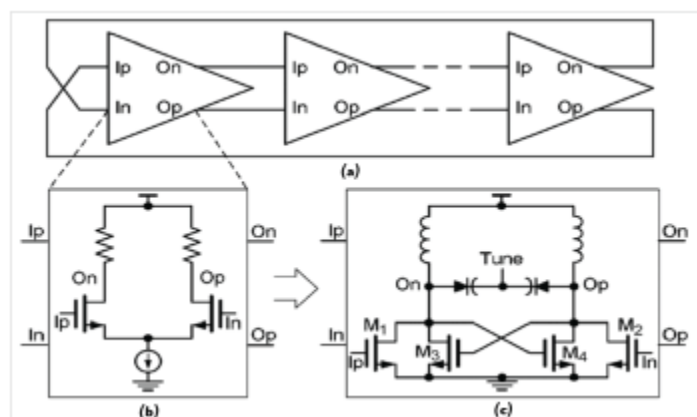


Figure 22 Ring oscillator structure (a) active gain stage (b) and LC-boosted gain stages (c).³²

For the validation of reported research work, resonators are fabricated on low loss quartz and borosilicate material. As shown in **Figure 15**, the metal structures are processed on top of quartz wafers (diameter $D = 150$ mm). The fabrication process uses a double-side coating of the substrates with a sputtered metal gold (Au) metallization. Unlike the SRR/CSRR depicted in Figure 15, the geometry of negative index Möbius strips (NIMS) is conformal, continuous, and maps one-to-one onto itself. These unique properties of NIMS permit EM coupling in such a way that a signal coupled to the loop does not encounter any obstructions when travelling around it, emulating an infinite

Ulrich L. Rohde, Federal Armed Forces University, Munich, Germany ; Ajay K. Poddar, Synergy Microwave, NJ

transmission line; hence providing a large group delay and high Q-factor. In this paper, the oscillator circuit uses a negative index ($\epsilon_r < 0, \mu_r < 0$) NIMO (Negative Index Möbius Oscillator) circuit for low cost high performance solution.

Examples

Signal Source

Möbius metamaterial inspired (MMI) structures are artificially constructed media on a size scale smaller than a wavelength of the external stimuli. They can exhibit a strong localization and enhancement of fields, which may provide novel tools to significantly enhance the sensitivity and resolution of sensors, and open new degrees of freedom in sensing design.¹⁻¹⁰ A detailed discussion about MMI structure characteristics is given in part 1 (MWJ May 2016 Issue), this issue (part 2) presents mainly their applications in high frequency signal sources and sensors, as well as the challenges and prospects.²⁸

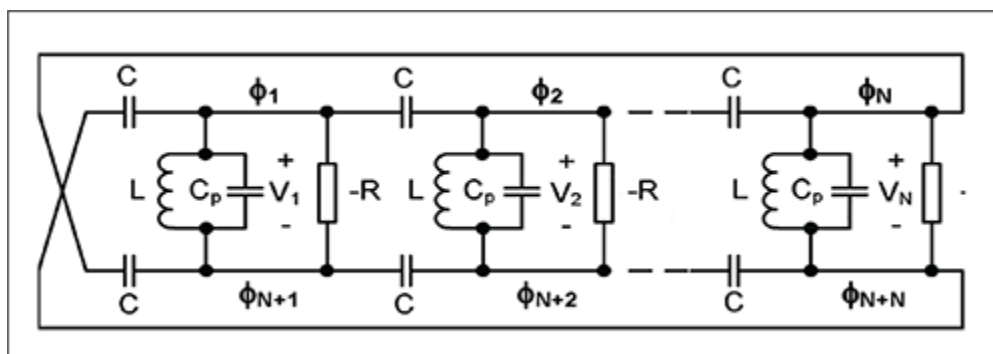


Figure 23 Typical negative index Möbius connected LC-ring oscillator.³³

From part 1 (MWJ May 2016 Issue, Equations 2 to 6, Ref 28), the Möbius transformation can be used for reducing the complexity of a system of N-coupled oscillators.²⁸ **Figure 16** shows the typical N-coupled N-push oscillator topology for the purpose of analysis.²⁹

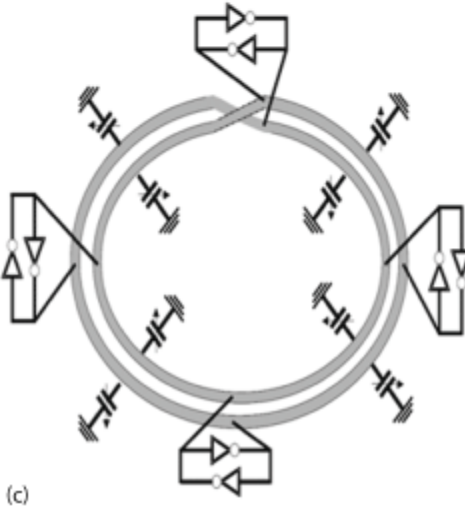
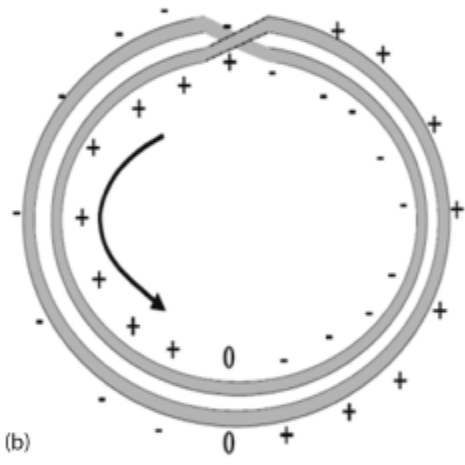
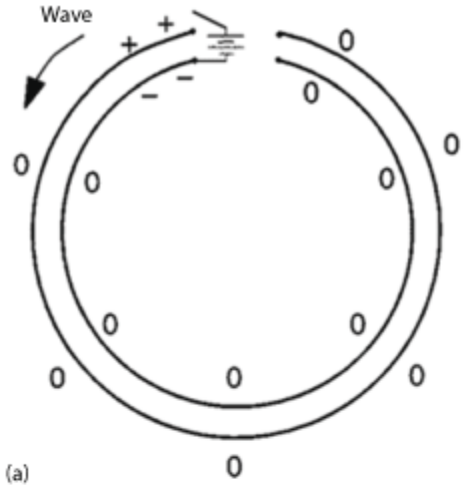
Globally, coupled oscillators have been used to model many diverse systems in physics, biology, chemistry, engineering, and space science. The system of coupled oscillators exhibits complex behavior because each individual unit influences the characteristics of other units. The phase dynamics of the N-coupled oscillator shown in Figure 16 is described by²⁹

$$\frac{\partial \theta_i(t)}{\partial t} = \omega_i - \left[\frac{\omega_i}{2Q_i} \right] \quad (67)$$

$$\left[\sum_{j=1}^N \beta_{ij} \left(\frac{A_j(t)}{A_i(t)} \right) \sin[\theta_j(t) - \theta_i(t) + \varphi_{ij}] \right]$$

$$\left[\frac{\omega_i}{2Q_i} B_{ni}(t) \right] \quad i=1, 2, 3, \dots, N$$

Ulrich L. Rohde, Federal Armed Forces University,
Munich, Germany ; Ajay K. Poddar, Synergy
Microwave, NJ



Ulrich L. Rohde, Federal Armed Forces University, Munich, Germany ; Ajay K. Poddar, Synergy Microwave, NJ

Figure 24 Oscillation based on the Möbius effect: open loop differential ring (a) Möbius connected differential ring (b) and practical tunable Möbius connected differential oscillator circuit (c).³⁷

where $A_i(t)$, $\theta_i(t)$, ω_i , and Q_i are the amplitude, phase, free-running frequency, and Q factor of the i^{th} oscillator, B_{ni} corresponds to the phase fluctuations; and β_{ij} and φ_{ij} are the coupling parameters between i^{th} and j^{th} oscillators.

From (67),

$$\frac{\partial \theta_i}{\partial t} = \dot{\theta}_i = f e^{j\theta_i} + l + \bar{f} e^{-j\theta_i} \quad (\text{for } i = 1, 2, 3 \dots N) \quad (68)$$

where f is any smooth complex-valued 2π -periodic function of the phases $\theta_1, \dots, \theta_N$ and over bar ($\bar{\cdot}$) is the complex conjugate.

The coupled-oscillator system shown in Figure 16 tends to collective synchronization and lock to a common frequency, despite the difference in oscillator natural frequencies. However, an accurate solution of (67) and (68) becomes difficult due to the nonlinearity and large number of variables associated with coupled-oscillator systems.

An alternative means to solve this is by reducing the complex dynamics to phase models assuming the couplings among oscillators are sufficiently weak such that when they are uncoupled, their phases advance at constant ‘velocities’ (natural frequency). The functions f and l given in (68) may depend on time and on any auxiliary state variables in the system, assuming such system is sinusoidally coupled because the dependence on i occurs solely through the first harmonics $e^{j\theta_i}$ and $e^{-j\theta_i}$.³⁰ This particular class of dynamical systems (68) can be reducible by a Möbius transformation in the form.³¹

$$e^{j\theta_i(t)} = M_t[e^{j\phi_i(t)}] \quad (69)$$

for $i = 1, 2, 3 \dots N$, where M_t is a one-parameter family of Möbius transformation and ϕ_i is a constant (time-independent) angle. The time- t flow map is an orientation-preserving homeomorphism that exhibits a Möbius map.

From (67) and (68), the distribution of natural frequencies for $N \rightarrow \infty$ is given by the sum of two Lorentzian distributions $l(\omega)$ [31]:

$$l(\omega) = \frac{\Delta}{2\pi} \left(\frac{1}{(\omega - \omega_0)^2 + \Delta^2} + \frac{1}{(\omega + \omega_0)^2 + \Delta^2} \right) \quad (70)$$

where Δ is the width parameter (half-width at half-maximum) of each Lorentzian and $\pm\omega_0$ are their center frequencies, as depicted in **Figure 17**.

From (70), the challenges are the minimization of frequency detuning (proportional to the separation between the two center frequencies) and AM-PM conversion noise. For low noise oscillator

Ulrich L. Rohde, Federal Armed Forces University, Munich, Germany ; Ajay K. Poddar, Synergy Microwave, NJ

applications, resonator Q-factor is important parameter. Resonator networks formed with Möbius strips are conformal, continuous, and map one-to-one onto itself; therefore, signals coupled to strips do not encounter any obstructions while travelling around them in such a way that a loop made of strips acts like an infinite transmission line. This arrangement enables a large group delay and improved Q-factor, which is promising for filter and oscillator applications. Möbius strips can have more than 1-twist (Figure 13, MWJ May 2016 Issue part 1, Ref 28). The 3-twisted Möbius strip has a trefoil knot as the boundary curve and so on. It is interesting to analyze the geometric phase of multi-knot non-orientable (Möbius) surfaces and their connection with nonlinear dynamical systems. This may provide a diagnostic analysis in abnormal neural oscillations and synchrony in schizophrenia.

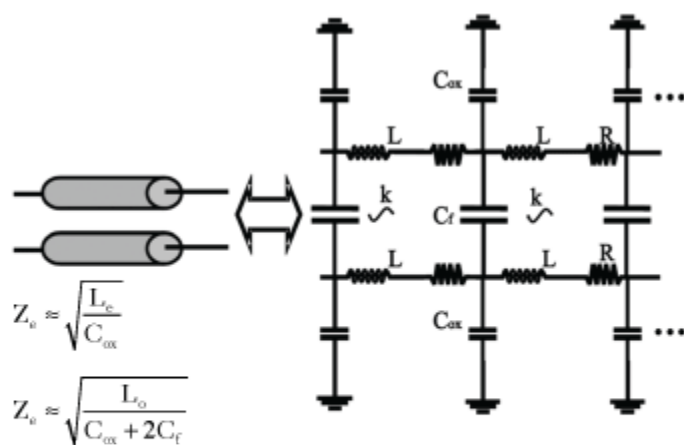
Figure 18 illustrates a typical phase-injection mechanism using phase-perturbation at the *i*th node on a Möbius strips resonator based frequency generating electronic circuit. The Q-factor (Q_L) of the resonator is²⁹

$$Q_L = \frac{\omega_0}{2} \left| \frac{d\varphi(\omega)}{d\omega} \right|_{\omega=\omega_0} = \quad (71)$$

$$\frac{\omega_0}{2} \tau_d; \quad \tau_d = \left| \frac{d\varphi(\omega)}{d\omega} \right|_{\omega=\omega_0}$$

$$\tau_d = \frac{d\varphi(\omega)}{d\omega} \Big|_{\omega=\omega_0} = \quad (72)$$

$$\frac{\varphi(\omega_0 + \Delta\omega) - \varphi(\omega_0 - \Delta\omega)}{2\Delta\omega}$$



$$L_e = L(1+k), L_o = L(1-k)$$

$$\gamma_e \approx \pm j\omega \sqrt{L_e C_{ox}}$$

$$\gamma_o \approx \pm j\omega \sqrt{L_o (C_{ox} + 2C_f)}$$

Ulrich L. Rohde, Federal Armed Forces University, Munich, Germany ; Ajay K. Poddar, Synergy Microwave, NJ

Figure 25 Lumped representation of coupled stripline model (Z_e, Z_o are even and odd mode impedances; γ_e, γ_o are even and odd mode propagation constants; L_e, L_o are even and odd mode lengths).³⁶

where $\varphi(\omega)$ is the phase of the resonator impedance and τ_d is the group delay. The effective inductance of the Möbius strips varies with the current/voltage passing through them, building the evanescent field for a higher quality factor:

$$\overline{Q_m(\omega)}_{\omega \rightarrow \omega_0} = \left[\frac{\omega}{2(I_{max} - I_{min})} \int_{I_{min}}^{I_{max}} Q_m(\omega, i) di \right]_{\omega \rightarrow \omega_0} \quad (73)$$

where I_{min} and I_{max} are the minimum and maximum currents, and $Q_m(\omega, i)$ is the instantaneous quality factor at frequency ω and current i flowing through the Möbius strips resonator.

From Figure 18, the locking condition is given by

$$\frac{2(f - f_0)}{f} = \frac{\eta \sin(\phi)}{2 + \cos(\phi)} \quad (74)$$

From (74), the locking range is restricted by the phase shift³⁰

$$\Delta f = \frac{f_0}{2Q} \tan \left(\sin^{-1} \left(\frac{\eta}{2} \right) \right) \quad (75)$$

where f_0 , Q , and η are the resonant frequency, quality factor of the LC tank, and the injection ratio (i_{inj}/I_{DC}) respectively.

Using Equations (71)-(75), a 25 GHz multi-knots Möbius-strips resonator based oscillator is designed and validated. **Figure 19** shows the circuit layout of tunable oscillator using multi-knots Möbius-strips resonators that support multi-injection nodes, thereby minimize detuning and provide a mechanism to suppress noise. The influence of phase-injection (perturbations) at different nodal points on the Möbius strips resonator are discussed for improving the tuning-range and phase noise performance of frequency generating circuits. The PCB is fabricated on an 8-mil thick Rogers substrate with a dielectric constant of 2.2.

As shown in Figure 19, the Möbius strips resonator increases evanescent mode field energy conservation due to the invariance of solutions for strips under a 2π rotation with a definite handedness. The resonator coupling coefficient β_j depends upon the geometry of the perturbation:

Ulrich L. Rohde, Federal Armed Forces University, Munich, Germany ; Ajay K. Poddar, Synergy Microwave, NJ

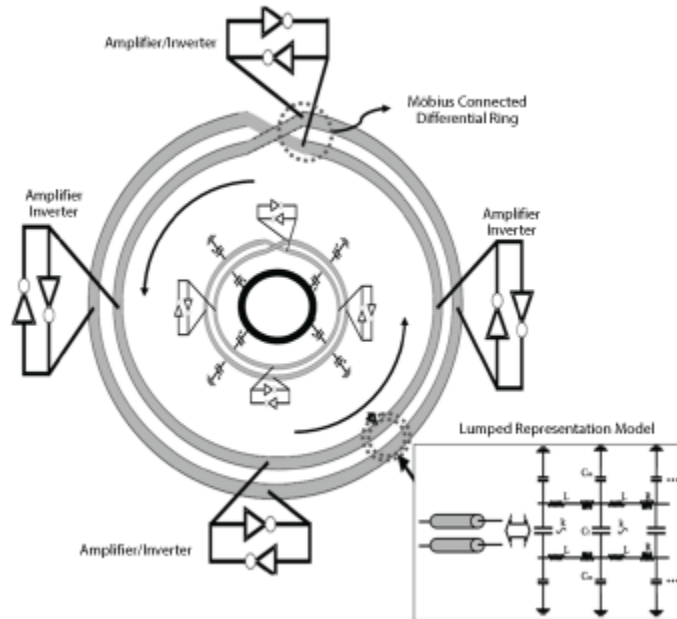


Figure 26 Möbius connected rotary wave oscillator, with distributed coupled lines represented as the continuous limit of the multi-section lumped LC circuit.

$$\beta_j = \left[\left(\frac{\int \epsilon E_a \cdot E_b dv}{\sqrt{\int \epsilon E_a^2 dv \int \epsilon E_b^2 dv}} \right)_e + \left(\frac{\int \mu H_a \cdot H_b dv}{\sqrt{\int \mu H_a^2 dv \int \mu H_b^2 dv}} \right)_m \right] \quad (76)$$

where E_a and H_a are the electric and magnetic field produced by the Möbius strip, and E_b and H_b are the corresponding fields due to perturbation of nearby adjacent resonators. The subscripts 'e' and 'm' denote electrical and magnetic coupling.

The oscillator circuit works with a DC bias of 5 Volts and 68 mA. Measured output power is typically -6 dBm. **Figure 20** shows measured phase noise of -109 dBc/Hz at 10 kHz offset with an output power of 6.73 dBm and 500 kHz tuning. The major drawback of this topology is limited tuning and mode-jumping.

For practical applications, output power, frequency stability, and tuning range need to be improved. These problems can be partially or fully fixed by understanding the phasor relationship between ring and Möbius strip resonator. **Figure 21** shows the typical representation of ring and Möbius strips resonators, and the equivalent LC representation consisting of inductors and capacitors along the transmission line. By virtue of the Möbius transformation, strips exhibit large group-delays, well suited for microwave resonator applications.

The electric currents on the ring resonator in **Figure 21c** can be formulated by a periodic boundary condition of the form described by

$$I_{j+k} = I_j \quad (77)$$

Ulrich L. Rohde, Federal Armed Forces University, Munich, Germany ; Ajay K. Poddar, Synergy Microwave, NJ

where I_k represents the electric current around the n^{th} closed loop on the periodic ladder structure of k -elements. The boundary condition of the general form shown in (77) governs that I_k is a conserved quantity that gives invariance to solutions under a 2π rotation with a definite handedness. The non-dissipative wave equation of the LC network for the k^{th} element is

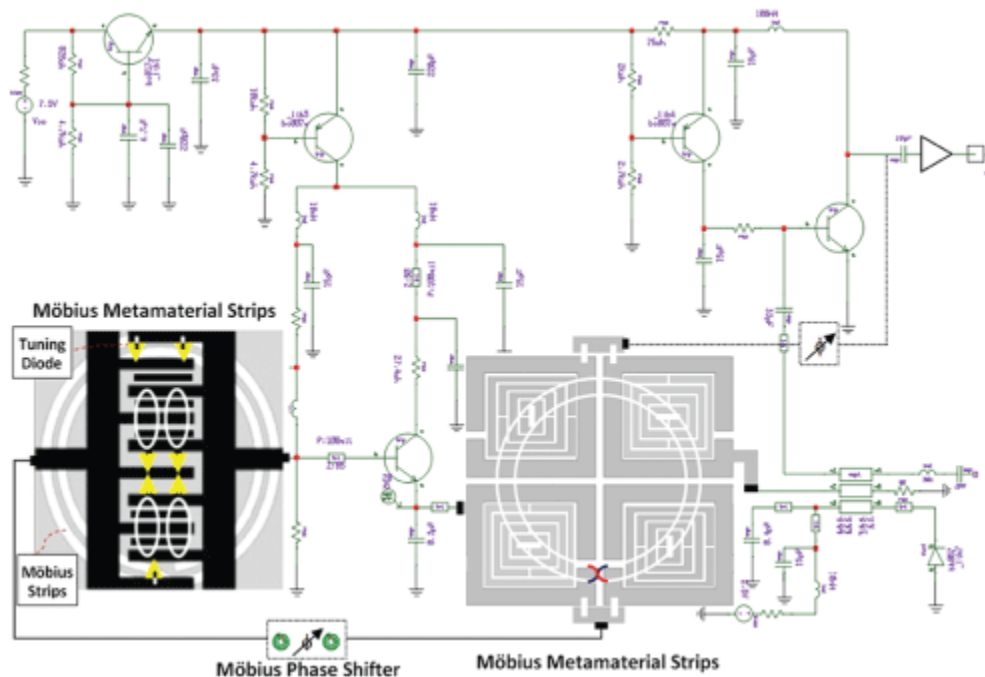


Figure 27 Layout of a 12 to 18 GHz oscillator using an evanescent mode metamaterial Möbius strip resonator network realized using 8 mil RT/Duroid 5880 with $\epsilon_r = 2.2$. The oscillator measures 0.75" x 0.75".

$$I_k = A_1 e^{i\left(\frac{p2\pi kM}{k}\right)} + A_2 e^{-i\left(\frac{p2\pi kM}{k}\right)} \quad (78)$$

$$\left(\omega^2 - \frac{1}{LC}\right)I_k - \left(\gamma\omega^2 - \frac{1}{2LC}\right)(I_{k+1} + I_{k-1}) = 0 \quad (79)$$

$$\omega^2 = \left\{ \frac{2\sin^2\left(\frac{p\pi}{k}\right)}{LC(1-2\gamma\cos\frac{p\pi}{k})} \right\} \quad (80)$$

where p is an integer specifying the normal mode and γ is the mutual coupling coefficient (mutual inductance 'M'=2 γ L). From (77)-(80), for even value of k , there are $k-1$ eigenvalues, including $(k-2)/2$ degenerate doublets and one singlet.

Ulrich L. Rohde, Federal Armed Forces University, Munich, Germany ; Ajay K. Poddar, Synergy Microwave, NJ

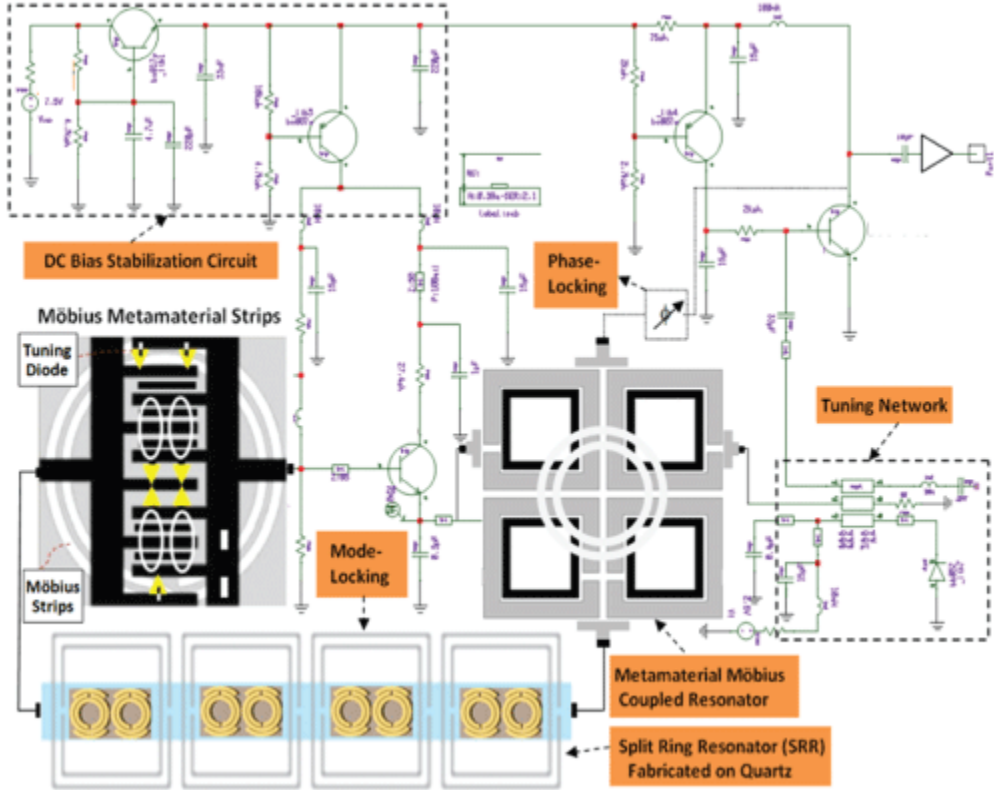


Figure 28 28.5 GHz NIMO oscillator.

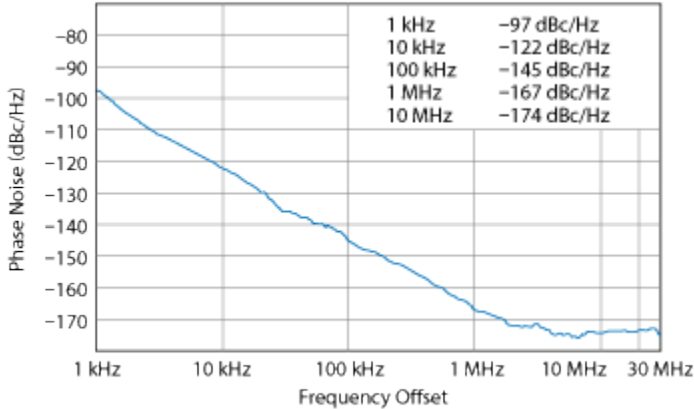


Figure 29 Measured phase noise of the 28.5 GHz NIMO oscillator shown in Fig. 28.

A typical ring resonator, whose eigenfunctions satisfy (17), defines a distinct inner and outer surface of the ring, shown in **Figure 21a**. Figure 21c shows a topological transformation resulting in a Möbius strip resonator, whose current dynamics formulated by applying twisted boundary condition as

Ulrich L. Rohde, Federal Armed Forces University, Munich, Germany ; Ajay K. Poddar, Synergy Microwave, NJ

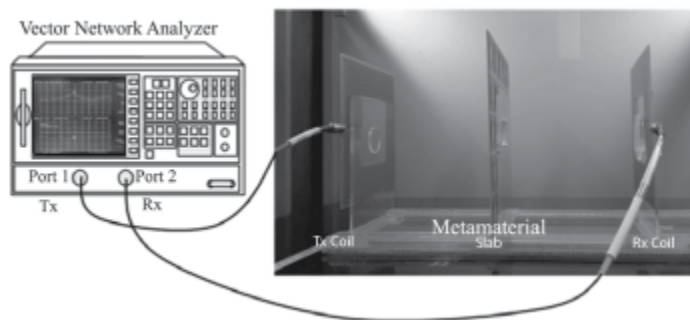
$$I_{j+k} = -I_j \quad (81)$$

From (81), a simple topological transformation on the resonator ring (see **Figure 21b**) results in a sign reversal of current (I_j) upon a 2π rotation of the solutions, and a 4π rotation is now required for invariance of the eigenfunctions. Note that the eigenfunctions satisfying the condition for twisted boundary are of the same form as (77) provided that the mode indices are given half-integral values ($p = 1/2, 3/2, 5/2, \dots, (k-1)/2$) relative to a ring consisting of identical components. The dispersion relation for the Möbius ring is the same as (80), however, the wave-vectors are shifted by

$$\Delta\lambda = -\left(\frac{\pi}{k}\right) \quad (82)$$

From (80)-(81), the two distinct topologies shown in Figures 21a and 21b can be considered a complementary pair related by a single transformation. The eigenfunctions of the Möbius resonator form an orthogonal basis set, presenting an interesting possibility for the design of metamaterials for multi-phase oscillator circuits. The inherent multi-phase, multi-mode nature of the Möbius strip provides additional degrees of freedom relative to traditional designs for generating multi-phase and quadrature oscillators. These are essential modules of many electronic systems, such as image rejection demodulators in wireless transceivers, half-rate clock-data-recovery (CDR) circuitry in high-speed optical receivers, phased-arrays, direct-conversion transmitters, and fractional-N frequency synthesizers.

TABLE I						
OSCILLATOR PERFORMANCE SUMMARY						
<i>Reference</i>	<i>f₀ (GHz)</i>	<i>P_{DC} (mW)</i>	<i>P_O (dBm)</i>	<i>Tuning (%)</i>	<i>L(f) (dBc/Hz)</i>	<i>FOM (dBc/Hz)</i>
[38]	22.1	11	-11	20.6%	-109	-181
[39]	11.2	20	2.9	4.1%	-125	-193
[40]	12.4	30	7.0	2.5%	-122	-189
[41]	38.1	130	10.5	2.6%	-112	-183
[42]	28.3	15	0.3	-	-98.5	-176
This Work (Fig. 28)	28.5	680	10.6	1.8%	-167	-227



Ulrich L. Rohde, Federal Armed Forces University, Munich, Germany ; Ajay K. Poddar, Synergy Microwave, NJ

Figure 30 Typical measurement setup for wireless power transfer efficiency.⁵³

Figures 22a and 22b show a typical ring oscillator. It exhibits multi-phase but it suffers from high phase noise.³¹ The LC-booster ring oscillator shown in Figures 22a and 22c minimizes the noise but is still inferior to a single-stage LC oscillator, largely due to the tradeoff between phase noise and phase error. Strong coupling between the gain stages (implying large-coupling MOSFETs) can minimize the phase errors; however, large coupling MOSFETs increase noise and power consumption.³¹ In all multiphase LC oscillator configurations, MOSFETs play a dual role; they compensate LC tank energy loss and they couple LC tanks together to maintain a desired phase relation.³² The second role, however, deteriorates phase noise, especially 1/f (flicker) noise up-conversion.³³

These problems can be partially, or fully, overcome by replacing the MOSFETs with metamaterial Möbius connected high order LC ring resonators in a distributed topology, as shown in Figure 23. The resonant frequency of metamaterial (-ve index) LC-ring resonators increases with the number of stages N as compared to right-handed (+ve index) LC-ring resonators. Therefore, the metamaterial LC-ring resonator is well suited for high frequency generation. The MOSFETs act as negative resistance generating devices, needed only for compensating the losses of the LC-ring resonators, implying that current from the MOSFETs is always injected into the resonator in phase with the voltage and does not resonate with LC resonator components. For an N -stage distributed LC-ring oscillator, the phase noise scales as $1/N$, while the power consumption increases linearly with N . This allows synthesizing multi-phases, while maintaining the identical figure of merit (FoM) as a 1-stage LC oscillator.³⁴

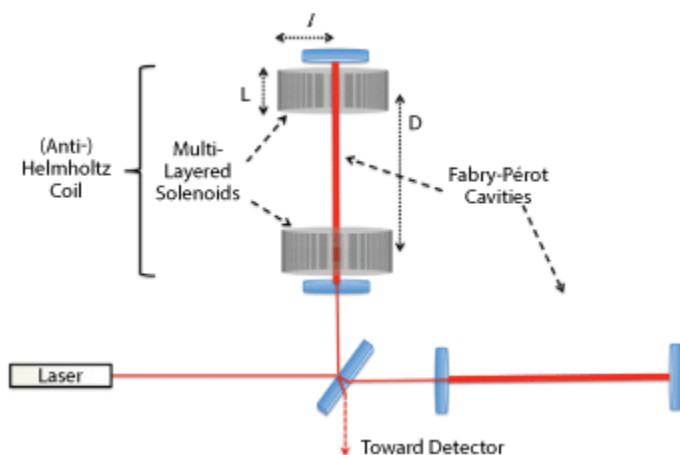


Figure 31 Typical experimental setup for measuring gravitational waves.⁵⁴

The main challenges of these topologies are mode selection and maintaining desired phase relationships. In addition, the number of noise sources increases linearly with N ; the total phase noise should be proportional to $1/N$, but this no longer holds under large signal drive level conditions. The alternative approach is a wave-based Möbius oscillator. The energy recycling nature of Möbius strips allows very high frequency oscillation with minimal power consumption for a given class of frequency generating circuits.

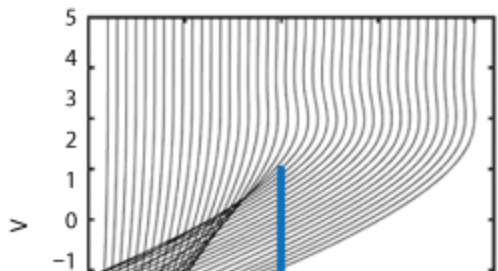
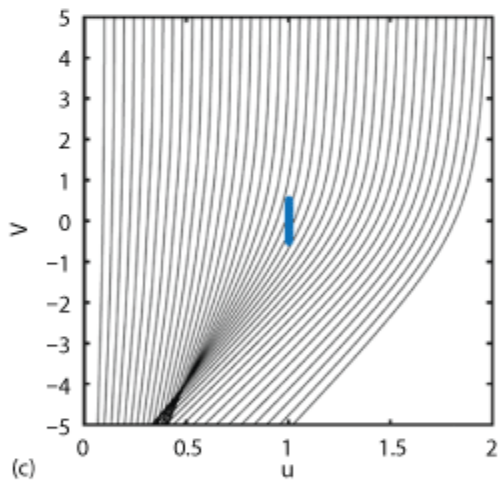
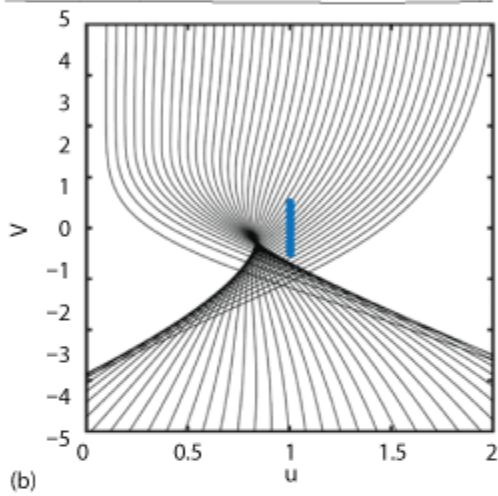
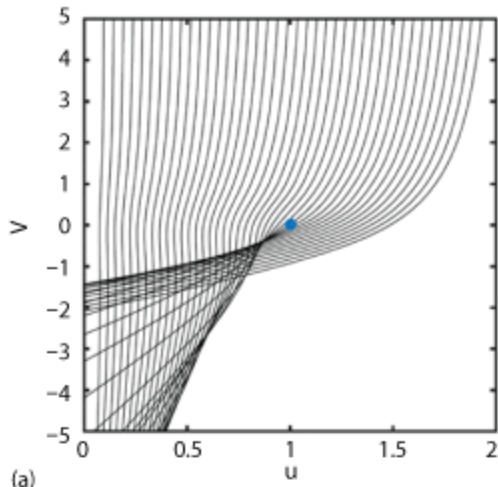
Ulrich L. Rohde, Federal Armed Forces University, Munich, Germany ; Ajay K. Poddar, Synergy Microwave, NJ

Figures 24a and **24b** show the differential open ring and closed cross-connected ring, respectively. When the voltage source connected in Figure 24a is replaced by a cross-connection of the inner and outer conductors, it leads to a signal inversion. If there were no losses, a wave could travel on this differential ring indefinitely, providing a full clock cycle for every other rotation of ring through the Möbius effect.³⁵ In real applications, however, multiple anti-parallel inverter pairs are added to the line shown in **Figure 24c** to overcome losses and provide rotation lock in the Möbius connected differential ring.

Figure 25 shows the lumped equivalent of coupled stripline used for the Möbius ring described in Figure 24.³⁶ As shown in Figure 25, coupled lines support even and odd mode propagation. The even mode (fast wave mode) is when the two lines are excited with the same signal; as a result, the coupling capacitance C_f between the two lines has no effect on the propagation constant γ . The odd mode (slow wave mode), is obtained as the line pair is excited differentially, so the coupling capacitance between the two lines has a doubling effect on the propagation constant of this mode. For the resonator application, slow wave propagation is of interest and care must be taken to suppress even mode propagation.

Figure 26 shows the method for achieving stable oscillation. Inverters across the lines provide gain and theoretically force the line to operate differentially; varactor diodes and the center ring provide even mode cancellation.³⁵⁻³⁷

Ulrich L. Rohde, Federal Armed Forces University,
Munich, Germany ; Ajay K. Poddar, Synergy
Microwave, NJ



Ulrich L. Rohde, Federal Armed Forces University, Munich, Germany ; Ajay K. Poddar, Synergy Microwave, NJ

Figure 32 Deflection of trajectories of parallel light rays coming from infinity. $CI = 10$ and $L \gg l$ (a) $CI = 10$ and $L = 0.5l$ (b) $CI = 10$ and $L = l$ (c) and $CI = 1$ and $L = 10l$ (d).⁵⁴

As shown in Figure 26, the Möbius effect enables energy harvesting (energy is not lost at each stage but re-circulates in closed path). While the benefits of Möbius connected wave-based oscillators are evident, this topology still has a limited tuning range of 10 to 20 percent. In this article, a novel approach for improving the tuning range is suggested and validated with the practical example of a 4 to 12 GHz/12 to 18 GHz oscillator based on a metamaterial Möbius strips resonator.

The phase-injections (perturbations) at different nodal points on the strips improve the tuning-range and phase noise performance of Möbius strip based frequency-generating circuits. The oscillator circuit shown in **Figure 27** works with a DC bias of 5 V and 35 mA; measured output power is typically 0dBm over the operating frequency band. The measured phase noise performance for a 12-18 GHz VCO is -130 dBc/Hz at 1 MHz frequency offset. It has a 6000 MHz tuning range with a phase noise variation within 3-5 dB over the operating frequency band.

The novel negative index Möbius oscillator (NIMO) circuit shown in **Figure 28** is built on an 8-mil thick substrate and uses a BFP740 SiGeHBT transistor for providing negative resistance to compensate the losses of the resonator tank. The total DC power consumption is 680 mW (8 V at 85mA), including the buffer amplifier.

Figure 28 shows the typical schematic of 28.5 GHz NIMO circuit that uses a NIMS resonator as a tank network for improving evanescent mode coupled energy of the resonator tank module and a coupled SRR for mode locking and unwanted mode suppression. **Figure 29** shows the measured phase noise of -144dBc/Hz at 100 kHz offset with 10.56 dBm output power. The measured FOM at 1MHz is -226 dBc/Hz for 680 mW DC power consumption. The main drawback of this configuration is limited tuning (<5 percent) to compensate for frequency drift due to temperature.

For practical applications, the tuning range must be improved. The tuning capability of the NIMO circuit in Figure 28 is enhanced by incorporating phase-stabilization (manipulating the phase velocity by introducing a mode-suppression ring that allows multi-mode-phase-injection into the Möbius strips cavity). This introduces a Q-multiplier effect and an exponential rise in the Q-factor over the desired tuning range. **Table I** shows several recently published papers to compare with this work based on FOM.

Wireless and Wearable Electronics

Wireless and wearable implantable biomedical electronics are promising for the continuous real-time measurement of underlying physiological signals such as in electrocardiography,⁴³ electromyography,⁴⁴ and brain action potentials.⁴⁵ In these biomedical devices, wireless power and data telemetry are employed to prolong operational life with communication based on backscattering, which can run either without a battery or with just a single rechargeable battery.

Magneto-inductive telemetry is widely used in these devices for wireless power and data transfer. The typical inductive telemetry core consists of a pair of antenna/coils placed coaxially in space, one inside the device and one placed externally as part of the reader/interrogator. The external coil

Ulrich L. Rohde, Federal Armed Forces University, Munich, Germany ; Ajay K. Poddar, Synergy Microwave, NJ

typically transmits data which is also harvested for its power and regulated to power up the implant circuitry. The antennas used for these telemetry systems are either loop wire coils or printed spiral coils. One of the most important design criteria is to maximize the coupling coefficient between external and implanted coils, which affects the power/data transfer efficiency significantly.

There has recently been an effort to use a metamaterial resonator for improved wireless energy transfer. Metamaterial resonators such as SRRs can exhibit strong magnetic resonance to EM waves,⁴⁶ with high Q factors. This makes them excellent candidates for near-field resonant power/data transfer. The SRR also enables sub-wavelength focusing of the incident energy at resonance in the capacitive gap of the metamaterial, which could be harvested for energy/power. Compared to a conventional antenna/coil system for power telemetry, the SRR provides a compact and low profile geometry due to an integrated antenna and resonator function built into the structure.⁴⁷

Coupled mode theory (CMT)⁴⁸ predicts that when the resonances of both coils are matched, within the "strongly coupled regime," it results in maximal energy transfer between the coils. However, if the resonance of either of the coils deviates from one another, the power transfer efficiency drops sharply. Since the biological environment is expected to vary due to physiological changes, it is very hard to match their resonances. This issue is especially critical for metamaterial-based energy harvesters⁴⁹⁻⁵⁰ due to their sharp narrowband resonances, thus automatic tuning of resonances is necessary. This can be done for conventional coils with tunable varactors;⁵¹⁻⁵² however, the tuning needs precision, adds complexity in the system and may be difficult with motion artifacts. The alternative is to embed of non-foster impedance circuitry inside the SRR metamaterial to achieve optimal power transfer over a broad band without the need for any tuning.

Current wireless power transfer (WPT) technology allows power transfer only over a limited distance because, as the distance between the transmitter (Tx) and receiver (Rx) coils increases, the power transfer efficiency (PTE) decreases with a steep slope, while the electromagnetic field (EMF) leakage increases. In order to increase PTE and decrease EMF leakage simultaneously, we need a method to concentrate the magnetic fields between the Tx and Rx coils. In this article, we proposed a novel metamaterial structure to realize high efficiency and low EMF leakage. Metamaterial can confine the magnetic fields between the Tx and Rx coils by negative relative permeability, including the reduction in leakage. **Figure 30** shows a typical experimental setup for optimized efficiency of wireless power transfer.⁵³

Artificial Gravitational Field

The generation of artificial gravitational fields with electric currents could in principle be detected through the induced change in space-time geometry that results in a purely classical deflexion of light by magnetic fields. Fuzfa 54 has proposed the experimental set-up shown in **Figure 31** that includes stacked large superconducting Helmholtz coils for the generation of the artificial gravitational field and the detection would be achieved by highly sensitive Michelson interferometers whose arms contain Fabry-Perot cavities to store light into the generated gravitational field. As depicted in Figure 31, the amplitude of the phase shift accumulated during the bouncing of light in the curved space-time generated by the magnetic field would reach, in a few months, the level of an astrophysical source of gravitational wave passing through ground-based GW observatories.⁵⁵ Since space-time is slightly shrunk inside the superconducting coils, light trapped inside the powered coil

Ulrich L. Rohde, Federal Armed Forces University, Munich, Germany ; Ajay K. Poddar, Synergy Microwave, NJ

accumulates phase shift as round trips succeed each other. The sensitivity and dynamic range of superconducting coils can be increased by incorporating MMI superconducting coils. The ongoing research in the MMI field could open new eras in experimental gravity and laboratory tests of space-time bends based on equivalence principle of general theory of relativity.

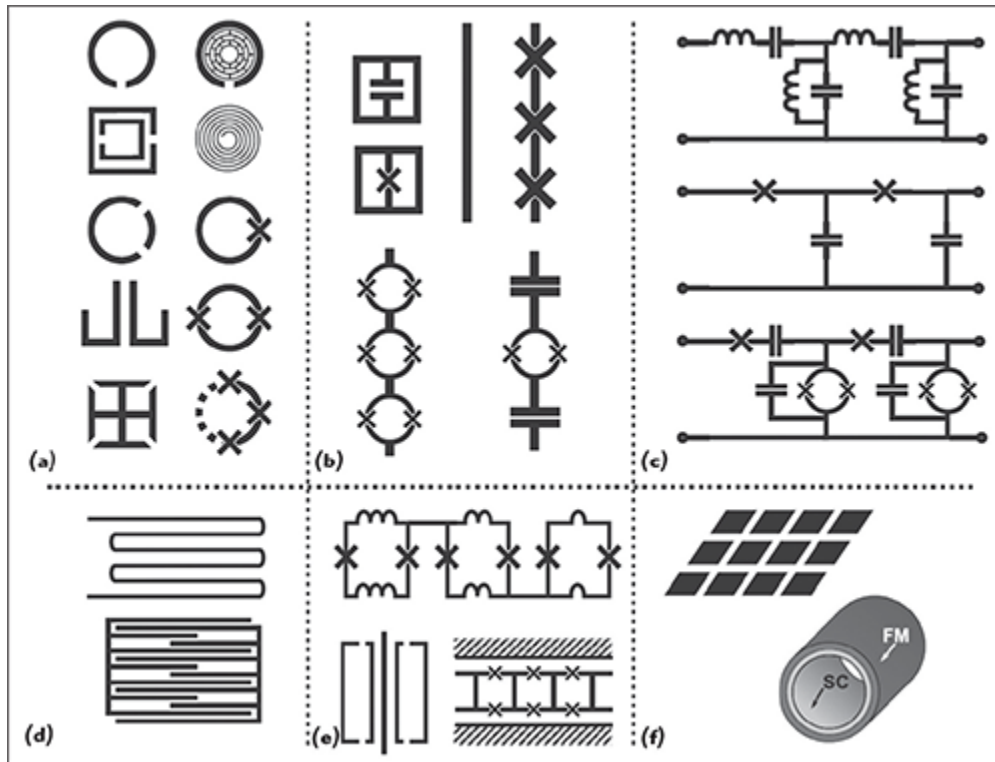


Figure 33 Typical symbolic representation of a superconducting metamaterial as a subset of meta-atoms and meta-molecules: magnetically active meta-atoms (a) electrically active meta-atoms (b) transmission line metamaterials (c) lumped element meta-atoms (d) various meta-molecule realizations (e) and DC magnetic cloak structures (f).⁵⁷

Ulrich L. Rohde, Federal Armed Forces University,
Munich, Germany ; Ajay K. Poddar, Synergy
Microwave, NJ

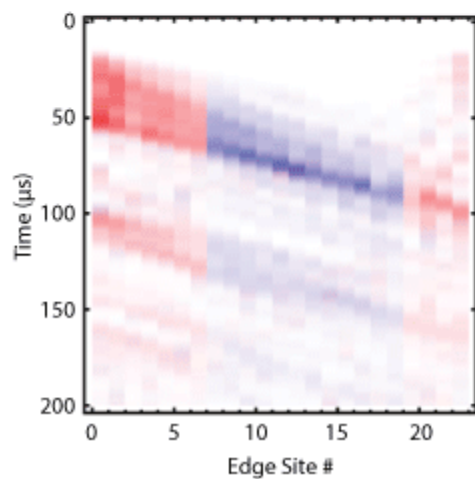
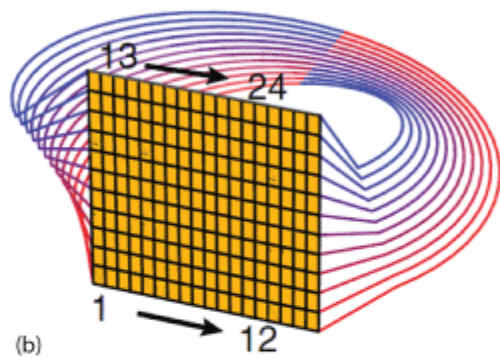
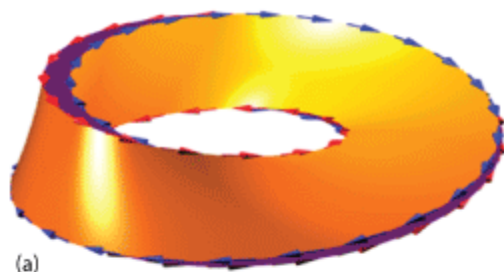


Figure 34 Typical topological Möbius metamaterial insulator: Möbius TI, with the arrow indicating the edge propagation direction, color the spin state (a) connectivity of the Möbius TI, with metamaterial PCB and external connections generating the topology indicating spin on traversing the edge (b) and spin-resolved detection of edge transport after excitation of \uparrow . \uparrow and \downarrow intensities are plotted in the red and blue channels, respectively, showing the conversion from \uparrow to \downarrow when the excitation moves from one edge to the other (c).

Figure 32 illustrates the deflected trajectories of a bundle of rays of incoming parallel light from spatial infinity, these trajectories have been obtained from the numerical resolution of geodesic equations in strongly curved space-times around a loop of solenoids with extremely large magneto-gravitational coupling (CI) so that the way light is deflected can be easily shown. Deflections of trajectories are plotted with different values of solenoid length (L), radius of current loop (I) and magneto-gravitational coupling (CI) strength.⁵⁴

Ulrich L. Rohde, Federal Armed Forces University, Munich, Germany ; Ajay K. Poddar, Synergy Microwave, NJ

MMI structures represent artificially engineered materials that can create and enable unique interactions of matter with electromagnetic and gravitational waves.

MMI Superconducting Coils

Superconductors offer unique advantages compared to ordinary metal, semiconductor and dielectric meta-atoms, namely: low loss, flux quantization and Josephson effects, quantum interactions between photons and discrete energy states in the meta-atom, and strong diamagnetism.⁵⁶

Figure 33 shows the typical symbolic representation of a superconducting metamaterial as a subset of meta-atoms and meta-molecules. Superconducting quantum metamaterial opens the possibility to explore collective quantum dynamics under very strong coupling between electromagnetic fields, gravitational field and artificial atoms.⁵⁷

Metamaterial, where interaction strengths and length scales can be engineered, are a promising avenue for studying topological structure such as Möbius strips. Time-reversal broken topological metamaterial have been realized in the microwave domain via a lattice of chiral magnetic (gyrotropic) resonators.⁵⁸⁻⁵⁹ **Figure 34** shows a typical Möbius metamaterial insulator, realized by connecting the left and right edges of the system with a half twist and a spin flip.⁶⁰

As illustrated in **Figure 34b**, “a” inductor j sites from the top of the left edge are connected to the “b” inductor at the j sites from the bottom of the right edge. The spin flip is necessary, as “up” spins propagate rightwards on the top edge but leftwards on the bottom edge.⁶¹ **Figure 34b** shows the temporal dynamics of a spin-up excitation in the system; it propagates rightward along the system edge, until it reaches the other edge, is converted into a down spin, and continues its progression around the system perimeter; this cycle is repeated until the excitation is damped out by the finite system Q .

Conclusion

Part 2 discusses MMS resonator based topology that enables next generation energy efficient signal source solutions in integrated circuit and surface mounted planar technology. The unique features of Möbius metamaterial strips promise many future inventions, recurring in an endless loop – one could say that the future exists on a Möbius strips surface. Part 3 will follow in the July 2016 issue.

References

1. D. R. Smith, S. Schultz, P. Markos and C. M. Soukoulis, “Determination of Effective Permittivity and Permeability of Metamaterials from Reflection and Transmission Coefficients,” *Physical Review B*, Vol. 65, No. 19, April 2002, pp. 195104-1-5.
2. D. R. Smith, D. C. Vier, T. Koschny, and C. M. Soukoulis, “Electromagnetic Parameter Retrieval from Inhomogeneous Metamaterials,” *Physical Review E*, Vol. 71, No. 3, March 2005, pp. 36617-1-11.
3. U. C. Hasar and J. J. Barroso, “Retrieval Approach for Determination of Forward and Backward Wave Impedances of Bianisotropic Metamaterials,” *Progress In Electromagnetics Research*, Vol. 112, 2011, pp. 109–124.

Ulrich L. Rohde, Federal Armed Forces University, Munich, Germany ; Ajay K. Poddar, Synergy Microwave, NJ

4. J. B. Pendry, A. J. Holden, D. J. Robbins and W. J. Stewart, "Low Frequency Plasmons in Thin-Wire Structures," *Journal of Physics: Condensed Matter*, Vol. 10, No. 22, June 1998, pp. 4785–4809.
5. R. Marqués, F. Medina and R. Rafii-El-Idrissi, "Role of Bianisotropic in Negative Permeability and Left-Handed Metamaterials," *Physical Review B*, Vol. 65, No. 14, April 2002, pp. 144440-1-6.
6. A. M. Nicolson and G. Ross, "Measurement of the Intrinsic Properties of Materials by Time-Domain Techniques," *IEEE Transactions on Instrumentation and Measurement*, Vol. 19, No. 4, November 1970, pp. 377–382.
7. W. B. Weir, "Automatic Measurement of Complex Dielectric Constant and Permeability at Microwave Frequencies," *Proceedings of the IEEE*, Vol. 62, No. 1, January 1974, pp. 33–36.
8. V. Milosevic, B. Jokanovic and R. Bojanic, "Effective Electromagnetic Parameters of Metamaterial Transmission Line Loaded With Asymmetric Unit Cells," *IEEE Transactions on Microwave Theory and Techniques*, Vol. 61, No. 8, August 2013, pp. 2761–2772.
9. L.D. Landau, L. P. Pitaevskii and E.M. Lifshitz, *Electrodynamics of Continuous Media*, 2nd ed. Oxford, U.K.: Pergamon, 1984.
10. J. W. Graham, "Arbitrary Oriented Biaxial Anisotropic Media: Wave Behaviors and Microstrip Antennas," Ph.D. Dissertation, Syracuse University, May 2012.
11. T. Koschny, P. Markoš, E. N. Economou, D. R. Smith, D. C. Vier, and C. M. Soukoulis, "Impact of Inherent Periodic Structure on Effective Medium Description of Left-Handed and Related Metamaterials," *Physical Review B: Condensed Matter*, Vol. 71, No. 24, June 2005, pp. 245105-1-22.
12. A. Alù, "Restoring the Physical Meaning of Metamaterial Constitutive Parameters," *Physical Review B, Condensed Matter*, Vol. 83, No. 8, February 2011, pp. 081102-1-4.
13. L. Chen, Z. -Y. Lei, R. Yang, X. -W. Shi and J. Zhang, "Determining the Effective Electromagnetic Parameters of Bianisotropic Metamaterials with Periodic Structures," *Progress In Electromagnetics Research M*, Vol. 29, 2013, pp. 79–93.
14. X. Chen, T. M. Grzegorzcyk, B. -I Wu, J. Pacheco, Jr. and J. A. Kong, "Robust Method to Retrieve the Constitutive Effective Parameters of Metamaterial," *Physical Review E*, Vol. 70, No. 1, July 2004, pp. 16608-1-7.
15. U. L. Rohde and A. K. Poddar, "Möbius Metamaterial Inspired Next Generation Circuits and Systems," *Microwave Journal*, Vol. 59, No. 5, May 2016.
16. X. Chen, B. -I. Wu, J. A. Kong and T. M. Grzegorzcyk, "Retrieval of the Effective Constitutive Parameters of Bianisotropic Metamaterial," *Physical Review E*, Vol. 71, No. 4, April 2005, pp. 046610.
17. R. Marqués, F. Martín, M. Sorolla, *Metamaterial with Negative Parameters: Theory, Design and Microwave Applications*, Wiley, 2008.
18. O. Sydoruk¹, E. Tatartschuk¹, E. Shamoninal and L. Solymar, "Analytical Formulation for the Resonant Frequency of Split Rings," *Journal of Applied Physics*, Vol. 105, No. 1, January 2009, pp. 14903.
19. X. Chen, T. M. Grzegorzcyk and J. A. Kong, "Optimization Approach to the Retrieval of the Constitutive Parameters of a Slab of General Bianisotropic Medium," *Progress In Electromagnetics Research*, Vol. 60, 2006, pp. 1–18.
20. Z. Li, K. Aydin and E. Ozbay, "Determination of the Effective Constitutive Parameters of Bianisotropic Metamaterials from Reflection and Transmission Coefficients," *Physical Review E*, Vol. 79, No. 2, February 2009, pp. 026610-1-7.

Ulrich L. Rohde, Federal Armed Forces University, Munich, Germany ; Ajay K. Poddar, Synergy Microwave, NJ

21. U. C. Hasar, "Procedure for Accurate and Stable Constitutive Parameters Extraction of Materials at Microwave Frequencies," *Progress In Electromagnetics Research*, Vol. 109, 2010, pp. 107–121.
22. J. Wang, S. Qu, J. Zhang, H. Ma, Y. Yang, C. Gu and X. Wu, "A Tunable Left-Handed Metamaterial Based on Modified Broadside-Coupling Split-Ring Resonators," *Progress In Electromagnetics Research Letters*, Vol. 6, 2009, pp. 35-45.
23. T. Nakamura, T. Masuda, N. Shiramizu, A. Nakamura and K. Washio, "A 11.1-V Regulator-Stabilized 21.4-GHz VCO and a 11.5% Frequency-Range Dynamic Divider for K-Band Wireless Communication," *MTT-Transactions*, Vol. 60, No. 9, September 2012, pp. 2823–2832.
24. Z. Chen, W. Hong, J. Chen and J. Zhou, "Design of High-Q Tunable SIW Resonator and its Application to Low Phase Noise VCO," *IEEE Microwave and Wireless Components Letters*, Vol. 23, No. 1, January 2013, pp. 43–45.
25. A. Collado, F. Mira and A. Georgiadis, "Mechanically Tunable Substrate Integrated Waveguide (SIW) Cavity Based Oscillator," *IEEE Microwave and Wireless Components Letters*, Vol. 23, No. 9, September 2013, pp. 489-491.
26. C. -L. Chang, C. -H. Tseng and H. -Y. Chang, "A New Monolithic Ka-Band Filter-Based Voltage Controlled Oscillator Using 0.15um GaAs PHEMT Technology," *IEEE Microwave and Wireless Components Letters*, Vol. 24, No. 2, February 2014, pp. 111–113.
27. Y. Chen, K. Mouthaan and F. Lin "Design of X-band and Ka-band Colpitts oscillators Using a Parasitic Cancellation Technique," *IEEE Transactions on Circuits and Systems-I*, Vol. 57, No. 8, August 2010, pp. 1817–1828.
28. Ulrich L. Rohde and Ajay K. Poddar, "Möbius Metamaterial Inspired Next Generation Circuits and Systems," *Microwave Journal*, Vol. 59, No. 5, May 2016.
29. A. Poddar, Slow Wave Resonator Based Tunable Multi-Band Multi-Mode Injection-Locked Oscillator, Habil Thesis, BTU Cottbus, Germany, 2014.
30. S. A. Marvel, R. E. Mirollo and S. H. Strogatz, "Identical Phase Oscillators with Global Sinusoidal Coupling Evolve by Möbius Group Action," *Chaos: An Interdisciplinary Journal of Nonlinear Science*, Vol. 19, No. 4, December 2009, pp. 043104-1-4.
31. E. Martens, "Cooperative Behavior in Networks of Coupled Oscillators," Ph.D. Diss., Faculty of the Grad School of Cornell University, May 2009.
32. A. Rofougaran, J. Rael, M. Rofougaran and A. Abidi, "A 900 MHz CMOS LC Oscillator with Quadrature Outputs," *IEEE International Solid State Circuits Conference Digest*, February 1996, pp. 392–393.
33. L. Guansheng, E. Afshari, "A Low Phase Noise Multi-Phase Oscillator Based on Left-Handed LC-Ring," *IEEE Journal of Solid State Circuits*, Vol. 45, No. 9, September 2010, pp. 1822–1833.
34. L. Romano, A. Bonfanti, S. Levantino, C. Samori and A. L. Lacaita, "5-GHz Oscillator Array with Reduced Flicker Up-Conversion in 0.13-um CMOS," *IEEE Journal of Solid State Circuits*, Vol. 41, No. 11, November 2006, pp. 2457–2467.
35. J. Wood, T. C. Edwards and Steve Lipa, "Rotary Travelling-Wave Oscillator Arrays: a New Clock Technology," *IEEE Journal of Solid State Circuits*, Vol. 36, No. 11, November 2001, pp. 1654–1665.
36. H.T. Ahn and D. J. Allstot, "A 0.5-8.5-GHz Fully Differential CMOS Distributed Amplifier," *IEEE Journal of Solid State Circuits*, Vol. 37, No. 8, August 2002, pp. 985–993.
37. D. Ham and W. Andress, "A Circular Standing Wave Oscillator," *IEEE Solid State Circuits Conference Digest*, Vol. 1, February 2004, pp. 380–533.

Ulrich L. Rohde, Federal Armed Forces University, Munich, Germany ; Ajay K. Poddar, Synergy Microwave, NJ

38. T. Nakamura, T. Masuda, N. Shiramizu, A. Nakamura and K. Washio, "A 1.1-V Regulator-Stabilized 21.4-GHz VCO and a 11.5% Frequency-Range Dynamic Divider for K-Band wireless communication", *IEEE Transactions on Microwave Theory and Techniques*, Vol. 60, No. 9, September 2012, pp. 2823-2832.
39. Z. Chen, W. Hong, J. Chen and J. Zhou, "Design of High-Q Tunable SIW Resonator and its Application to Low Phase Noise VCO," *IEEE Microwave and Wireless Components Letters*, Vol. 23, No. 1, January 2013, pp. 43-45.
40. A. Collado, F. Mira and A. Georgiadis, "Mechanically Tunable Substrate Integrated Waveguide (SIW) Cavity Based Oscillator," *IEEE Microwave and Wireless Components Letters*, Vol. 23, No. 9, September 2013, pp. 489-491.
41. C. -L. Chang, C. -H. Tseng and H. -Y Chang, "A New Monolithic Ka-Band Filter-Based Voltage Controlled Oscillator Using 0.15um GaAs PHEMT Technology," *IEEE Microwave and Wireless Components Letters*, Vol. 24, No. 2, February 2014, pp. 111-113.
42. Y. Chen, K. Mouthaan and F. Lin "Design of X-Band and Ka-Band Colpitts Oscillators Using a Parasitic Cancellation Technique," *IEEE Transactions on Circuits and Systems-I*, Vol. 57, No. 8, August 2010, pp. 1817-1828.
43. J. Riistama, E. Aittokallio, J. Verho and J. Lekkala, "Totally Passive Wireless Biopotential Measurement Sensor by Utilizing Inductively Coupled Resonance Circuits," *Sensors and Actuators A: Physical*, Vol. 157, No. 2, February 2010, pp. 313-321.
44. D. J. Young, "Wireless Powering and Data Telemetry for Biomedical Implants," International Conference of the *IEEE Engineering in Medicine and Biology Society*, September 2009, pp. 3221-3224.
45. W. Biederman, D. J. Yeager, N. Narevsky, A. C. Koralek, J. M. Carmena, E. Alon and J. M. Rabaey, "A Fully-Integrated, Miniaturized (0.125 mm²) 10.5 μ W Wireless Neural Sensor Solid-State Circuits," *IEEE Journal of Solid State Circuits*, Vol. 48, No. 4, April 2013, pp. 960-970.
46. V. G. Veselago, "The Electrodynamics of Substances with Simultaneously Negative Values of ϵ and μ ," *Sov Phys Uspekhi*, Vol. 10, No. 4, 1968, pp. 509-514.
47. R. A. Shelby, D. R. Smith and S. Schultz, "Experimental Verification of a Negative Index of Refraction," *Science*, Vol. 292, No. 5514, April 2001, pp. 77-79.
48. A. Kurs, A. Karalis, R. Moffatt, J. D. Joannopoulos, P. Fisher and M. Soljac'ic', "Wireless Power Transfer via Strongly Coupled Magnetic Resonances," *Science*, Vol. 317, No. 5834, July 2007, pp. 83-86.
49. A. M. Hawkes, A. R. Katko S. A. Cummer, "A Microwave Metamaterial with Integrated Power Harvesting Functionality," *Applied Physics Letters*, Vol. 103, No. 16, October 2013, p. 163901.
50. O. M. Ramahi, T. S. Almoneef, M. Alshareef and M. S. Boybay, "Metamaterial Particles for Electromagnetic Energy Harvesting," *Applied Physics Letters*, Vol. 101, No. 17, October 2012, p. 173903.
51. J. M. Wilson, R. Bashirullah, D. P. Nackashi, D. A. Winick, B. E. Duewer and P. D. Franzon, "Design of Rotating MEMS Tunable Capacitors for use at RF and Microwave Frequencies," *Proceedings of the SPIE*, Vol. 4593, 2001, pp. 186-197.
52. A. S. Y. Poon and M. Taghivand, "Supporting and Enabling Circuits for Antenna Arrays in Wireless Communications," *Proceedings of the IEEE*, Vol. 100, No. 7, July 2012, 2207-2218.
53. Y. Cho, J. J. Kim, D. -H. Kim, S. Lee, H. Kim, C. Song, S. Kong, H. Kim, C. Seo, S. Ahn and J. Kim, "Thin PCB-Type Metamaterial for Improved Efficiency and Reduced EMF Leakage in

Ulrich L. Rohde, Federal Armed Forces University, Munich, Germany ; Ajay K. Poddar, Synergy Microwave, NJ

- Wireless Power Transfer Systems," *IEEE Transactions on Microwave Theory and Techniques*, Vol. 64, No. 2, February, 2016 pp. 353-364.
54. A. Fuzfa, "How Current Loops and Solenoids Curve Space-Time," *Physical Review D*, V3, December 2015.
 55. W. Chaibi, R. Geiger, B. Canuel, A. Bertoldi, A. Landragin and P. Bouyer, "Low Frequency Gravitational Wave Detection With Ground Based Atom Interferometer Arrays," *Physical Review D*, January 2016.
 56. S. M. Anlage, "The Physics and Applications of Superconducting Metamaterials," *Journal of Optics*, Vol. 13, No. 2, April 2010.
 57. P. Jung, A. V. Ustinov and S. M. Anlage, "Progress in Superconducting Metamaterials," *Superconductor Science Technology*, Vol. 27, May 2014.
 58. Z. Wang, Y. D. Chong, J. D. Joannopoulos and M. Soljačić, "Reflection-Free One-Way Edge Modes in a Gyromagnetic Photonic Crystal," *Physical Review Letters*, Vol. 100, No. 1, February 2008.
 59. Z. Wang, Y. Chong, J. D. Joannopoulos and M. Soljačić, "Observation of Unidirectional Backscattering-Immune Topological Electromagnetic States," Vol. 461, No. 7265, October 2009, pp. 772–775.
 60. J. Ningyuan, C. Owens, A. Sommer, D. Schuster and J. Simon, "Time- and Site-Resolved Dynamics in a Topological Circuit," *American Physical Society*, Vol. 5, No. 2, June 2015.
 61. L. T. Huang and D. H. Lee, "Topological Insulators on a Möbius Strip," *Physical Review B*, Vol. 84, No. 19, November 2011.

Möbius Metamaterial Strips: Opportunity, Trends, Challenges and Future

The MMS (Metamaterial Möbius Strip) is an artificial composite structure with a negative index of refraction ($n = -\sqrt{\epsilon\mu}$; $\epsilon < 0$, $\mu < 0$), where n is the refractive index, ϵ is the electrical permittivity and μ is the magnetic permeability of the medium. It has emerged as a cutting edge of science relating physics, chemistry, biology, material science, optics, acoustics and electronics. For most naturally existing materials, μ is close to 1; hence, magnetic susceptibility of natural materials is small as compared to the electric/dielectric susceptibility. This phenomenon limits the interaction of atoms to the electric component of the electromagnetic (EM) wave, leaving the magnetic component mostly unexploited. Magnetism is primarily weak at optical frequencies as well, because the relaxation times of paramagnetic and ferromagnetic processes are considerably longer than an optical period, electron movement in atoms is the only mechanism for creating the magnetic response. This is why the magnetic field component is usually not involved in light-matter interactions.

Ulrich L. Rohde, Federal Armed Forces University, Munich, Germany ; Ajay K. Poddar, Synergy Microwave, NJ

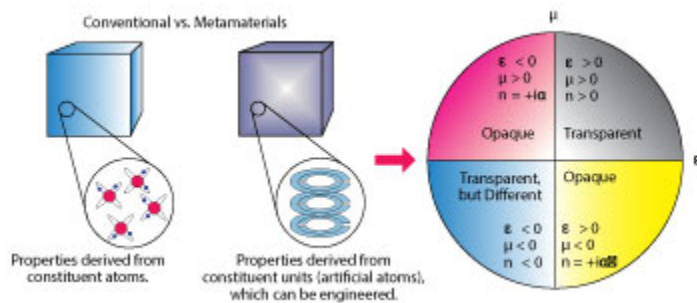
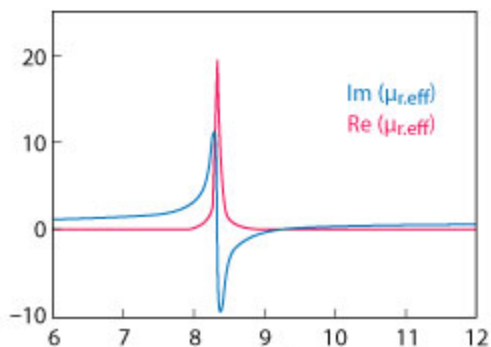
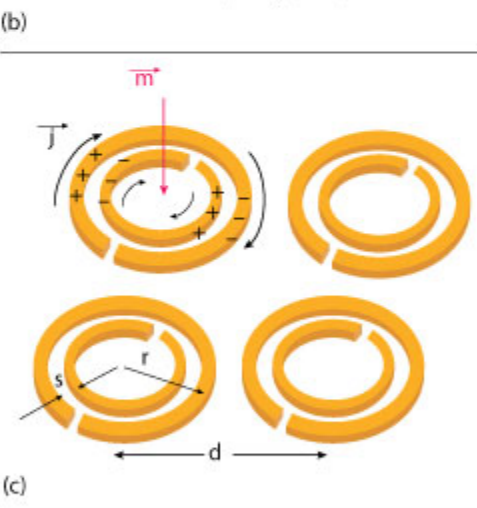
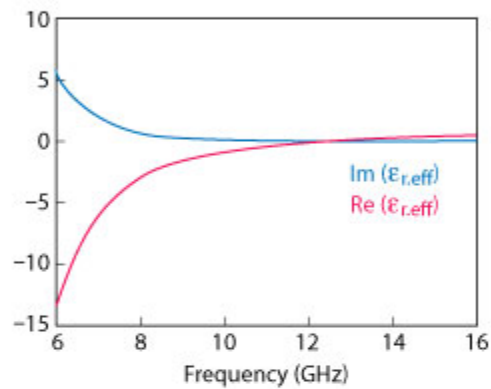
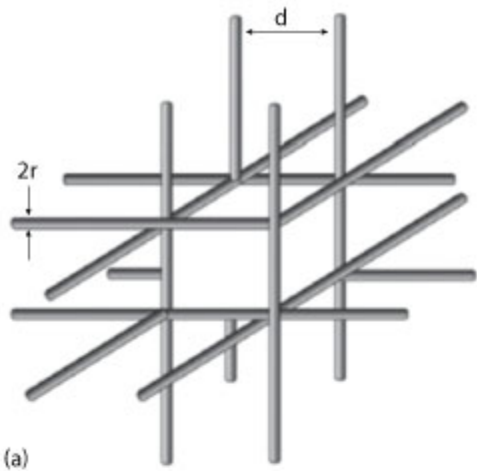


Figure 1 Characteristics of conventional materials vs. metamaterials.

The reason for weak magnetism is mainly due to limitations of the material properties imposed by chemical composition and constituent components (atoms and molecules). On the contrary, MMS resonant nanostructures, in principle, can exhibit a broad range of magnetic permeability values.¹⁻⁷⁵ A number of stimulating phenomena and applications associated with MMS structures are discussed in part 1 (MWJ May 2016) and part 2 (MWJ June 2016) of this series. This issue addresses the prospects, challenges and future directions of MMS inspired components for various applications including the Gravitational Casimir Effect.

Ulrich L. Rohde, Federal Armed Forces University,
Munich, Germany ; Ajay K. Poddar, Synergy
Microwave, NJ



Ulrich L. Rohde, Federal Armed Forces University, Munich, Germany ; Ajay K. Poddar, Synergy Microwave, NJ

Figure 2 Typical negative index structure for the realization of artificial electric and magnetic responses; periodic wires arranged in a simple cubic lattice (a) effective permittivity of wire medium, acting as dilute metal with extremely low plasma frequency (b) a magnetic field penetrating an SRR induces a current, and hence, a magnetic moment (c) and SRR effective permeability at resonance (d).⁸

Recent research in the field of metamaterials⁶⁹⁻⁷⁵ has not only established interesting physical phenomena but also lead to opportunities for utilizing negative index components and devices for next generation energy-efficient electronic circuits and systems. **Figure 1** compares the properties of natural and artificially engineered composite materials.¹ Unlike conventional materials that interact with EM waves based on their chemical compositions, the properties of metamaterials are derived from their topologies and geometric structures.

The typical metamaterial consists of periodically or arbitrarily disseminated structured cells with dimensions and spacings much smaller than a wavelength of the incident EM waves.¹⁻³ As a consequence, the microscopic detail of each unit cell structure cannot be sensed by EM waves. What is important to understand is the average result of the collective response of the entire assemblage, comprised of inhomogeneous matter. In other words, such a collection of inhomogeneous matter can be characterized by an equivalent homogenous material with effective constitutive relative permittivity ($\epsilon_{r,eff}$) and permeability ($\mu_{r,eff}$) at the macroscopic level. The key aspect of an MMS inspired structure is that effective permittivity ($\epsilon_{r,eff}$) and permeability ($\mu_{r,eff}$) can be controlled and tuned by a suitably designed disseminated element for broadband operation.

In classical EM theory, the characteristics of matter illustrated in Figure 1 can be described by the Drude–Lorentz model⁶ as

$$\epsilon_r(\omega) = 1 - \frac{\omega_{p,e}^2}{\omega^2 - \omega_{0,e}^2 + i\omega\gamma_e} \quad (1)$$

$$\mu_r(\omega) = 1 - \frac{\omega_{p,m}^2}{\omega^2 - \omega_{0,m}^2 + i\omega\gamma_e} \quad (2)$$

where ω_p is the plasma frequency, ω_0 is the resonant frequency, subscripts ‘e’ and ‘m’ represent electric and magnetic response, and γ is the damping factor associated with material losses.

Figure 2 shows a typical metamaterial structure,⁴⁻⁵ realized by the combination of split ring resonators (SRR) and thin metallic wires. The effective relative permittivity ($\epsilon_{r,eff}$) and effective relative permeability ($\mu_{r,eff}$) obey the Drude–Lorentz⁶⁻⁹ model as

Ulrich L. Rohde, Federal Armed Forces University, Munich, Germany ; Ajay K. Poddar, Synergy Microwave, NJ

$$\epsilon_{r,\text{eff}}(\omega) = 1 - \frac{\omega_{p,\text{eff}}^2}{\omega(\omega + i\omega\gamma_{\text{eff}})},$$

$$\omega_{p,\text{eff}}(\omega) = \frac{e^2}{\epsilon_0} \frac{n_{e,\text{eff}}}{m_{e,\text{eff}}} = \frac{2\pi c^2}{d^2 \ln \frac{d}{r}},$$

$$\gamma_{\text{eff}} = \epsilon_0 \frac{d^2 \omega_p^2}{\pi r^2 \sigma} \approx 0.1 \omega_{p,\text{eff}} \quad (3)$$

$$\mu_r(\omega) = 1 = \frac{F \omega^2}{\omega^2 - \omega_0^2 + i\Gamma\omega}, F = \frac{\pi \times r^2}{d^2},$$

$$\omega_0 = \sqrt{\frac{3sc^2}{\pi^2 r^3}}, \Gamma = \frac{2}{r \sigma_0} \quad (4)$$

where σ is the conductivity of metal wire, d is the lattice constant, ω_0 represents the resonant frequency, $\omega_{p,\text{eff}}$ is the effective plasma frequency, F is the filling ratio of the SRR, and Γ is the damping term. From (3), the effective plasma frequency is $\omega_{p,\text{eff}} = 7.52 \times 10^{10}$ rad/sec; assuming that the metal wire conductivity $\sigma = 107 \Omega^{-1} \text{ m}^{-1}$, the metal wire radius $r = 1 \times 10^{-6}$ meters and the lattice constant $d = 3.5 \times 10^{-3}$ meters. From (4), the resonant frequency $f_0 = 8.324$ GHz; assuming that for the SRR, $d = 4 \times 10^{-3}$ meters, $r = 1 \times 10^{-3}$ meters, and $s = 1 \times 10^{-4}$ meters. This corresponds to a free space wavelength of 3.6×10^{-2} meters which is about 10 times larger than d .

From (3) and (4), $\epsilon_{r,\text{eff}}$ of metallic wire and $\mu_{r,\text{eff}}$ of the SRR exhibit the typical Drude-Lorentz characteristics,⁸ plotted in **Figures 2b** and **d**. Equations (3) and (4) provide approximate analytical solutions for the effective constitutive parameters (permittivity, permeability) with reasonable accuracy, valid for the simple structure shown in Figure 2. For a complex structure, however, and especially for an MMS inspired negative index metasurface, this is not true.

The alternative approach is to retrieve the effective parameters from numerical simulations⁹⁻¹² described in detail.⁷⁰ The first step of the retrieval procedure is to calculate the transmission and reflection of the composite MMS based on numerical algorithms, such as finite-difference time-domain (FDTD) and finite element method (FEM). Some commercial software, including ADS, Ansys HFSS, CST Microwave Studio, COMSOL Multiphysics and SONNET are widely used but none of these provide error free solutions. The refractive index and impedance are related to the transmission coefficient (t) and reflection coefficient (r) by equations⁹

Ulrich L. Rohde, Federal Armed Forces University,
Munich, Germany ; Ajay K. Poddar, Synergy
Microwave, NJ

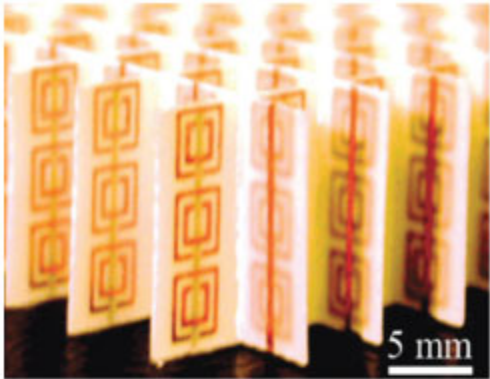
$$Z_{\text{eff}} = \pm \frac{(1+r)^2 - t^2}{(1-r)^2 - t^2}^{1/2} \quad (5)$$

$$n_{\text{eff}} = \pm \cos^{-1} \left[\frac{1}{k_0 L} \frac{1-r^2+t^2}{2t} + \frac{2\pi m}{k_0 L} \right],$$
$$k_0 = \frac{2\pi}{\lambda_0} \quad (6)$$

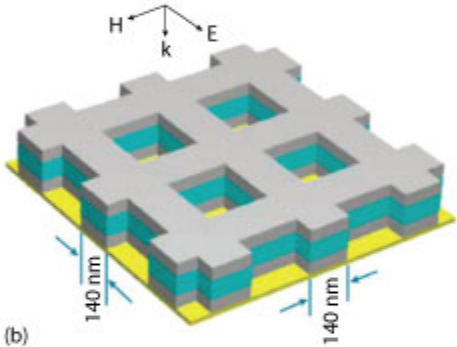
$$\epsilon_{r,\text{eff}}(\omega) = \frac{n_{\text{eff}}(\omega)}{Z_{\text{eff}}(\omega)} \quad (7)$$

$$\epsilon_{r,\text{eff}}(\omega) = n_{\text{eff}}(\omega) \times Z_{\text{eff}}(\omega) \quad (8)$$

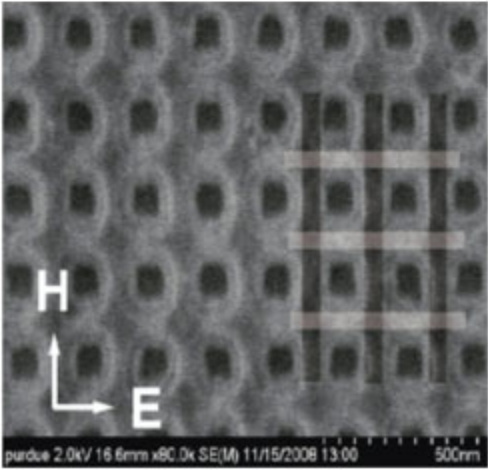
Ulrich L. Rohde, Federal Armed Forces University,
 Munich, Germany ; Ajay K. Poddar, Synergy
 Microwave, NJ



(a)



(b)



(c)

Figure 3 Typical arrangement of artificially engineered negative index medium; copper SRRs and wires deposited lithographically on standard circuit boards for microwave frequencies where the size of the unit cell is 5×10^{-3} meters (a)¹³NIM fishnet structure for the visible region (yellow) where two layers of metal mesh (gray) are separated by a dielectric layer (cyan) (b) and a scanning electron microscope (SEM) image of the fishnet structure fabricated by electron beam lithography (c).¹⁴

where k_0 is the wave vector in vacuum, L is the thickness of the metamaterial, and m is an integer.

Ulrich L. Rohde, Federal Armed Forces University, Munich, Germany ; Ajay K. Poddar, Synergy Microwave, NJ

From Equations (5) and (6), effective impedance and refractive index can be determined provided that the metamaterial structures act like a passive medium; this implies that the real part of z_{eff} and the imaginary part of n^{eff} are positive.⁹ Note that the effective parameter retrieval process is a challenging task, especially when metamaterial structures fall into the category of anisotropic or bi-anisotropic, and EM wave is obliquely incident.¹² Parameter retrieval becomes even more complex for nonlinear metamaterial composite structures.

The metamaterial structure shown in **Figure 3a** is a combination of metallic wires and SRRs; however, these artificially engineered structures pose fabrication problems. A simplified structure reported in literature is the Fishnet structure¹⁴⁻¹⁶ that consists of two layers of metal meshes separated by a dielectric layer (see **Figures 3b** and **3c**). Paired stripes oriented parallel to the electric field provide negative $\epsilon_{r,\text{eff}}(\omega)$, while the other pairs of stripes parallel to the magnetic field support negative $\mu_{r,\text{eff}}(\omega)$. Since the dielectric thickness of the fishnet structure is easy to control, the fabrication burden is significantly eased as compared to the conventional approach of using SRRs and metallic wires.⁸ Moreover, in order to produce a negative refractive index, EM waves are incident normal to the fishnet surface, whereas the structure fabricated by SRRs and wires requires oblique incidence to excite SRRs with out-of-plane magnetic fields for strong magnetic resonances.

METAMATERIAL OPPORTUNITIES AND EMERGING TRENDS

The aerospace, defense and biomedical electronics sectors are viewed as the most vibrant market areas for metamaterial products applications. The rise of drones and related weight considerations, the need for improved military communications, and the burgeoning demand for new and more sophisticated biosensors are all areas where metamaterial technology can help propel things forward.

Imaging

Metamaterial structures have been used in magnetic imaging, microwave circuit components, antennas, and perfect lenses with imaging resolutions beyond the diffraction limit.¹⁻²¹ In conventional optical systems, it is not possible to determine two points separated less than $\lambda/2n$, where n is the refractive index of the ambient medium. This fundamental limitation exists because the information of the object's fine features and textures are carried by evanescent waves, which exponentially decay in space. All the information relevant to the sub-wavelength details of the object is lost, before reaching the imaging plane. It is interesting to note that a metamaterial slab acts as a perfect lens to recover all the lost information.²⁰ This extraordinary property of perfect lens arises from the fact that the initially decayed evanescent waves are now amplified through the slab. Meanwhile, the propagating waves are focused due to the negative refraction and reversed phase front. As a result, a metamaterial slab, incredibly, brings both propagating and evanescent waves to a perfect focus (see **Figures 4a** and **4b**), without suffering the traditional constraint imposed by the diffraction limit.

This shows promise in the realization of metamaterial super lenses, which are lenses that are almost free of aberrations and that can focus images below the diffraction limit. The recorded image "NANO" (see **Figure 5b**) reproduces the fine features from the object mask (see **Figure 5a**) in all directions with good fidelity, while the image in the control experiment without the super lens (see **Figure 5c**) shows a much wider line width.²² In the seminal paper, Pendry et al.,⁵ predicted the

Ulrich L. Rohde, Federal Armed Forces University, Munich, Germany ; Ajay K. Poddar, Synergy Microwave, NJ

enhanced nonlinear optical properties by inserting nonlinear elements into the gap of SRRs, arising from the giant local-field amplification.

Figure 6 shows the typical measurement setup for an MRI measurement at 8.5 MHz for prostate cancer detection. Metamaterial inspired ($\mu = -1$) split ring resonators loaded with capacitors and inductors enabled a 20 times increase in the magnetic field. As shown in **Figure 6b**, the lens resolves two magnetic sources indistinguishable without the lens.⁷⁶

Lightweight Metamaterial

Metamaterial technology is an enabler to build lighter and more compact antenna systems. **Figure 7** shows the performance of the typical light weight inspired monopole antenna. The data shows that the bandwidth increased to over an octave while preserving the radiation characteristics of a simple monopole.

Light Manipulation

Metamaterial technology offers unparalleled opportunities for light manipulation. Recent developments in the field have fueled new opportunities for light propagation, establishing a new paradigm for spin and quantum related phenomena in optical physics. Nonlinear metamaterials, with properties depending on the intensity of EM waves, is an emerging research topic with novel phenomena such as hysteretic transition,²³ unusual wave mixing²⁴ and solitary wave propagation.²⁵⁻²⁶

Ulrich L. Rohde, Federal Armed Forces University,
Munich, Germany ; Ajay K. Poddar, Synergy
Microwave, NJ

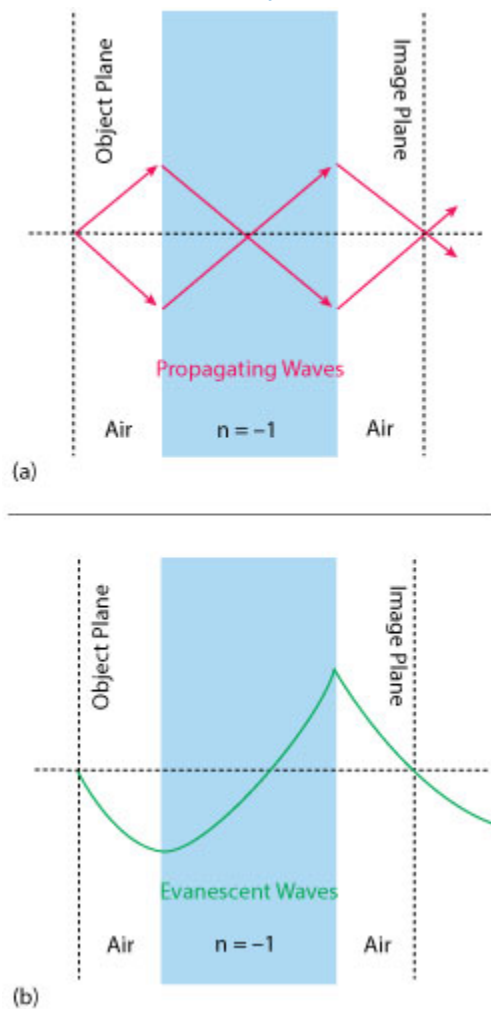


Figure 4 Metamaterial slab shows the properties of a perfect lens; focusing all light rays from a point source (a) and amplifying evanescent waves (b) to provide perfect imaging at the image plane.

The other interesting phenomenon is the reversed Manley–Rowe relation and backward phase matching condition for second-harmonic generation (SHG) or optical parametric amplification (OPA).²⁷ Suppose a metamaterial has a negative refractive index at the fundamental frequency ω_1 and a positive refractive index at the second-harmonic frequency ω_2 . At ω_1 the energy flow (Poynting vector) points from left to right, for example; then the wave vector \vec{k} must point from right to left arising from negative index sample at ω_1 . The phase matching condition i.e. $\vec{k}_2 = 2\vec{k}_1$ requires that the wave vector \vec{k}_2 at the second harmonic frequency ω_2 also travels from the right to the left. Since the metamaterial possesses a positive refractive index at ω_2 , the energy flow is at the same direction as the wave vector. As a result, the second harmonic signal is maximal at the incident interface rather than at the exit interface of the metamaterial slab, in sharp contrast to SHG in normal dielectric materials (see **Figure 8**). Moreover, artificial magnetic metamaterials could provide additional ways to boost the nonlinear process.²⁸ In terms of applications, tunable metamaterials²⁹⁻

Ulrich L. Rohde, Federal Armed Forces University, Munich, Germany ; Ajay K. Poddar, Synergy Microwave, NJ

³⁰ and memory devices³¹ have been experimentally demonstrated based on nonlinear metamaterial composites.

Metamaterials may manifest fascinating phenomena in the quantum world. In principle, the metamaterial concept could be applied to any wave at any scale, including the matter wave which is the wave description of particles, such as electrons and neutrons, in quantum mechanics. Indeed, researchers have made theoretical efforts in this direction. Cheianov et al.,³² theoretically demonstrated that negative refraction and focusing of electrons can be achieved in graphene (see **Figure 9**), a monolayer of graphite.

Figure 10 illustrates the technology and transformation optics approach that enables unprecedented design flexibility and novel device applications.

TECHNOLOGY CHALLENGES

The metamaterial technology and transformation optics shown in Figure 10 promise unparalleled opportunities; but at the same time, metamaterial composites fabrication is challenging. The real challenge is to predict the topology and geometry of negative index microstructures even though they tend to have simple shapes. The topology optimization method allows selection of geometric and topological configuration of multi-physical functional materials while taking into account the MMS material composition. Commercialization is primarily a manufacturing problem due to the lack of effective tools to economically pattern large volumes of material.

The immediate step is to improve the homogenization methodology for the design of multi-function nonlinear metamaterial devices, improving the bandwidth, and providing smaller/more compact structures. More investigation of pulse propagation in optical fiber and speed control by means of nonlinear refractive index for the space-time cloak, solitons and their variants is needed in negative refractive index composites.

FUTURISTIC OUTLOOK

The emerging future is likely to be in the area of the Gravitational Casimir effect and signal processing where the space-time cloak acts as a means of prioritizing data channels, rather than theoretically attempting to combine space-time and spatial cloaks. In addition to this, Möbius transformations that exploit hyperbolic characteristics could be interesting for a variety of Minkowski-based relativistic scenarios including spinning cosmic strings.

Ulrich L. Rohde, Federal Armed Forces University,
Munich, Germany ; Ajay K. Poddar, Synergy
Microwave, NJ

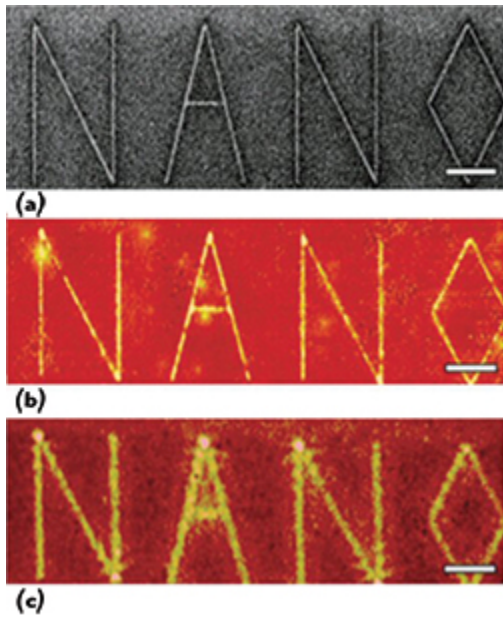
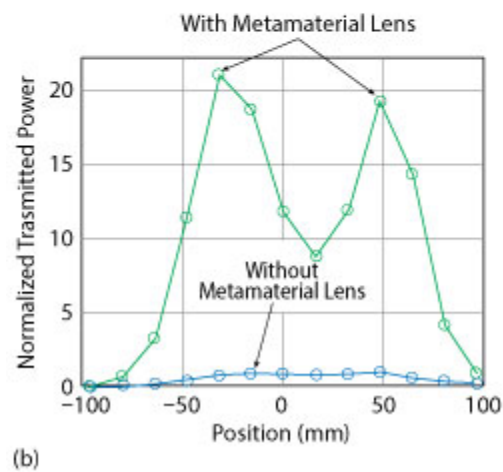
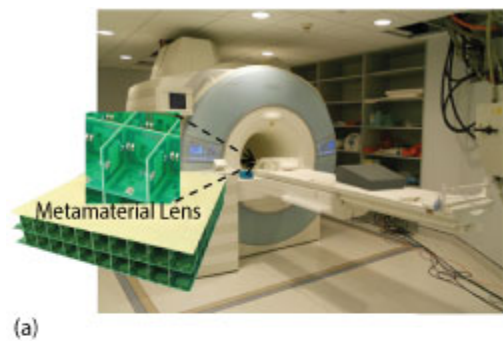


Figure 5 Experimental demonstration of an optical silver superlens; object mask (a) metamaterial superlens image (b) and conventionally focused image (c).



Ulrich L. Rohde, Federal Armed Forces University, Munich, Germany ; Ajay K. Poddar, Synergy Microwave, NJ

Figure 6 MRI measurement setup shows the use of metamaterial lens for imaging (a) and the measurement response with and without the lens (b).⁷⁶

Gravitational Casimir Effect

Figure 11 shows the practical evidence of the Casimir force 'F' on parallel plates kept in vacuum. The effective force $F \propto A/d^4$, where A is the area of plate and d is the distance between the plates. The Casimir force⁶⁷ (see Figure 12) arises from the interaction of the surfaces with the surrounding electromagnetic spectrum, and includes a complex dependence on the full dielectric function of both surfaces and the region between. On the more theoretical side, the MMI structure can produce a powerful Casimir effect (force from nothing), which will allow the transport of matter; this implies the ability to attract or push away physical matter.

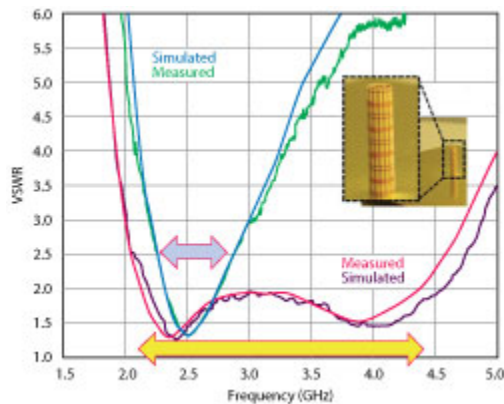
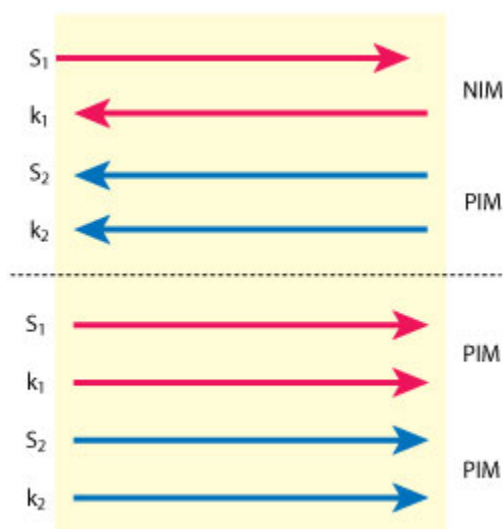


Figure 7 Data showing increased antenna bandwidth using metamaterial.⁷⁷ Simulated monopole alone (blue line), measured monopole alone (green line), simulated monopole with metamaterial (red line), measured monopole with metamaterial (purple line).



Ulrich L. Rohde, Federal Armed Forces University, Munich, Germany ; Ajay K. Poddar, Synergy Microwave, NJ

Figure 8 Schematic of a second harmonic generation with negative index materials in comparison with normal SHG with only positive index materials.

As shown in Figure (12),⁵⁶ the polaritonic contribution is responsible for the change in sign of the Casimir force between a metallic and a metamaterial mirror. For $L \geq \lambda r/5$ the binding TM polariton, which dominates at short distance, is overwhelmed by the joint repulsion due to the anti-binding TM and TE polaritons. This shows that, for mixed configurations as well, surface plasmons are crucial in determining both the strength and the sign of the Casimir interaction.

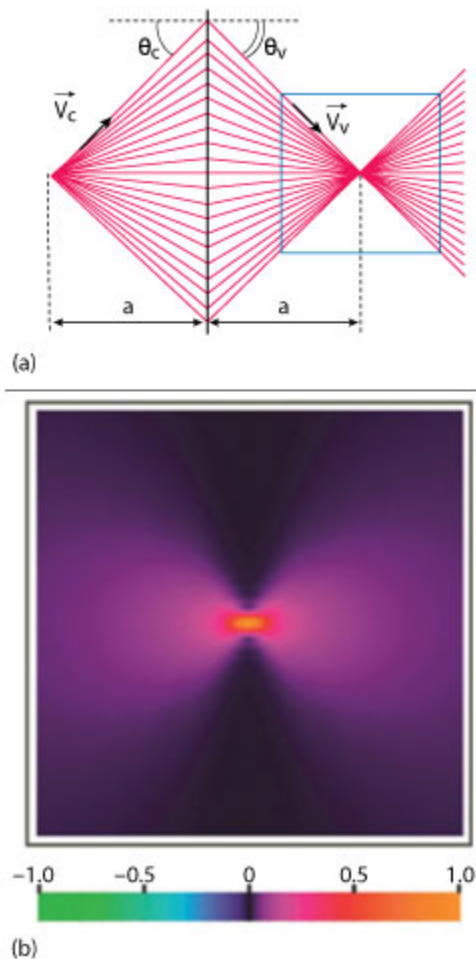


Figure 9 Focusing of electrons by a grapheme p–n junction; trajectories of electrons diverging from a source at distance a from the junction and becoming convergent after negative refraction (a) and the interference-induced pattern in the charge current near the focal image (b).³²

One of the exciting properties of MMI structures is that they can bend light in a way that is mathematically equivalent to the way space-time bends light, enabling topological exploration for the realization of low cost gravitational wave detector. **Figure 13** shows the gravitational Casimir effect, with a two plate setup. The change in the refractive index of the plates causes the gravitational wave to refract, where k represents the wave vector of the incident, transmitted, and reflected gravitational

Ulrich L. Rohde, Federal Armed Forces University, Munich, Germany ; Ajay K. Poddar, Synergy Microwave, NJ

waves, and γ is the corresponding angle with respect to the surface normal.⁶⁸ The Casimir effect has also been investigated in weak gravitational fields to see the effect the slightly curved space time background would have on the Casimir energy.⁶⁸

Gravitational Wave Reflector and the Gravitational Characteristic Impedance of Free Space

Thin Metamaterial superconducting films are predicted to be highly reflective mirrors for gravitational waves at microwave frequencies. The quantum mechanical non-localizability of the negatively charged Cooper pairs, which are protected from the localizing effect of decoherence by an energy gap, causes the pairs to undergo non-picturable, non-geodesic motion in the presence of a gravitational wave⁵⁷. This non-geodesic motion, which is accelerated motion through space, leads to the existence of mass and charge super currents inside the Metamaterial superconducting film. On the other hand, the decoherence-induced localizability of the positively charged ions in the lattice causes them to undergo picturable, geodesic motion as they are carried along with space in the presence of the same gravitational wave. The resulting separation of charges leads to a virtual plasma excitation within the film that enormously enhances its interaction with the wave, relative to that of a neutral super fluid or any normal matter. The existence of strong mass super currents within a superconducting film in the presence of a gravitational wave, dubbed the H-C (Heisenberg-Coulomb) effect, implies the specular reflection of a gravitational microwave from a film whose thickness is much less than the penetration depth of the material, in close analogy with the electromagnetic case. The argument is developed by allowing classical gravitational fields, which obey Maxwell-like equations, to interact with quantum matter, which is described using the BCS and Ginzburg-Landau theories of superconductivity, as well as a collisionless plasma model.

Experiments at the frontiers of quantum mechanics and gravitation are rare. Minter⁵⁷ et al argue for a claim that may lead to several new types of experiments, namely, that a superconducting film whose thickness is less than the London penetration depth of the material can specularly reflect not only electromagnetic (EM) microwaves, as has been experimentally demonstrated⁵⁸⁻⁵⁹ but gravitational (GR) microwaves as well. The basic motivation lies in the well known fact that Einstein's field equations lead, in the limits of weak GR fields and non-relativistic matter, to gravitational Maxwell-like equations,⁶⁰ which in turn lead to boundary conditions for gravitational fields at the surfaces of the superconducting films homologous to those of electromagnetism. All radiation fields, whether electromagnetic or gravitational, will be treated classically, whereas the superconductors with which they interact will be treated quantum mechanically.

The first claim is that a GR microwave will generate quantum probability super currents, and thus mass and electrical super currents, inside a superconductor, due to the quantum mechanical non-localizability of the Cooper pairs within the material. The non-localizability of Cooper pairs, which is ultimately due to the Uncertainty Principle (UP), causes them to undergo non-picturable, non-geodesic motion in the presence of a GR wave. This non-geodesic motion, which is accelerated motion through space, leads to the existence of mass and charge super-currents inside a superconductor. By contrast, the localizability of the ions within the superconductor's lattice causes them to undergo picturable, geodesic motion, i.e., free fall, in the presence of the same wave. The resulting relative motion between the Cooper pairs and the ionic lattice causes the electrical polarization of the superconductor in the presence of a GR wave, since its Cooper pairs and ions carry not only mass but oppositely signed charge as well.

Ulrich L. Rohde, Federal Armed Forces University, Munich, Germany ; Ajay K. Poddar, Synergy Microwave, NJ

Furthermore, the non-localizability of the Cooper pairs is “protected” from the normal process of localization, i.e., from decoherence, by the characteristic energy gap of the Bardeen-Cooper-Schrieffer (BCS) theory of superconductivity. The decoherence of entangled quantum systems such as Cooper pairs (which are in the spin-singlet state) is the fundamental cause of the localizability of all normal matter.⁶¹

Minter⁵⁷ et claimed that the mass super-currents induced by a GR wave are much stronger than what one would expect in the case of a neutral super-fluid or any normal matter, due to the electrical polarization of the superconductor caused by the wave. This is what referred to as the “Heisenberg-Coulomb (H-C) effect.” The magnitude of the enhancement due to the H-C effect (is given by the ratio of the electrical force to the gravitational force between two electrons,

The Maxwell-like representation of Einstein’s equations of general relativity describe the coupling of weak gravitational fields to slowly moving matter. In the asymptotically flat space-time coordinate system of a distant inertial observer, the four equations in SI units are:

$$\frac{q^2}{4\pi\epsilon_0 G m_e^2} = 4.2 \times 10^{42} \quad (9)$$

where q is the electron charge, m_e is the electron mass, ϵ_0 is the permittivity of free space, and G is Newton’s constant. The vastness of equation (9) implies the possibility of an enormous back-action of a superconductor upon an incident GR wave, leading to its reflection.

There are four conventionally accepted fundamental force of nature (i) gravitational, (ii) electromagnetic, (iii) strong nuclear, and (iv) weak nuclear. Each one is understood as the dynamics of a field. The gravitational force is modeled as a continuous classical field. Interestingly, of the four fundamental forces of nature, only gravity and electricity have long range, inverse square laws.

The pure number obtained in (9) by taking the ratio of these two inverse-square laws is therefore just as fundamental as the fine structure constant. Because this number is so large, the gravitational force is typically ignored in treatments of the relevant quantum physics. But for a semi-classical treatment of the interaction of a superconductor with a GR wave must account for both the electrodynamics and the gravito-electrodynamics of the superconductor, since both play an important role in its overall response to a GR wave.

Gravitational Characteristic Impedance of Free Space

The Maxwell like representation of the Einstein equations of general relativity can be described the coupling of weak GR fields to slowly moving matter. In the asymptotically flat space-time coordinate system of a distant inertial observer, the four equations in SI units are

Ulrich L. Rohde, Federal Armed Forces University,
Munich, Germany ; Ajay K. Poddar, Synergy
Microwave, NJ

$$\nabla \times \bar{E}_G = -\frac{\partial \bar{E}_G}{\partial t} \quad (10)$$

$$\nabla \times \bar{B}_G = \mu_G \left(-j_G + \epsilon_G \frac{\partial \bar{E}_G}{\partial t} \right) \quad (11)$$

$$\nabla \cdot \bar{E}_G = -\frac{\partial_G}{\epsilon_G} \quad (12)$$

$$\nabla \cdot \bar{B}_G = 0 \quad (13)$$

where the gravitational analog of the electric permittivity ϵ_G and magnetic permeability μ_G of free space is given by

$$\mu_G = \frac{4\pi G}{c^2} = 9.3 \times 10^{-27} \quad (14)$$

$$\epsilon_G = \frac{1}{4\pi G} = 1.2 \times 10^9 \quad (15)$$

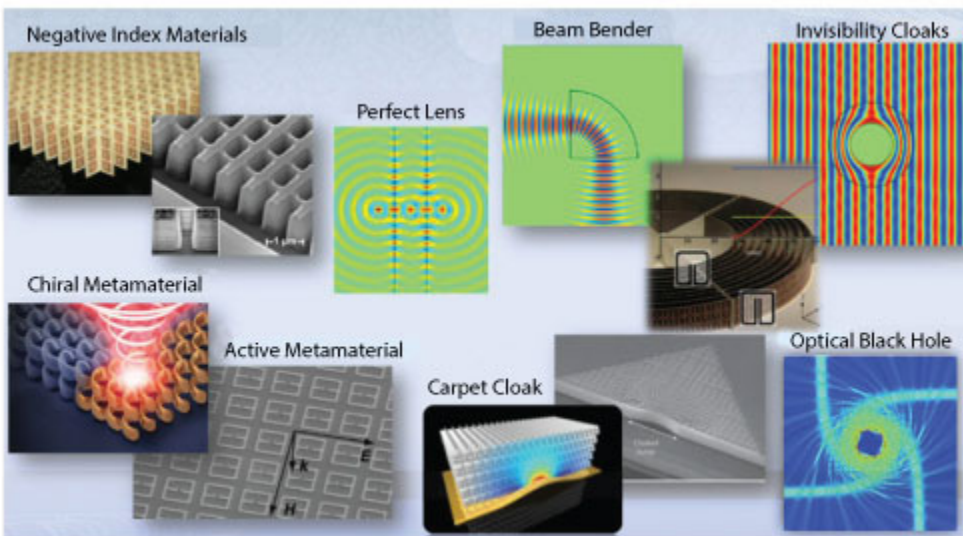


Figure 10 Metamaterial technology and transformation optics approaches.

Ulrich L. Rohde, Federal Armed Forces University, Munich, Germany ; Ajay K. Poddar, Synergy Microwave, NJ

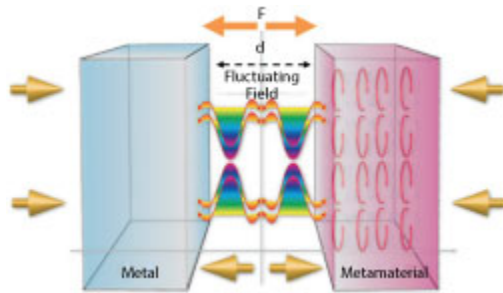


Figure 11 The repulsive Casimir force 'F' on parallel plate kept in vacuum.⁵⁶

The value of ϵ_G is fixed by demanding that Newton's law of gravitation be recovered from the Gauss-like law (13), whereas the value of μ_G is fixed by the linearization procedure from Einstein's field equations. These two constants express the strengths of the coupling between sources (i.e., of masses and mass currents, respectively) and gravitational fields, and are analogous to the two constants ϵ_0 (the permittivity of free space) and μ_0 (the permeability of free space), which express the strengths of coupling between sources (charges and charge currents, respectively) and electromagnetic fields in Maxwell's theory.

In the above set of equations, the field $\bar{\mathbf{E}}_G$ is the gravito-electric field, which is to be identified with the local acceleration g of a test particle produced by the mass density ρ_G , in the Newtonian limit of general relativity. The field $\bar{\mathbf{B}}$ is the gravito-magnetic field produced by the mass current density j_G and by the gravitational analog of the Maxwell displacement current density

$$\epsilon_G \left(\frac{\partial \bar{\mathbf{E}}_G}{\partial t} \right)$$

of the Ampere-like law (11). The resulting magnetic-like field $\bar{\mathbf{B}}_G$ can be regarded as a generalization of the Lense-Thirring field of general relativity. Because these equations are linear, all fields will obey the superposition principle not only outside the source (i.e., in the vacuum), but also within the matter inside the source, provided the field strengths are sufficiently weak and the matter is sufficiently slowly moving. Note that the fields $\bar{\mathbf{E}}_G$ and $\bar{\mathbf{B}}_G$ in the above Maxwell-like equations will be treated as classical fields, just like the fields $\bar{\mathbf{E}}_G$ and $\bar{\mathbf{B}}_G$ in the classical Maxwell's equations.

Ulrich L. Rohde, Federal Armed Forces University,
Munich, Germany ; Ajay K. Poddar, Synergy
Microwave, NJ

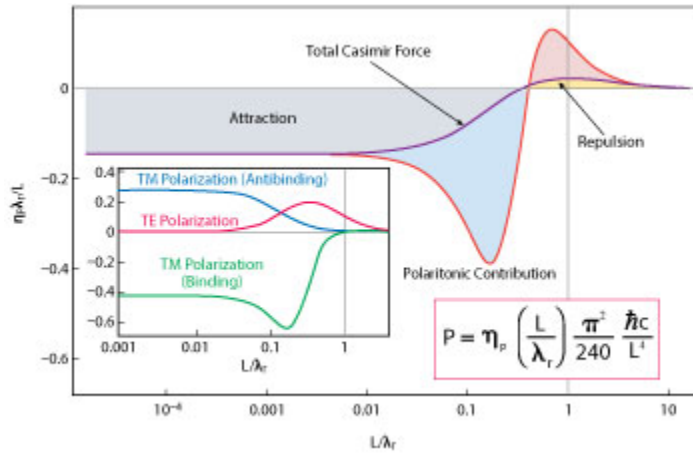


Figure 12 The polaritonic contribution is responsible for the change in sign of the Casimir force between a metallic and a metamaterial mirror.⁵⁶

As noted earlier, Cooper pairs cannot freely fall along with the ionic lattice in response to an incident GR wave because the UP forbids such pairs from having classical trajectories, i.e., from traveling along geodesics. An incident field E will therefore cause the Cooper pairs to undergo non-geodesic motion, in contrast to the geodesic motion of the ions inside the lattice. This entails the existence of mass currents (as well as charge currents) from the perspective of a local, freely falling observer who is located near the surface of the superconducting film anywhere other than at its center of mass. These mass currents will be describable by a gravitational version of Ohm's law

$$\mathbf{J}_G = (\boldsymbol{\omega}) = \boldsymbol{\sigma}_{S,G}(\boldsymbol{\omega}) \bar{\mathbf{E}}_{G-INSIDE}(\boldsymbol{\omega}) \quad (16)$$

where $\mathbf{J}_G(\boldsymbol{\omega})$ is the mass-current density at frequency $\boldsymbol{\omega}$, $\check{\delta}_{S,G} = \check{\delta}_{1S,G}(\boldsymbol{\omega}) + i\check{\delta}_{2S,G}(\boldsymbol{\omega})$ is the complex mass-current conductivity of the film at the frequency $\boldsymbol{\omega}$ in its linear response to the fields of the incident GR wave, and $\bar{\mathbf{E}}_{G-INSIDE}(\boldsymbol{\omega})$ is the driving gravito-electric field inside the film at frequency $\boldsymbol{\omega}$.

The existence of these mass currents can also be inferred from DeWitt's minimal coupling rule for superconductors⁶². The real part of the mass conductivity, $\check{\delta}_{1S,G}(\boldsymbol{\omega})$, describes the superconductor's dissipative response to the incident gravito-electric field, while the imaginary part, $\check{\delta}_{2S,G}(\boldsymbol{\omega})$ describes its non-dissipative response to the same field. The basic assumption behind equation (16) is that the mass-current density in any superconductor responds linearly to a weak GR wave at the driving frequency. One should view $\check{\delta}_{S,G}(\boldsymbol{\omega})$ as a phenomenological quantity, which, like the electrical conductivity $\check{\delta}_S$, must be experimentally determined. In any case, the resulting optics for weak GR waves will be linear, just like the linear optics for weak EM waves.

An important physical property follows from the above Maxwell-like equations, namely, the characteristic gravitational impedance of free space Z_G ⁶³⁻⁶⁵.

$$Z_G = \sqrt{\frac{\mu_G}{\epsilon_G}} = \frac{4\pi G}{C} = 2.8 \times 10^{-18} \quad (17)$$

Ulrich L. Rohde, Federal Armed Forces University, Munich, Germany ; Ajay K. Poddar, Synergy Microwave, NJ

This quantity is a characteristic of the vacuum, i.e., it is a property of space-time itself, and it is independent of any of the properties of matter per se. As with

$$Z_0 = \sqrt{\frac{\mu_0}{\epsilon_0}} = 377$$

ohms in the EM case,

$$Z_G = \sqrt{\frac{\mu_G}{\epsilon_G}} = 2.8 \times 10^{-28}$$

will play a central role in all GR radiation coupling problems.

In practice, the impedance of a material object must be much smaller than this extremely small quantity before any significant portion of the incident GR-wave power can be reflected. In other words, conditions must be highly unfavorable for dissipation into heat. Because all classical material objects have extremely high levels of dissipation compared to Z_G , even at very low temperatures, they are inevitably very poor GW reflectors.⁶⁵⁻⁶⁶ The question of GW reflection from macroscopically coherent quantum systems such as superconductors requires a separate analysis due to the effectively zero resistance associated with superconductors, i.e., the lack of dissipation exhibited by matter in this unique state, at temperatures near absolute zero.

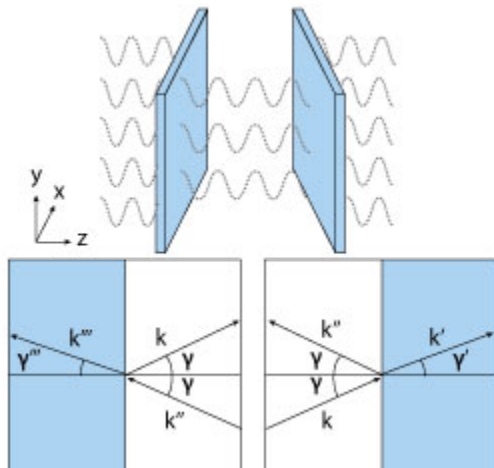


Figure 13 The Gravitational Casimir effect.⁶⁸

Peters⁷⁸ reported on the gravitational refractive index n_G , which was much larger than that generated by just considering induced quadrupole moments, suggesting that his model encapsulates the dominant GW interaction with matter, given as

Ulrich L. Rohde, Federal Armed Forces University, Munich, Germany ; Ajay K. Poddar, Synergy Microwave, NJ

$$n_G = 1 + \frac{2\pi G \rho}{\omega^2} \quad (18)$$

where ρ is the density of the medium.

Minter⁵⁷ et al., give the reflection coefficient of a superconducting film from an incident GW as

$$r_G = \frac{1}{1 + \frac{2\delta^2}{c \times d} \xi} \quad (19)$$

where δ is the EM skin depth of the superconducting film and d is the film thickness.

From (19), the gravitonic contribution to the Casimir pressure for superconducting lead (Pb) of thickness $d = 2$ nm at zero temperature is plotted in **Figure 14**.⁶⁸ The EM skin depth of Pb is $\delta = 37$ nm. This result is compared with the photonic contribution to the Casimir pressure of superconducting lead. The EM reflection coefficient is⁷⁹

$$r_E = \frac{1}{1 + \frac{2\lambda\delta^2}{c \times d} \xi} \quad (20)$$

where $\lambda = 83$ nm is the coherence length. The photonic contribution to the Casimir pressure is calculated by using Equation (19).

James⁶⁸ claims that if measurements of the Casimir pressure plots shown in Figure (14) solid line, then one should conclude that the H-C effect is invalid, if we are to hold on to the idea of the graviton. However, if experiments show the Casimir pressure to be an order of magnitude larger than that predicted from the photonic contribution alone, this would be the first experimental evidence for the validity of the H-C theory and the existence of gravitons. This would open a new field in the way of graviton detection.

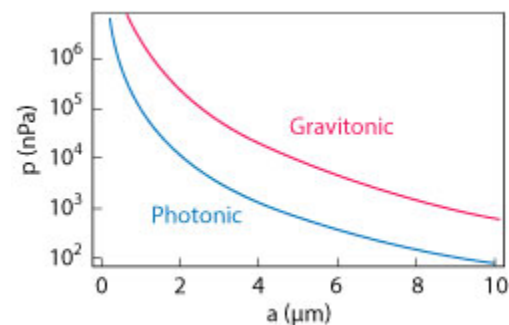


Figure 14 Typical CAD simulated plots of gravitonic (red line) and photonic (blue line) contributions to the Casimir pressure of parallel plates kept in vacuum.⁶⁸

Ulrich L. Rohde, Federal Armed Forces University, Munich, Germany ; Ajay K. Poddar, Synergy Microwave, NJ

CONCLUSION

This series of articles discussed the opportunities, emerging trends, challenges and future direction promoted by the scientists, experimentalists and technologists whose focus is in translating metamaterials into practical systems and devices. Their unique electromagnetic properties have attracted considerable attention from researchers across multiple disciplines. With the complete degree of freedom to control over material properties, what is possible is limited only by our imagination. Magneto electric couplings can be a source of new behavior in Casimir systems, metamaterial Casimir repulsive effects can lead to anti-gravity and low cost solution for levitation. As a final comment, the authors acknowledge that MMS metasurfaces can provide nearly infinite group delay, which is very helpful in understanding Einstein precession, geodetic effects and provides new evidence for refining our understanding of the relativistic corrections to Newtonian celestial mechanics. For example, multi-knots Möbius strips can be considered as tiny strings that can vibrate in multiple dimensions, and depending on how they vibrate, they might be seen in 3-dimensional space as matter, light or gravity. The vibration of the string which determines whether it appears to be matter or energy, and every form of matter or energy is the result of the vibration of the string. The authors consciously set out to describe a model of the universe as a “Möbius Universe,” unbounded in the form of Möbius loop along the plane of space-time fabrics.

ACKNOWLEDGMENTS

The authors would like to thank Dr. Ignaz Eisele (EMFT Fraunhofer Institute, Munich, Germany) for developing prototypes and custom structures, Dr. Karl-Heinz Hoffmann (Bavarian Academy of Science, Germany), Dr. Shiban Koul (IIT-Delhi, India), Dr. Tatsuo Itoh (UCLA, USA), Dr. Matthias Rudolph (BTU Cottbus, Germany), Dr. Afshin Daryoush (Drexel University, Philadelphia, USA) and Dr. Arye Rosen (Rowan University, NJ, USA) for their valuable inputs, technical discussions and developing prototype for the theoretical proof and experimental validation. The authors would also like to thank the Indian Government in 1990s for supporting the negative index Möbius strips based RF&MW components for space applications. A special heartfelt thank you goes to our close friend Prof. D. Sundararajan who passed away on 22nd September 2014. Prof. Sundararajan and Dr. Poddar had been working on this mysterious Metamaterial Mobius strips since 1990 and were the first ones to demonstrate Möbius strips sensors for the applications in underground mine detections, memory devices, RFID for the detection of chemical explosives and weapons made of plastics, and composite materials which were often missed and undetected by RADAR.

References

1. D. R. Smith, S. Schultz, P. Markoš and C. M. Soukoulis, “Determination of Effective Permittivity and Permeability of Metamaterials from Reflection and Transmission Coefficients,” *Physical Review B*, Vol. 65, No. 19, April 2002, pp. 195104-1-5.
2. D. R. Smith, D. C. Vier, Th. Koschny and C. M. Soukoulis, “Electromagnetic Parameter Retrieval from Inhomogeneous Metamaterials,” *Physical Review E*, Vol. 71, No. 3, March 2005, pp. 36617-1-11.
3. J. B. Pendry, A. J. Holden, D. J. Robbins and W. J. Stewart, “Low Frequency Plasmons in Thin.-Wire Structures,” *Journal of Physics: Condensed Matter*, Vol. 10, No. 22, June 1998, pp. 4785-4809.

Ulrich L. Rohde, Federal Armed Forces University, Munich, Germany ; Ajay K. Poddar, Synergy Microwave, NJ

4. J. B. Pendry, A. J. Holden, W. J. Stewart and I. Youngs, "Extremely Low Frequency Plasmons in Metallic Mesostructures," *Physical Review Letters*, Vol. 76, No. 25, June 1996, pp. 4773–4776.
5. J. B. Pendry, A. J. Holden, D. J. Robbins and W. J. Stewart, "Magnetism From Conductors and Enhanced Nonlinear Phenomena," *IEEE Transactions on Microwave Theory and Techniques*, Vol. 47, No. 11, November 1999, pp. 2075–2084.
6. J. D. Jackson, "Classical Electromagnetics," John Wiley & Sons, 3rd Edition, New York, 1999.
7. V. G. Veselago, "Electrodynamics of Substances with Simultaneously Negative Values of Sigma and Mu," *Soviet Physics Uspekhi*, Vol. 10, 1968, pp. 509–514.
8. Y. Liu and X. Zhang, "Metamaterials: A New Frontier of Science and Technology," *Chemical Society Reviews*, Vol. 40, January 2011, pp. 2494–2507.
9. D. R. Smith, S. Schultz, P. Markoš and C. M. Soukoulis, "Determination of Effective Permittivity and Permeability of Metamaterials from Reflection and Transmission Coefficients," *Physical Review B: Condensed Matter*, April 2002, Vol. 65, April 2002, pp. 195104-1-5.
10. X. Chen, B. I. Wu, J. A. Kong and T. M. Grzegorzczak, "Retrieval of the Effective Constitutive Parameters of Bianisotropic Metamaterials," *Physical Review E, Statistical Physics, Plasmas, Fluids, and Related Interdisciplinary Topics*, Vol. 71, No. 4, April 2005, pp. 046610.
11. D. R. Smith, D. C. Vier, Th. Koschny and C. M. Soukoulis, "Electromagnetic Parameter Retrieval from Inhomogeneous Metamaterials," *Physical Review E: Statistical, Nonlinear, Biological, and Soft Matter Physics*, Vol. 71, March 2005, pp. 036617-1-11.
12. C. Menzel, T. Paul, C. Rockstuhl, T. Pertsch, S. Tretyakov and F. Lederer, "Validity of Effective Material Parameters for Optical Fishnet Material," *Physical Review B: Condensed Matter*, Vol. 81, No. 3, January 2010, pp. 035320/1-5.
13. R. A. Shelby, D. R. Smith and S. Schultz, "Experimental Verification of a Negative Index of Refraction," *Science*, Vol. 292, No. 5514, April 2001, 292, pp. 77–79.
14. S. Xiao, U. K. Chettiar, A. V. Kildishev, V. P. Drachev and V. M. Shalaev, "Yellow-Light Negative-Index Metamaterials," *Optics Letters*, Vol. 34, No. 22, 2009, pp. 3478–3480.
15. S. Zhang, W. Fan, N. C. Panoiu, K. J. Malloy, R. M. Osgood and S. R. J. Brueck, "Experimental Demonstration of Near-Infrared Negative-Index Metamaterials," *Physical Review Letters*, Vol. 95, September 2005, pp. 137404.
16. G. Dolling, C. Enkrich, M. Wegener, C. M. Soukoulis and S. Linden, "Simultaneous Negative Phase and Group Velocity of Light in a Metamaterial," *Science*, 2006, Vol. 312, No. 5775, May 2006, pp. 892–894.
17. M. C. K. Wiltshire¹, J. B. Pendry, I. R. Young, D. J. Larkman, D. J. Gilderdale and J. V. Hajnal, "Microstructured Magnetic Materials for RF Flux Guides in Magnetic Resonance Imaging," *Science*, Vol. 291, No. 5505, February 2001, pp. 849–851.
18. C. Caloz, A. Sanada, and T. Itoh, "A Novel Composite Right/Left-Handed Coupled-Line Directional Coupler with Arbitrary Coupling Level and Broad Bandwidth," *IEEE Transactions on Microwave Theory and Techniques*, Vol. 52, No. 3, March 2004, pp. 980–992.
19. A. Kurs, A. Karalis, R. Moffatt, J. D. Joannopoulos, P. Fisher and M. Soljacic, *Science*, Vol. 317, No. 5834, July 2007, pp. 83–86.
20. J. B. Pendry, "Negative Refraction Makes a Perfect Lens," *Physical Review Letters*, Vol. 85, October 2000, pp. 3966–3969.
21. X. Zhang and Z. W. Liu, "Superlenses to Overcome the Diffraction Limit," *Nature Materials*, Vol. 7, June 2008, pp. 435–441.

Ulrich L. Rohde, Federal Armed Forces University, Munich, Germany ; Ajay K. Poddar, Synergy Microwave, NJ

22. N. Fang, H. Lee, C. Sun and X. Zhang, "Sub-Diffraction-Limited Optical Imaging with a Silver Superlens," *Science*, Vol. 308, No. 5721, April 2005, pp. 534–537.
23. A. A. Zharov, I. V. Shadrivov and Yu. S. Kivshar, "Nonlinear Properties of Left-Handed Metamaterials," *Physical Review Letters*, Vol. 91, No. 3, July 2003, pp. 037401-1-4.
24. V. M. Agranovich, Y. R. Shen, R. H. Baughman and A. A. Zakhidov, "Linear and Nonlinear Wave Propagation in Negative Refraction Metamaterials," *Physical Review B: Condensed Matter*, Vol. 69, No. 16, April 2004, pp. 165112.
25. N. Lazarides, M. Eleftheriou and G. P. Tsironis, "Discrete Breathers in Nonlinear Magnetic Metamaterials," *Physical Review Letters*, Vol. 97, October 2006, pp. 157406.
26. Y. Liu, G. Bartal, D. A. Genov and X. Zhang, "Subwavelength Discrete Solutions in Nonlinear Metamaterials," *Physical Review Letters*, Vol. 99, October 2007, pp. 153901.
27. N.M. Litchinitser and V.M. Shalaev, "Photonic Metamaterials," *Laser Physics Letters*, Vol. 5, 2008, pp. 411–420.
28. M. W. Klein, C. Enkrich, M. Wegener and S. Linden, "Second-Harmonic Generation from Magnetic Metamaterials," *Science*, Vol. 313, No. 5786, July 2006, pp.
29. I. V. Shadrivov, S. K. Morrison and Y. S. Kivshar, "Tunable Split-Ring Resonators for Nonlinear Negative-Index Metamaterials," *Optics Express*, Vol. 14, No. 20, October 2006, pp. 9344–9349.
30. B. N. Wang, J. F. Zhou, T. Koschny and C. M. Soukoulis, "Nonlinear Properties of Split-Ring Resonators," *Optics Express*, Vol. 16, No. 20, 2008, pp. 16058–16063.
31. T. Driscoll, H. T. Kim, B. G. Chae, B. J. Kim, Y. W. Lee, N. M. Jokerst, S. Palit, D. R. Smith, M. Di Ventra and D. N. Basov, "Memory Metamaterials," *Science*, Vol. 325, No. 5947, September 2009, pp. 1518–1521.
32. V. V. Cheianov, V. Fal'ko and B. L. Altshuler, "The Focusing of Electron Flow and a Veselago Lens in Graphene P-N Junctions," *Science*, Vol. 315, No. 5816, March 2007, pp. 1252–1255.
33. S. Zhang, D. A. Genov, C. Sun and X. Zhang, "Cloaking of Matter Waves," *Physical Review Letters*, Vol. 100, No. 12, March 2008, pp. 123002-1-4.
34. Z. Jacob, J. Y. Kim, G. V. Naik, A. Boltasseva, E. E. Narimanov and V. M. Shalaev, "Engineering Photonic Density of States Using Metamaterials," *Applied Physics B: Lasers and Optics*, Vol. 100, No. 1, July 2010, pp. 215–218.
35. M. A. Noginov, H. Li, Y. A. Barnakov, D. Dryden, G. Nataraj, G. Zhu, C. E. Bonner, M. Mayy, Z. Jacob and E. E. Narimanov, "Controlling Spontaneous Emission with Metamaterials," *Optics Letters*, Vol. 35, No. 11, 2010, pp. 1863–1865.
36. C. Henkel and K. Joulain, "Casimir Force Between Designed Materials: What is Possible and What Not," *Europhysics Letters*, Vol. 72, No. 6, December 2005, pp. 929–935.
37. U. Leonhardt and T. G. Philbin, "Quantum Levitation by Left-Handed Metamaterials," *New Journal of Physics*, Vol. 9, August 2007, pp. 010254-1-11.
38. F.S.S. Rosa, D.A.R. Dalvit and P.W. Milonni, "Casimir-Lifshitz Theory and Metamaterials," *Physical Review Letters*, Vol. 100, No. 18, May 2008, pp. 183602.
39. R. Zhao, J. Zhou, T. Koschny, E. N. Economou and C. M. Soukoulis, "Repulsive Casimir Force in Chiral Metamaterials," *Physical Review Letters*, Vol. 103, No. 10, September 2009, pp. 103602.
40. V. Yannopapas and N. V. Vitanov, "First-Principles Study of Casimir Repulsion in Metamaterials," *Physical Review Letters*, Vol. 103, No. 12, September 2009, pp. 120401.
41. S. I. Maslovski and M. G. Silveirinha, "Ultralong-range Casimir-Lifshitz Forces Mediated by Nanowire Materials," *Physical Review A*, No. 82, No. 2, August 2010, pp. 022511.

Ulrich L. Rohde, Federal Armed Forces University, Munich, Germany ; Ajay K. Poddar, Synergy Microwave, NJ

42. Y. Yang, H. Zhang, J. Zhu, G. Wang, T. -R. Tzeng, X. Xuan, K. Huang and P. Wang, "Distinguishing the Viability of a Single Yeast Cell with an Ultra-Sensitive Radio Frequency Sensor," *Lab Chip*, Vol. 10, January 2010, pp. 553–555.
43. Y. Cui and P. Wang, "The Design and Operation of Ultra-Sensitive and Tunable Radio-Frequency Interferometers," *IEEE Transactions on Microwave Theory and Techniques*, Vol. 62, No. 12, December 2014, pp. 3172–3182.
44. G. P. Agrawal, *Fiber-Optic Communication Systems*, 3rd ed., Wiley, 2010.
45. A. H. Gnauck, R. W. Tkach, A. R. Chraplyvy and T. Li, "High-Capacity Optical Transmission Systems," *Journal of Lightwave Technology*, Vol. 26, No. 9, May 2008, pp. 1032-1045.
46. R. J. Essiambre and R. W. Tkach, "Capacity Trends and Limits of Optical Communication Networks," *Proceedings of the IEEE*, Vol. 100, No. 5, May 2012, pp. 1035–1055.
47. A. H. Gnauck, P. J. Winzer, S. Chandrasekhar, X. Liu, B. Zhu and D. W. Peckham, "Spectrally Efficient Long-Haul WDM Transmission Using 224-Gb/s Polarization-Multiplexed 16-QAM," *Journal of Lightwave Technology*, Vol. 29, No. 4, February 2011, pp. 373–377.
48. D. J. Richardson, J. M. Fini and L. E. Nelson, "Space-Division Multiplexing in Optical Fibres," *Nature Photonics*, Vol. 7, No. 5, April 2013, pp. 354–362.
49. B. Zhu, J. M. Fini, M. F. Yan, X. Liu, S. Chandrasekhar, T. F. Taunay, M. Fishteyn, E. Monberg and F. V. Dimarcello, "High-Capacity Space-Division-Multiplexed DWDM Transmissions Using Multi Core Fiber," *Journal of Lightwave Technology*, Vol. 30, No. 4, February 2012, pp. 486–492.
50. X. Liu, S. Chandrasekhar, X. Chen, P. J. Winzer, Y. Pan, T. Taunay, B. Zhu, M. Fishteyn, M. F. Yan, J. Fini, E. M. Monberg and F. V. Dimarcello, "1.12-Tb/s 32-QAM-OFDM Superchannel with 8.6-b/s/Hz Intrachannel Spectral Efficiency and Space-Division Multiplexing with 60-b/s/Hz Aggregate Spectral Efficiency," *Optical Express*, Vol. 19, No. 26, December 2011, pp. B958–B964.
51. R. Ryf, S. Randel, A. H. Gnauck, C. Bolle, A. Sierra, S. Mumtaz, M. Esmaeelpour, E. C. Burrows, R. J. Essiambre, P. J. Winzer, D. W. Peckham, A. H. McCurdy and R. Lingle, "Mode-Division Multiplexing Over 96 km of Few-Mode Fiber Using Coherent 6 × 6 MIMO Processing," *Journal of Lightwave Technology*, Vol. 30, No. 4, February 2012, pp. 521–531.
52. N. Bozinovic, Y. Yue, Y. Ren, M. Tur, P. Kristensen, H. Huang, A. E. Willner and S. Ramachandran, "Terabit-Scale Orbital Angular Momentum Mode Division Multiplexing in Fibers," *Science*, Vol. 340, No. 6140, June 2013, pp. 1545–1548.
53. N. Bozinovic, S. Golowich, P. Kristensen and S. Ramachandran, "Control of Orbital Angular Momentum of Light, with Optical Fibers," *Optics Letters*, Vol. 37, No. 13, 2012, pp. 2451–2453.
54. P. Gregg, P. Kristensen, S. Golowich, J. Olsen, P. Steinvurzel and S. Ramachandran, "Stable Transmission of 12 OAM States in Air-Core Fiber," *Optical Society of America CLEO 2013 Technical Digest*, June 2013, pp. 1–2.
55. J. Zeng, X. Wang, J. Sun, A. Pandey, A. N. Cartwright and N. M. Litchinitser, "Manipulating Complex Light with Metamaterial," *Scientific Reports*, Vol. 3, No. 2826, October 2013.
56. F. Intravaia and C. Henkel, "Can Surface Plasmons Tune the Casimir Forces Between Metamaterials?" *Institut fuer Physik und Astronomie*, Poster, <http://cnls.lanl.gov/casimir/PostersSF/Intravaia-SantaFe-poster.pdf>.
57. S. Minter, K. Wegter-McNelly and R. Chiao, "Do Mirrors for Gravitational Wave Exist?" *Physica E: Low-dimensional Systems and Nanostructures*, Vol. 42, No. 3, January 2010, pp. 234-255.

Ulrich L. Rohde, Federal Armed Forces University, Munich, Germany ; Ajay K. Poddar, Synergy Microwave, NJ

58. R.E. Glover and M. Tinkham, "Transmission of Superconducting Films at Millimeter-Microwave and Far Infrared Frequencies," *Physical Review*, Vol. 104, No. 3, November 1956, pp. 844.
59. M. Tinkham, "Introduction to Superconductivity," 2nd ed., Dover, New York, 2004.
60. R. M. Wald, "General Relativity," University of Chicago Press, Chicago, 1984.
61. W.H. Zurek, "Decoherence, Einselection, and the Quantum Origins of the Classical," *Reviews of Modern Physics*, Vol. 75, No. 3, September 2003, pp. 715.
62. B.S. DeWitt, "Superconductors and Gravitational Drag," *Physical Review Letters*, Vol. 16, No. 24, June 1966, pp. 1092.
63. R. Y. Chiao, "Science and Ultimate Reality," J. D. Barrow, P. C. W. Davies, and C. L. Harper (eds.) Jr. (Cambridge University Press, Cambridge, 2004), p. 254.
64. C. Kiefer and C. Weber, "On the Interaction of Mesoscopic Quantum Systems with Gravity," *Annalen der Physik*, Vol. 14, No. 4, April 2005, pp. 253–278.
65. R.Y. Chiao and W. J. Fitelson, "Time and Matter in the Interaction Between Gravity and Quantum Fluids: Are there Macroscopic Quantum Transducers Between Gravitational and Electromagnetic Waves?" arXiv:gr-qc/0303089, March 2003.
66. S. Weinberg, "Gravitation and Cosmology," Wiley, New York, 1972.
67. A. Lambrecht, "The Casimir Effect: a Force From Nothing," *Physics World*, September 2002.
68. J. Q. Quach, "Gravitational Casimir Effect," *Physical Review Letters*, Vol. 114, No. 8, February 2015, pp. 081104-1-5.
69. U. L. Rohde and A. K. Poddar, "Möbius Metamaterial Inspired Next Generation Circuits and Systems," *Microwave Journal*, Vol. 59, No. 5, May 2016, pp. 62–88.
70. U. L. Rohde and A. K. Poddar, "Möbius Metamaterial Inspired: Signal Sources and Sensors," *Microwave Journal*, Vol. 59, No. 6, June 2016.
71. U. L. Rohde and A. K. Poddar, "Ka-Band Metamaterial Möbius Oscillator (MMO) Circuit," *IEEE International Microwave Symposium Digest*, May 2016, pp. 1–4.
72. U. L. Rohde and A. K. Poddar, "Möbius Metamaterial Strips Resonator: Tunable Oscillators for Modern Communication Systems," *Microwave Journal*, Vol. 58, No. 1, January 2015.
73. U. L. Rohde and A. K. Poddar, "Metamaterial Resonators: Theory and Applications," *Microwave Journal*, Vol. 57, No. 12, December 2014, pp. 74–86.
74. U. L. Rohde and A. K. Poddar, "Möbius Strips and Metamaterial Symmetry: Theory and Applications," *Microwave Journal*, Vol. 57, No. 11, November 2014, pp. 76–88.
75. U. L. Rohde, A. K. Poddar and D. Sundararjan, "Printed Resonators: Möbius Strips Theory and Applications," *Microwave Journal*, Vol. 56, No. 11, November 2013, pp. 24–54.
76. C. P. Scarborough, Z. H. Jiang, D. H. Werner, C. Rivero-Baleine and C. Drake, "Experimental Demonstration of an Isotropic Metamaterial Super Lens with Negative Unity Permeability at 8.5 MHz," *Applied Physics Letters*, Vol. 101, No. 1, July 2012, pp. 014101-1-3.
77. Z. H. Jiang, M. D. Gregory and D. H. Werner, "A Broadband Monopole Antenna Enabled by an Ultrathin Anisotropic Metamaterial Coating," *IEEE Antennas and Wireless Propagation Letters*, Vol. 10, 2011, pp. 1543-1546.
78. P. C. Peters, "Index of Refraction for Scalar, Electromagnetic, and Gravitational Waves in Weak Gravitational Fields," *Physical Review D*, Vol. 9, April 1974, pp. 2207–2218.
79. S. J. Minter, K. Wegter-McNelly and R. Y. Chiao, "Do Mirrors for Gravitational Waves Exist?" *Physica E* 42, 2010.

Ulrich L. Rohde, Federal Armed Forces University,
Munich, Germany ; Ajay K. Poddar, Synergy
Microwave, NJ